DETERMINATION OF THE RADIATIVE DECAY WIDTH

OF THE $K^{*+}(890)$ MESON

by

Clark David Chandlee

Submitted in Partial Fulfillment

of the

Requirements for the Degree

DOCTOR OF PHILOSOPHY

University of Rochester

Rochester, New York

1982

CURRICULUM VITAE

The author was born on October 23, 1954 in Frederick, Maryland. He attended public school in East Brunswick, New Jersey, graduating from East Brunswick High School in June of 1972. The following September he began his undergraduate studies at Rutgers College of Rutgers University, The State University of New Jersey, with a major in physics. He graduated with honors and high distinction in physics with an AB degree in May of 1976.

The author entered the Graduate School of the University of Rochester the following September to pursue a higher education in physics. Upon entering the Graduate School, the author was granted a Rush Rhees Fellowship. He received further support as a research assistant for five years and as a teaching assistant for one year.

Pursuant to the Ph.D. degree, the author received a Master of Arts degree in physics in May of 1978.

Professor Paul F. Slattery acted as the author's graduate adviser and later directed the course of his thesis work.

ACKNOWLEDGMENTS

The author would like to take this opportunity to express his gratitude to all who have helped to bring this endeavor to its fruition. Such a pursuit depends heavily on the hard work of many people and acknowledgment of such is duly warranted in light of these many contributions.

On this experiment, the principal collaborators, including physicists, professors, and students from Fermi National Accelerator Laboratory, the University of Minnesota, and the University of Rochester were David Berg, Joseph Biel, Selcuk Cihangir, Bruce Collick, Thomas Ferbel, Stephen Heppelmann, Joey Huston, Terrence Jensen, Alan Jonckheere, Terrence Joyce, Peter Koehler, Frederick Lobkowicz, Yousef Makdisi, Marvin Marshak, Michael McLaughlin, Charles Nelson, Takayoshi Ohshima, Earl Peterson, Keith Ruddick, Michael Shupe, Paul Slattery, Patrick Thompson, John Whittaker, and Marek Zielinski.

The author would like to express his appreciation to his adviser, Professor Paul F. Slattery, for his guidance and concern during the extent of this thesis work.

He would also like to thank Professors M. Marshak, E. Peterson, and K. Ruddick of the University of Minnesota, Professors T. Ferbel, and F. Lobkowicz of the University of Rochester, and Fermi National Accelerator Laboratory staff physicists J. Biel, A. Jonchkeere, C. Nelson, and P. Koehler for their efforts leading to the successful completion of this experiment. Professor Ferbel is also thanked for many helpful discussions and for his criticism of this manuscript.

Special thanks is also extended to research associates T. Jensen, T. Ohshima, M. Shupe, and P. Thompson for their day-to-day leadership and control of the running and analysis of the experiment. The assistance of M. Zielinski in fitting some of the data is also gratefully acknowledged.

The author would also like to recognize with appreciation the assistance and numerous contributions of his fellow graduate students D. Berg, S. Cihangir, B. Collick, S. Heppelmann, J. Huston, and M. McLaughlin. The help of Bruce Kearns during the early prepatory stages of this experiment and that of students John Bartelt and Scott Sherman during certain phases of the running period is also acknowledged with gratitude.

Thanks also goes out to T. Haelen and the staff of the Cyclotron Lab at the University of Rochester for their fine design and assembly of various elements of the experimental apparatus.

Edna Hughes is thanked for her fine efforts in typing this thesis as is John Sheedy for the inking of the figures.

The author would also like to express his thanks and appreciation to Mrs. Betty Cook for her help in various university matters and for making his stay in Rochester a little less complicated.

Finally, the author is indebted to his parents, George and Gladys, his grandmother, Anna Smith, and his brothers and sisters, George, Joel, Kim, and Tammy for their encouragement during the years of his graduate career. This thesis is specifically dedicated to his sister Tammy.

This research was supported in part by the U.S. Department of Energy and the National Science Foundation.

ABSTRACT

A systematic study of the coherent excitation of high energy pions and kaons by nuclear targets has been completed at Fermilab (Experiment 272) with the intent of extracting the radiative decay widths of the various vector and tensor mesons. This work was initiated to furnish experimental results for comparison with theoretical predictions based on unitary symmetry schemes, quark models, and vector dominance models with the hope of shedding light on the structure of the quark-antiquark system.

The work presented here deals with data collected during the second running period of E272 on the excitation of incident 200 GeV/c K^+ by copper and lead targets for the purpose of precisely determining the radiative width for the transition $K^{*+}(890) \rightarrow K^+\gamma$.

The experiment was performed in the M1E secondary beam line of the Meson Lab utilizing an enhanced, Cherenkov tagged, positive kaon beam, a forward charged particle spectrometer consisting of drift and proportional wire chambers, and a liquid argon calorimeter for photon detection.

A Primakoff type analysis of excitation in the nuclear Coulomb field including a strong contribution to the coherent production process from isoscalar exchange was applied to data for both the $K^+\pi^0$ and $K^0_S\pi^+$ decay modes of the $K^{*+}(890)$. The production differential cross section can be written as $d\sigma/dt' = |A_c + e^{i\theta}A_s|^2$, where A_c, the Coulombic amplitude, and A_s, the strong amplitude, are proportional to the square roots of Γ, the radiative partial width, and C_s, the elementary strength of the ω exchange process on nucleons, respectively. The angle θ measures the relative phase between the two coherent amplitudes.

This three-parameter fit to the data gave very consistent results over the range of targets and final states previously mentioned and yielded weighted averages of:

$$\Gamma(K^{*+}(890) \rightarrow K^+\gamma) = 51 \pm 3 \pm 4 \quad \text{kev}$$
$$C_s = 3.2 \pm 0.7 \quad \text{mb/GeV}^4$$
$$\theta = 84 \pm 14 \quad \text{degrees}$$

where the errors on Γ are statistical and systematic, respectively.

The result for $\Gamma(K^{*+}(890) \rightarrow K^+\gamma)$ is in reasonable agreement with theoretical predictions, but the value for C_s does not agree with extrapolation from lower energy data.

TABLE OF CONTENTS

	Page
CURRICULUM VITAE	ii
ACKNOWLEDGMENTS	iii
ABSTRACT	v
TABLE OF CONTENTS	vii
LIST OF TABLES	ix
LIST OF FIGURES	x
CHAPTER	
I. INTRODUCTION	1
A. Introduction to Quantum Chromo-Dynamics	1
B. Theoretical Models of Vector Meson Radiative Decays	3
C. Theoretical Predictions for Radiative Decay Rates	11
D. Outline of Thesis	14
II. COHERENT NUCLEAR PRODUCTION	17
A. Introduction	17
B. Primakoff Production	25
C. Coherent Strong Excitation	28
D. Theoretical Coherent Production Cross Sections	30
III. EXPERIMENTAL SET-UP	32
A. The Beam Line	32
B. Beam Spectrometer and Targets	38
C. Charged Particle Spectrometer	42
D. Liquid Argon Calorimeter	54
E. Experimental Triggers and Data Acquisition	58

	Page
IV. CALIBRATION OF SPECTROMETER	72
A. Alignment and Calibration of the Wire Chambers	72
B. Calibration of the Momentum Analyzing Magnet	87
C. Calibration of the Liquid Argon Calorimeter	90
V. ANALYSIS OF EXPERIMENTAL DATA	102
A. Monte Carlo Model of Experiment	102
B. Normalization	122
C. Determination of Absolute Cross Sections	137
VI. FITTING OF $K^{*+}(890)$ DATA	160
A. Introduction	160
B. Check on Decay Angular Distributions	160
C. Check on K_s^o Life-time	163
D. Fitting Formalism for the Differential Cross Section	165
E. Fits to $d\sigma/dm$	167
F. Fits to $d\sigma/dt'$	174
VII. CONCLUSIONS	184
A. Introduction	184
B. Final Results	185
C. Discussion of Results	186
REFERENCES	189

LIST OF TABLES

		Page
I.	Quark Wavefunctions of Pertinent Vector and Pseudoscalar Mesons	7
II.	Reduced $V \to P\gamma$ Transition Rates	8
III.	Quark Model Predictions for Widths of Pertinent Radiative Decays	13
IV.	Extrapolated Predictions for $V \to P\gamma$ Partial Widths Using Experimental Input	15
V.	Parameters of the Experimental Targets	41
VI.A	Beam Flux, Target Related, and Spectrometer Related Corrections for the Decay $K^+ \to \pi^+\gamma\gamma$	129
VI.B	Beam Flux, Target Related, and Spectrometer Related Corrections for the Decay $K^+ \to \pi^+\pi^+\pi^-$	130
VI.C	Beam Flux, Target Related, and Spectrometer Related Corrections for the $K^{*+} \to K^+\gamma\gamma$ Data	131
VI.D	Beam Flux, Target Related, and Spectrometer Related Corrections for the $K^{*+} \to \pi^+\pi^+\pi^-$ Data	132
VII.A	Totals of Corrections Applied to the K^{*+} ($\to K^+\gamma\gamma$) t' Distribution	151
VII.B	Totals of Corrections Applied to the K^{*+} ($\to \pi^+\pi^+\pi^-$) t' Distribution	152
VIII.	Results of Fits to the $K^{*+}(890)$ Mass Differential Cross Sections	175
IX.	Results of Fits to the $K^{*+}(890)$ -t' Differential Cross Sections	182

LIST OF FIGURES

Figure			Page
1.	(a)	Kinematic variables associated with the coherent reaction $a + A \to a^* + A$	20
	(b)	Diagram for Primakoff production	
2.	(a)	Diagram for $K^{*+}(890)$ Primakoff production on the nuclear target A in the rest frame of the $K^{*+}(890)$ (Gottfried-Jackson reference frame)	23
	(b)	Definition of the Gottfried-Jackson reference frame	
	(c)	Definition of the helicity reference frame	
3.		Schematic diagram of the M1 beam line elements. The elements B are bending dipole magnets and Q are focusing quadrapole magnets. K1, 2, 3 are beam species tagging Cherenkov counters. The half width of the beam envelope transported by the nominally tuned elements is shown at the top.	33
4.		Tagging efficiency times beam species fraction for the Cherenkov counter K1 as a function of helium pressure. The requirements of 2-fold and 3-fold coincidences are explained in the text. K1 represents the Cherenkov signal while B is a beam particle signal.	36
5.		Schematic diagram of the positions of the scintillator counters used in the experiment. The inset details the counter arrangement in and around the target box.	37
6.		Plan view of the E272 experimental set-up.	39
7.		Diagram of the charged veto logic common to all electronic logic triggers set to detect K*'s.	44
8.		Schematic diagram of the MWPC read-out and electronics debugging system.	47
9.		Wire geometry of one drift cell of the (a) upstream (DI,II) and (b) downstream (DIII,DIV) DWC's. Efficiency curves for chambers of each cell type obtained with a β^- source are also shown.	50
10.		Schematic diagram of the DWC read-out and drift time digitizer calibration scheme.	53
11.		Exploded view of two layers (one x, one y) of the LAC detailing its construction.	55

Figure		Page
12.	Analog electronics used to determine LAC calorimetric signals for use in the trigger logic.	59
13.	Track counter logic diagram for the ρ and V triggers.	63
14.	Diagram illustrating formation of the LAC logic signal for use in the ρ trigger.	66
15.	Total elements of logic for the ρ, V, random beam, first beam and calibration triggers. Also shown in the dotted box are the elements of the ρ and V pre-triggers.	70
16.	Illustration of the flow of data through the on-line data acquisition system.	71
17.	Plot of drift time in DWC versus distance charged particle passed from sense wire for typical (a) upstream and (b) downstream chambers. Also shown are the results of a fit described in the text. These plots were obtained with straight through beam events.	75
18.	Beam related effects on the drift time-position relation of the DWC's. Shown are the effects in two chambers in DI ((a) DIX1, (b) DIX2).	77
19.	Drift time-position relation for DWC's obtained using charged particles scattered out of the beam region. Fitting for the drift velocity and the variables t_o and θ is described in the text. These plots represent a sum over all events and over all (a) upstream and (b) downstream planes for each event.	82
20.	Histograms of deviations of measured position from expected position of charged particle in (a) upstream and (b) downstream DWC's. The errors associated with the extrapolation to the expected position have not been removed.	83
21.	Deviation of measured position from expected position of the charged particle as a function of position within a drift cell for (a) upstream and (b) downstream chambers.	84
22.	Plots of (a) upstream and (b) downstream DWC resolutions as a function of position within a drift cell.	86

Figure		Page
23.	(a) $\pi^+\pi^-$ mass spectrum derived from $K^{*+}(890)\to K^o_S\pi^+ \to\pi^+\pi^-\pi^+$ events with results of a fit to a Gaussian line shape after final calibration of the BM109 magnet. (b) Histogram of γγ masses derived from $K^+\to\pi^+\pi^o\to\pi^+\gamma\gamma$ events after final calibration of the LAC. Superimposed is the Monte Carlo expectation normalized to the number of real data events in the range $0.110\ \text{GeV} \le m_{\gamma\gamma} < 0.160\ \text{GeV}$.	89
24.	(a) Plot of energy deposited in LAC by positrons from $K^+ \to e^+\pi^o\nu$ decays versus momentum of the same measured by the charged particle spectrometer. (b) Deviation of energy deposited in LAC by these same positrons from the momentum measured by the charged particle spectrometer.	97
25.	Energy resolution of LAC obtained from $K^+ \to e^+\pi^o\nu$ decays.	99
26.	Position resolution of (a) positrons and (b) hadrons in the LAC obtained from K^+ decays. The uncertainty in position includes the error in the extrapolation of the charged particle trajectory from the DWC system to the LAC.	100
27.	Reconstructed beam (a) $K^+ \to \pi^+\pi^o$ and (b) $K^+ \to \pi^+\pi^+\pi^-$ decay z-vertex distributions from data with the lead target in place. The smooth curves are Monte Carlo predictions normalized to the number of real data events between the arrows. Cuts on the data are explained in the text.	111
28.	Reconstructed total energy for the (a) 2π and (b) 3π decays of beam kaons. Superimposed is the Monte Carlo expectation normalized to the number of real data events between the arrows. Cuts on the data are explained in the text.	113
29.	(a) Histogram of the energy asymmetry of photons from π^o decay resulting from $K^+ \to \pi^+\pi^o$ beam decays. (b) Histogram of cosθ of the π^+ resulting from $K^+ \to \pi^+\pi^o$ decays in the helicity frame. The events in both of these histograms have been isolated with cuts on the data explained in the text. The smooth curves represent Monte Carlo predictions normalized to the total number of events in each histogram.	114

Figure		Page
30.	Reconstructed K^+ masses for the (a) 2π and (b) 3π decay modes. Superimposed are the Monte Carlo predictions normalized to the data between the arrows.	116
31.	Comparison of t distributions for real data to that generated by the Monte Carlo for $K^+ \to \pi^+\pi^0$ and $K^+ \to \pi^+\pi^+\pi^-$ decays with the (a) empty, (b) copper, and (c) lead targets in place. Cuts on the data are explained in the text. The Monte Carlo predictions (smooth curves) are normalized to the total number of real data events with $t < 0.001$ GeV^2.	118
32.	Plots of P_t resolution extracted from $K^+ \to \pi^+\pi^0$ data on each of the targets as a function of decay vertex for both (a) real data and (b) Monte Carlo data. Cuts imposed on the data are explained in the text. The dotted lines represent fits explained in the text.	120
33.	S-counter pulse height distributions for well defined beam particles (random beam trigger) and for clean $K^+ \to \pi^+\pi^+\pi^-$ decays (V-triggers) isolated with cuts explained in the text. The V-trigger data has been normalized to the random beam trigger data between the arrows. The shaded region indicates the loss of events in the V-trigger mode resulting from discrimination of the S-counter signal.	126
34.	Plots of the (a) uncorrected $K^+ \to \pi^+\pi^0$ decay rate and that (b) corrected as explained in the text as a function of run number.	134
35.	Plots of K^+ decay normalization correction factors as explained in the text as a function of decay vertex for (a) $K^+ \to \pi^+\pi^0$ and (b) $K^+ \to \pi^+\pi^+\pi^-$ decays. The dotted lines represent fits to the data explained in the text.	136
36.	Interaction z-vertex distributions for coherently excited $K^{*+}(890)$'s summed over copper and lead targets with an empty target subtraction detected in the (a) $K^+\gamma\gamma$ and (b) $\pi^+\pi^+\pi^-$ final states. Superimposed are the Monte Carlo expectations normalized to the data between the arrows.	141

Figure		Page
37.	Reconstructed total energy distributions for coherently produced $K^{*+}(890)$'s summed over copper and lead targets with an empty target subtraction detected in the (a) $K^+\gamma\gamma$ and (b) $\pi^+\pi^+\pi^-$ final states. The smooth curves represent the Monte Carlo predictions normalized to the number of real data events between the arrows.	143
38.	Distributions of (a) $\gamma\gamma$ masses and (b) $\pi^+\pi^-$ masses found in the final states $K^+\gamma\gamma$ and $\pi^+\pi^+\pi^-$, respectively, resulting from the decay of coherently produced $K^{*+}(890)$ events, summed over copper and lead target data with an empty target subtraction. Superimposed are the Monte Carlo predictions normalized to the data between the arrows.	144
39.	(a) Histogram of energy asymmetry of photons from π^0 decay isolated in the $K^+\gamma\gamma$ final state of coherently produced $K^{*+}(890)$'s. (b) Reconstructed decay z-vertex distribution for neutral "V" particles found in the $\pi^+\pi^+\pi^-$ final state of decay of coherently excited $K^{*+}(890)$'s. Both of these histograms contain data obtained on copper and lead targets with an empty target subtraction and the smooth curves represent the Monte Carlo predictions normalized to the data between the arrows.	146
40.	Distributions of $\cos\theta$ in the Gottfried-Jackson frame for the K^+ and π^+ found in the decay of coherently produced $K^{*+}(890)$'s to (a) $K^+\pi^0$ and (b) $K^0_s\pi^+$, respectively. Each histogram contains data obtained from both copper and lead targets after a target empty subtraction. The smooth curves are the Monte Carlo predictions for the decays of coherently excited $K^{*+}(890)$'s normalized to the total number of events in each histogram.	147
41.	Mass distributions for the $K^+\pi^0$ and $K^0_s\pi^+$ final states resulting from the decay of coherently excited incident K^+'s on the copper target, (a) and (b) respectively, and on the lead target, (c) and (d), respectively, after an empty target subtraction. The arrows indicate the mass cuts applied to the data to isolate the $K^{*+}(890)$ resonance.	154
42.	Histograms of the -t' distributions for the $K^+\pi^0$ and $K^0_s\pi^+$ final states resulting from the decay of coherently produced $K^{*+}(890)$'s on the copper target, (a) and (b), respectively, and on the lead target, (c) and (d), respectively, after an empty target subtraction. These data represent the raw input for an extraction of the partial width for the decay $K^{*+}(890) \to K^+\gamma$.	156-157

Figure		Page
43.	Acceptance corrected distributions for $\cos\theta$ in the Gottfried-Jackson frame for the K^+ and π^+ found in the decay of coherently produced $K^{*+}(890)$'s to (a) $K^+\pi^0$ and (b) $K^0_s\pi^+$, respectively, summed over copper and lead target data with an empty target subtraction. The dashed lines represent the $\sin^2\theta$ shape expected for decays of coherently produced $K^{*+}(890)$'s and are normalized to the total number of events in each histogram.	161
44.	Acceptance corrected distribution of the life-time of K^0_s's (in its reference frame) found in the final state of the decay of coherently produced $K^{*+}(890)$'s on the copper and lead targets after an empty target subtraction. The dotted line is a result of a least squares fit for the K^0_s mean life described in the text.	164
45.	Acceptance corrected and normalized $K\pi$ mass spectra from the process $K^+A \to K\pi A$ for events with $-t' < 0.004$ Gev^2 . The smooth curve above each distribution gives the acceptance as a function of mass assuming a $\sin^2\theta\sin^2\phi$ decay distribution in the Gottfried-Jackson frame. The dashed curves represent fits to the data in the region between the arrows to a distorted Breit-Wigner form discussed in the text. Included are data from the detected final states $K^+\gamma\gamma$ and $\pi^+\pi^+\pi^-$ on copper, (a) and (b), respectively, and lead targets, (c) and (d), respectively, after a target empty subtraction.	168-171
46.	Completely corrected and normalized $-t'$ distributions for coherently excited $K^{*+}(890)$'s produced on the copper and lead targets and detected in the (a) $K^+\gamma\gamma$ and (b) $\pi^+\pi^+\pi^-$ final states. The dashed curves are fits to the data using the model described in the text.	180-181

CHAPTER I

INTRODUCTION

A. Introduction to Quantum Chromo-Dynamics

In recent years, the non-Abelian gauge theory of Quantum Chromo-Dynamics (QCD) has emerged as the best candidate for a description of Nature's strong interaction. The successes of the local gauge theory of the unified weak-electromagnetic interaction give credence to the assertion that strong forces can also be understood in terms of a local gauge invariance and hint that all forces may soon be describable in terms of matter and gauge fields invariant under an appropriate group of local gauge transformations.

According to QCD, the hadronic building blocks of nuclear matter are pictured as composite systems constructed from a fundamental n-tuplet of colored quarks (q), and a corresponding conjugate n-tuplet of antiquarks ($\bar{q}$).[1] These composite systems are envisioned to be bound by the influence of the exchange of colored gluonic gauge bosons among the constituent quarks, and can be phenomonologically grouped into multiplets of the unitary symmetry group SU(n).

Experimentally, there now exists direct evidence for five (n=5) types of flavors (labels of quark identity) of quarks (i.e. up (u), down (d), strange (s), charmed (c), and bottom (b)) with a sixth flavor (top) highly suspected on the grounds of a symmetry of

correspondence between quark and lepton generations as implied by the SU(2) ⊗ U(1) electro-weak unified field theory.[2] This suspicion ensues from the constraint of renormalizability which demands that in order for currents coupled to gauge fields to be free of triangle anomalies, the number of flavors must be identical to the number of leptons.

For the purposes of this work, only the "old" (i.e. pre 1974) quarks (u, d, s) need be considered and any discussion of $SU(n)_{flavor}$ will be restricted to the case n = 3.

The notion of color as a dynamical variable was introduced to explain many puzzles inherent to the original uncolored scheme.[3,4] First of all, it was required to solve the triality puzzle concerning the experimentally observed baryons and mesons. The fact that baryons could only be constructed from quark triplets (qqq) and the mesons from quark-antiquark pairs ($q\bar{q}$) indicated a deeper symmetry of Nature. The triality puzzle could be understood if hadrons were manifestly color singlets.

Color symmetry also explained the riddle of the existence of the low-lying baryons (e.g. Δ) whose spin structure, in principle, should forbid their existence by the Pauli Principle. Because the constituent quark wavefunction is symmetric in spin and isospin, color antisymmetry was required to ensure overall antisymmetry of the wavefunctions.

Color also provided a means for bringing the current algebra calculation of the $\pi^0 \to \gamma\gamma$ decay rate into agreement with experiment,

and for explaining the experimental ratio $R = \sigma(e^+e^- \to \text{hadrons})/\sigma(e^+e^- \to \mu^+\mu^-)$.

The local symmetry group of the strong interaction is taken to be $SU(3)_{color}$. The QCD gauge bosons exhibit exact SU(3) color symmetry and are grouped into an $SU(3)_{color}$ octet. These bosons couple only to color charges and are incapable of flavor discrimination.

Of the experimentally accessible systems for testing some of the basic precepts of this theory, mesonic systems present one of the simplest. The electromagnetic interaction between the quark and antiquark constituents of mesons is especially amenable to laboratory study in a high energy experiment.

B. Theoretical Models of Vector Meson Radiative Decays

Radiative decays of the sort $M_i(J_i^{P_i}) \to M_f(J_f^{P_f}) + \gamma$, where $M_{i,f}$ are the initial and final meson states of spin $J_{i,f}$ and parity $P_{i,f}$ are particularly enlightening probes of electromagnetic structure. Specifically, this radiative decay proceeds by means of the emission of ℓ-tuple electromagnetic radiation according to the selection rules

$$|J_f - J_i| = \ell \tag{1}$$

$$P_f = (-1)^{\ell} P_i \qquad \text{electric transition} \tag{2}$$

$$P_f = -(-1)^{\ell} P_i \qquad \text{magnetic transition} \tag{3}$$

Much theoretical investigation has been devoted to radiative decays of the sort $V(J^P=1^-) \to P(J^P=0^-) + \gamma$ within the framework of SU(3) unitary symmetry schemes,[5] simple quark models,[6,7,8] and vector dominance models.[9-12] Here V represents the SU(3) vector meson nonet and P are the members of the pseudoscalar nonet. According to the Rules (1)-(3), this reaction proceeds via a magnetic dipole (M1) transition.

The unitary symmetry scheme relates transition matrix elements $\langle V|m|P\gamma\rangle$ among like multiplets of the SU(3) classification, but its predictive power fails in the case of decays linking singlet to octet states or vice versa. A few specific relations relevant to this work are

$$\langle \rho|m|\pi\gamma\rangle = \langle K^{*\pm}|m|K^{\pm}\gamma\rangle$$

$$= -\frac{1}{2}\langle \overline{K^{o*}}|m|\bar{K}^{o}\gamma\rangle$$

$$= \frac{1}{\sqrt{3}}\langle \omega_8|m|\pi^{o}\gamma\rangle$$

Here $|\omega_8\rangle$ represents the pure octet member of the vector nonet possessing zero isospin (I) and zero hypercharge (Y).

The naive or simple quark model model makes identical predictions to the above, but also allows extension to decays untreatable by unitary symmetry techniques.

In this model, the M1 transition matrix element is taken to be of the form $\langle V|\vec{\mu}\cdot\vec{B}|P\gamma\rangle$, and the transition occurs via a spin flip of a constituent quark with magnetic moment $\vec{\mu}_i$ in the presence of

and for explaining the experimental ratio $R = \sigma(e^+e^- \to \text{hadrons})/\sigma(e^+e^- \to \mu^+\mu^-)$.

The local symmetry group of the strong interaction is taken to be $SU(3)_{color}$. The QCD gauge bosons exhibit exact SU(3) color symmetry and are grouped into an $SU(3)_{color}$ octet. These bosons couple only to color charges and are incapable of flavor discrimination.

Of the experimentally accessible systems for testing some of the basic precepts of this theory, mesonic systems present one of the simplest. The electromagnetic interaction between the quark and antiquark constituents of mesons is especially amenable to laboratory study in a high energy experiment.

B. Theoretical Models of Vector Meson Radiative Decays

Radiative decays of the sort $M_i(J_i^{P_i}) \to M_f(J_f^{P_f}) + \gamma$, where $M_{i,f}$ are the initial and final meson states of spin $J_{i,f}$ and parity $P_{i,f}$ are particularly enlightening probes of electromagnetic structure. Specifically, this radiative decay proceeds by means of the emission of ℓ-tuple electromagnetic radiation according to the selection rules

$$|J_f - J_i| = \ell \tag{1}$$

$$P_f = (-1)^{\ell} P_i \qquad \text{electric transition} \tag{2}$$

$$P_f = -(-1)^{\ell} P_i \qquad \text{magnetic transition} \tag{3}$$

Much theoretical investigation has been devoted to radiative decays of the sort $V(J^P=1^-) \to P(J^P=0^-) + \gamma$ within the framework of SU(3) unitary symmetry schemes,[5] simple quark models,[6,7,8] and vector dominance models.[9-12] Here V represents the SU(3) vector meson nonet and P are the members of the pseudoscalar nonet. According to the Rules (1)-(3), this reaction proceeds via a magnetic dipole (M1) transition.

The unitary symmetry scheme relates transition matrix elements $\langle V|m|P\gamma\rangle$ among like multiplets of the SU(3) classification, but its predictive power fails in the case of decays linking singlet to octet states or vice versa. A few specific relations relevant to this work are

$$\langle \rho|m|\pi\gamma\rangle = \langle K^{*\pm}|m|K^{\pm}\gamma\rangle$$

$$= -\frac{1}{2}\langle \overline{K^{o*}}|m|\bar{K}^{o}\gamma\rangle$$

$$= \frac{1}{\sqrt{3}}\langle \omega_8|m|\pi^{o}\gamma\rangle$$

Here $|\omega_8\rangle$ represents the pure octet member of the vector nonet possessing zero isospin (I) and zero hypercharge (Y).

The naive or simple quark model model makes identical predictions to the above, but also allows extension to decays untreatable by unitary symmetry techniques.

In this model, the M1 transition matrix element is taken to be of the form $\langle V|\vec{\mu}\cdot\vec{B}|P\gamma\rangle$, and the transition occurs via a spin flip of a constituent quark with magnetic moment $\vec{\mu}_i$ in the presence of

of the magnetic field $\vec{B}$ generated by the emitted photon. This is clearly a semi-classical treatment of the radiation field. Also, the additivity assumption[13]

$$\vec{\mu} = \sum_i \vec{\mu}_i \tag{4}$$

where the summation index i runs over the constituent quarks, has been invoked. Furthermore, the $q\bar{q}$ pairs in both the final and initial states are taken to be in the relative S-wave (ℓ=0) and, enlisting SU(6) symmetry,[14] the space parts of the meson wavefunctions $f_{V,P}(\vec{r})$ are taken to be identical.

Using standard spectroscopic notation (i.e. $^{2J+1}L_s$, where J is the total angular momentum, 2J+1 gives the number of magnetic substates, L is the orbital angular momentum, and s the spin angular momentum) in spin space the radiative decay $V \to P + \gamma$ can be expressed as $^3S_1 \to {}^1S_0 + \gamma$; i.e. the triplet state transforms to a singlet state with the emission of a photon.

A semi-classical treatment of the radiation field takes the magnetic field $\vec{B}$ in the transition matrix element to be a consequence of the vector potential $\vec{A}$ generated by the emitted photon.[15] The normalized form of the vector potential of a photon in the polarization state λ is given by

$$\vec{A} = \frac{1}{\sqrt{2k}}\,\hat{\epsilon}_\lambda e^{i\vec{k}\cdot\vec{r}} \tag{5}$$

where $\vec{\epsilon}$ is the unit polarization vector and $\vec{k}$ is the wave vector of the photon. Here, natural units of $\hbar = c = 1$ have been chosen and will be used throughout this thesis unless otherwise noted.

First, in order to calculate numerical values for pertinent transition rates using the quark model, the quark wavefunctions of the involved states are required. The states of interest include the $K^{*+}(890)$ and K^+ mesons, as well as the ω, ρ^+, $\overline{K^{0*}}$, π^0, π^+, and $\overline{K^0}$ mesons, required for later discussions; these wavefunctions are listed in Table I. In this table, u, d, and s are the flavor labels of the spin one-half spin states α, and β, the basis states with spin up and down, respectively. Also, $|\omega_1\rangle$ represents the I=Y=0 purely singlet member of the vector nonet. Only the S_z=1 states of the vector mesons are given.

Using Equations (4) and (5), the matrix element of the interaction Hamiltonian for the ith quark with emission of a photon in the polarization state λ is written as

$$m_i^\lambda = \frac{1}{\sqrt{2k}}\,\vec{\mu}_i\cdot(\vec{k}\times\hat{\epsilon}_\lambda)e^{i\vec{k}\cdot\vec{r}}$$

In the rest frame of the parent vector meson,

$$k = \frac{m_V^2 - m_P^2}{2m_V}$$

For $K^{*+} \to K^+\gamma$ decays, k = 309 MeV/c.

Taking $\vec{\mu}_i = \mu_i\vec{\sigma}$, where $\vec{\sigma}$ are the Pauli matrices, summing over constituent quarks and photon polarizations, and averaging over initial spin states of the vector meson, we have the reduced

TABLE I

Quark Wavefunctions of Pertinent Vector and Pseudoscalar Mesons

$S=1,\ S_z=1$:

$$|\omega_8\rangle = \frac{1}{\sqrt{6}}\,(\alpha_u\alpha_{\bar{u}} + \alpha_d\alpha_{\bar{d}} - 2\alpha_s\alpha_{\bar{s}})\,f(\vec{r})$$

$$|\omega_1\rangle = \frac{1}{\sqrt{3}}\,(\alpha_u\alpha_{\bar{u}} + \alpha_d\alpha_{\bar{d}} + \alpha_s\alpha_{\bar{s}})\,f(\vec{r})$$

$$|\rho^+\rangle = \alpha_u\alpha_{\bar{d}}\,f(\vec{r})$$

$$|K^{*+}\rangle = \alpha_u\alpha_{\bar{s}}\,f(\vec{r})$$

$$|\overline{K^{o*}}\rangle = \alpha_{\bar{d}}\alpha_s\,f(\vec{r})$$

$S=0,\ S_z=0$:

$$|\pi^o\rangle = \frac{1}{2}\,[(\alpha_u\beta_{\bar{u}} - \alpha_{\bar{u}}\beta_u) - (\alpha_d\beta_{\bar{d}} - \alpha_{\bar{d}}\beta_d)]\,f(\vec{r})$$

$$|\pi^+\rangle = \frac{1}{\sqrt{2}}\,(\alpha_u\beta_{\bar{d}} - \alpha_{\bar{d}}\beta_u)\,f(\vec{r})$$

$$|K^+\rangle = \frac{1}{\sqrt{2}}\,(\alpha_u\beta_{\bar{s}} - \alpha_{\bar{s}}\beta_u)\,f(\vec{r})$$

$$|\overline{K^o}\rangle = \frac{1}{\sqrt{2}}\,(\alpha_{\bar{d}}\beta_s - \alpha_s\beta_{\bar{d}})\,f(\vec{r})$$

transition rates:

$$\left(\sum_\lambda \left|\sum_i \langle v|m_i^\lambda|P\gamma\rangle\right|^2\right)_{\substack{\text{avg.}\\ \text{spin}}} = |\langle v|m|P\gamma\rangle|^2$$

These are tabulated in Table II for the decays of interest.

TABLE II

Reduced $V \to P\gamma$ Transition Rates

$$|\langle\omega_8|m|\pi^o\gamma\rangle|^2 = (1/9)k(\mu_u - \mu_d)^2$$

$$|\langle\omega_1|m|\pi^o\gamma\rangle|^2 = (2/9)k(\mu_u - \mu_d)^2$$

$$|\langle\rho|m|\pi\gamma\rangle|^2 = (1/3)k(\mu_u + \mu_d)^2$$

$$|\langle K^{*+}|m|K^+\gamma\rangle|^2 = (1/3)k(\mu_u + \mu_s)^2$$

$$|\langle\overline{K^{o*}}|m|\overline{K^o}\gamma\rangle|^2 = (1/3)k(\mu_d + \mu_s)^2$$

$$|\langle\omega|m|\pi^o\gamma\rangle|^2 = (1/3)k(\mu_u - \mu_d)^2$$

With the exception of the result for the decay $\omega_1 \to \pi^o\gamma$, the results tallied in Table II are all related through SU(3) symmetry predictions, if it is assumed that the μ_i are simply proportional to the quark charges. In the case of the ω, the quark model prediction is $\langle\omega_8|m|\pi^o\gamma\rangle = \frac{1}{\sqrt{2}}\langle\omega_1|m|\pi^o\gamma\rangle$.

TABLE I

Quark Wavefunctions of Pertinent Vector and Pseudoscalar Mesons

$S=1,\ S_z=1$:

$$|\omega_8\rangle = \frac{1}{\sqrt{6}}\,(\alpha_u\alpha_{\bar{u}} + \alpha_d\alpha_{\bar{d}} - 2\alpha_s\alpha_{\bar{s}})\,f(\vec{r})$$

$$|\omega_1\rangle = \frac{1}{\sqrt{3}}\,(\alpha_u\alpha_{\bar{u}} + \alpha_d\alpha_{\bar{d}} + \alpha_s\alpha_{\bar{s}})\,f(\vec{r})$$

$$|\rho^+\rangle = \alpha_u\alpha_{\bar{d}}\,f(\vec{r})$$

$$|K^{*+}\rangle = \alpha_u\alpha_{\bar{s}}\,f(\vec{r})$$

$$|\overline{K^{o*}}\rangle = \alpha_{\bar{d}}\alpha_s\,f(\vec{r})$$

$S=0,\ S_z=0$:

$$|\pi^o\rangle = \frac{1}{2}\,[(\alpha_u\beta_{\bar{u}} - \alpha_{\bar{u}}\beta_u) - (\alpha_d\beta_{\bar{d}} - \alpha_{\bar{d}}\beta_d)]\,f(\vec{r})$$

$$|\pi^+\rangle = \frac{1}{\sqrt{2}}\,(\alpha_u\beta_{\bar{d}} - \alpha_{\bar{d}}\beta_u)\,f(\vec{r})$$

$$|K^+\rangle = \frac{1}{\sqrt{2}}\,(\alpha_u\beta_{\bar{s}} - \alpha_{\bar{s}}\beta_u)\,f(\vec{r})$$

$$|\overline{K^o}\rangle = \frac{1}{\sqrt{2}}\,(\alpha_{\bar{d}}\beta_s - \alpha_s\beta_{\bar{d}})\,f(\vec{r})$$

transition rates:

$$\left(\sum_\lambda \left|\sum_i \langle v|m_i^\lambda|P\gamma\rangle\right|^2\right)_{\substack{\text{avg.}\\ \text{spin}}} = |\langle v|m|P\gamma\rangle|^2$$

These are tabulated in Table II for the decays of interest.

TABLE II

Reduced $V \to P\gamma$ Transition Rates

$$|\langle\omega_8|m|\pi^o\gamma\rangle|^2 = (1/9)k(\mu_u - \mu_d)^2$$

$$|\langle\omega_1|m|\pi^o\gamma\rangle|^2 = (2/9)k(\mu_u - \mu_d)^2$$

$$|\langle\rho|m|\pi\gamma\rangle|^2 = (1/3)k(\mu_u + \mu_d)^2$$

$$|\langle K^{*+}|m|K^+\gamma\rangle|^2 = (1/3)k(\mu_u + \mu_s)^2$$

$$|\langle\overline{K^{o*}}|m|\overline{K^o}\gamma\rangle|^2 = (1/3)k(\mu_d + \mu_s)^2$$

$$|\langle\omega|m|\pi^o\gamma\rangle|^2 = (1/3)k(\mu_u - \mu_d)^2$$

With the exception of the result for the decay $\omega_1 \to \pi^o\gamma$, the results tallied in Table II are all related through SU(3) symmetry predictions, if it is assumed that the μ_i are simply proportional to the quark charges. In the case of the ω, the quark model prediction is $\langle\omega_8|m|\pi^o\gamma\rangle = \frac{1}{\sqrt{2}}\langle\omega_1|m|\pi^o\gamma\rangle$.

In deriving these results, the overlap integral $\int d^3r f_V^*(\vec{r}) f_P(\vec{r})$ has been set to unity. Actually, the integral of interest is $\int d^3r f_V^*(\vec{r}) e^{i\vec{k}\cdot\vec{r}} f_P(\vec{r}) = \int d^3r f_V^*(\vec{r}) \cos(\vec{k}\cdot\vec{r}) f_P(\vec{r})$.[16] As both initial and final states are s-waves, only the even part of $e^{i\vec{k}\cdot\vec{r}}$ contributes. This gives $\int d^3r f_V^*(\vec{r}) \cos(\vec{k}\cdot\vec{r}) f_P(\vec{r}) = 1 + k^2/6\langle r^2\rangle + O(k^4 \langle r^4\rangle)$. Taking $\langle r^2\rangle_{K^+} = 0.26 \pm 0.07\ \mathrm{fm}^2$,[17-19] we have for $K^{*+} \to K^+\gamma$ decays $k^2/6\langle r^2\rangle = 0.11 \pm 0.03$. So, the static or long wavelength approximation of setting this integral to unity (i.e. where recoil effects are neglected) is only partially valid.

Employing Fermi's Second Golden Rule,[20] we get for the $V \to P\gamma$ decay widths

$$\Gamma(V \to P\gamma) = 2\pi\rho\left|\langle V|m|P\gamma\rangle\right|^2$$

where ρ is the density of accessible final states.

It remains unclear whether a relativistic or nonrelativistic treatment for the density of states is appropriate. Both forms will be investigated. They are:

$$\rho = \frac{4\pi k^2}{(2\pi)^3}\ \frac{E_P}{m_V} \qquad \text{(non-relativistic)}$$

$$\rho = \frac{4\pi k^2}{(2\pi)^3} \qquad \text{(relativistic)}$$

where $E_P = (m_P^2 + k^2)^{1/2}$ is the energy of the final state pseudoscalar meson.

So, finally, we have,

$$\Gamma(V \to P\gamma) = \frac{k^2}{\pi}\left|\langle V|m|P\gamma\rangle\right|^2 \frac{E_P}{m_V} \quad \text{(non-relativistic)} \tag{6}$$

$$= \frac{k^2}{\pi}\left|\langle V|m|P\gamma\rangle\right|^2 \quad \text{(relativistic)} \tag{7}$$

Of the decays under study here, only the transition $\omega \to \pi^0\gamma$ is effected by problems associated with octet-singlet mixing. The physical vector nonet isoscalars ω and ϕ are taken as a linear combination of the pure singlet ($|\omega_1\rangle$) and pure octet ($|\omega_8\rangle$ states.

$$\omega = \cos\theta_V \omega_1 + \sin\theta_V \omega_8$$

$$\phi = -\sin\theta_V \omega_1 + \cos\theta_V \omega_8$$

Here θ_V is the vector nonet mixing angle, and has been determined to be $40 \pm 1°$ from the quadratic mass formula.

If ideal mixing ($\theta_V = \tan^{-1} 1/\sqrt{2} = 35.3°$) is assumed, the strange quark content of the ω vanishes, and the ϕ becomes populated solely by strange quarks. (Again, only the $s_z=1$ states are given.)

$$|\omega\rangle = \frac{1}{\sqrt{2}}(\alpha_u\alpha_{\bar{u}} + \alpha_d\alpha_{\bar{d}}) f(\vec{r})$$

$$|\phi\rangle = \alpha_s\alpha_{\bar{s}} f(\vec{r})$$

This assumption shall be adopted in the remainder of this discussion and gives rise to the final entry in Table II.

C. Theoretical Predictions for Radiative Decay Rates

There are many avenues of approach in utilizing the quark model formalism to make numerical predictions for decay rates. One can calculate raw rates without any reference to other experimentally determined radiative widths. One technique is to assume that the quark magnetic moments are proportional to the quark charges (i.e. that the photon is a U-spin scalar). As deduced from measurements of the proton and neutron magnetic moments, we have $\mu_i = \left(\frac{e_i}{e}\right) \mu_p$, where $\mu_p = \frac{2.79e}{2M_p}$ is the proton magnetic moment, e is the electron charge, M_p is the mass of the proton, and e_i are the quark charges ($e_{u,d,s}$ = 2/3e, -1/3 e, -1/3 e). This result is then used in Equations (6) and (7) to make predictions of widths. This approach assumes exact SU(3) symmetry.

Alternatively we may use experimentally derived values for μ_i as deduced from measurements of baryon magnetic moments.[21] This method rests on an implicit assumption of SU(3) symmetry breaking which may be phenomenologically understood by assigning different masses to the different quarks.[22] Experimentally, μ_u=1.852 μ_N, μ_d=-0.972 μ_N, and μ_s=-0.614±0.005 μ_N, where μ_N is the nuclear magneton.[23-26] These results imply, through the relation $\mu_i = \frac{e_i}{2m_i}$ (assuming quarks are point-like Dirac particles), that $m_u \approx m_d \neq m_s$.

There are also indications that higher order QCD corrections to the simple quark spin flip picture presented so far may be important. In the absence of a reliable calculation of these corrections, one can assign effective magnetic moments to the quarks,

and in this manner modify the relations between quark magnetic moments prescribed by exact SU(3) symmetry presented earlier.[27,28]

Predictions for $V \to P\gamma$ decay widths from these alternate approaches are given in Table III.[29] The latest experimental numbers are also listed for comparison.

Another approach is to use one well-determined radiative width, such as for $\omega \to \pi^0\gamma$, and extrapolate it to other decays via the previously developed formalism. This works best for kinematically similar decays such as for the $\rho \to \pi\gamma$ decay when the width $\Gamma(\omega \to \pi^0\gamma)$ is used as the starting value. Under such circumstances phase space factors and other kinematic corrections can be ignored due to the near identity of masses of the ω and ρ. In this case, the prediction is $\Gamma(\rho \to \pi\gamma)/\Gamma(\omega \to \pi^0\gamma) = 1/9$ for unviolated SU(3).

It is apparent that in the non-strange sector of vector meson radiative decays, the theoretical predictions are in reasonable agreement with experimentally derived results, and a reasonably self-consistent picture of these decays has emerged. This can be contrasted to the state of confusion existing a few years ago before our group's measurement of $\Gamma(\rho \to \pi\gamma)$.[30]

Extending the previous technique to decays of the strange vector mesons, we have in the limit of exact SU(3) symmetry $\Gamma(\overline{K^{0*}} \to \overline{K^0}\gamma)/\Gamma(K^{*+} \to K^+\gamma) = 4.0$. For broken SU(3), and using non-relativistic phase space, this ratio becomes 1.64. Carithers et al found $\Gamma(K^{0*} \to K^0\gamma) = 75 \pm 35$ keV.[31] This measurement implies a value of 19 ± 9 keV for $\Gamma(K^{*+}(890) \to K^+\gamma)$ in the limit of exact

TABLE III

Quark Model Predictions for Widths of Pertinent Radiative Decays

Decay	Exact SU(3)		Broken SU(3)		Experimental rates
	non-relativistic phase space	relativistic phase space	non-relativistic phase space	relativistic phase space	
$\omega \to \pi^0\gamma$	613 keV	1.18 MeV	626 keV	1.21 MeV	789 ± 92 keV
$\rho^+ \to \pi^+\gamma$	64 keV	123 keV	57 keV	110 keV	71 ± 7 keV
$K^{*+} \to K^+\gamma$	46 keV	69 keV	81 keV	122 keV	51 ± 5 keV*
$\overline{K^{0*}} \to \overline{K^0}\gamma$	183 keV	282 keV	133 keV	204 keV	75 ± 35 keV

*As reported in this work.

SU(3) symmetry, and a value of 46 ± 21 keV if SU(3) violation is estimated from measurements of baryon magnetic moments. In Table IV, predictions for the pertinent radiative widths are presented using the experimentally determined widths for $\omega \to \pi^0\gamma$ and $\rho^+ \to \pi^+\gamma$ as input, and extrapolating by means of the quark model formalism to the other decays.

This thesis reports a measurement of $\Gamma(K^{*+}(890) \to K^+\gamma) = 51 \pm 5$ keV. Discussion of this result and its implications will be postponed until Chapter VII.

D. Outline of Thesis

In Chapter II, an introduction to the theory and phenomenology of coherent production processes on complex nuclei are presented. Both the electromagnetic and strong production mechanisms contributing to coherent $K^{*+}(890)$ production are discussed, and their relation to the experimentally measured differential cross sections is described.

In Chapter III, the experimental apparatus and technique are described. First, the beam, the kaon enhancement mechanism, and the targets used are elucidated. Following this are descriptions of the target counter arrangement, the charged particle wire chamber spectrometer, and the liquid argon photon calorimeter (LAC). Finally, the intricacies of the trigger logic for each of the detected final states resulting from $K^{*+}(890)$ decay, and the beam sampling triggers set-up to monitor variations in beam flux are explored.

TABLE IV

Extrapolated Predictions for $V \to P\gamma$ Partial Widths Using Experimental Input

Decay	Exact SU(3)		Broken SU(3)	
	non-relativistic phase space	relativistic phase space	non-relativistic phase space	relativistic phase space
(using $\Gamma(\omega \to \pi^0\gamma) = 789 \pm 92$ keV as input[32])				
$\rho^+ \to \pi^+\gamma$	84 ± 10 keV	84 ± 10 keV	73 ± 9 keV	73 ± 9 keV
$K^{*+} \to K^+\gamma$	60 ± 7 keV	47 ± 5 keV	104 ± 12 keV	81 ± 9 keV
$\overline{K^{0*}} \to \overline{K^0}\gamma$	242 ± 28 keV	190 ± 22 keV	172 ± 20 keV	135 ± 16 keV
(using $\Gamma(\rho^+ \to \pi^+\gamma) = 71 \pm 7$ keV as input[33])				
$\omega \to \pi^0\gamma$	669 ± 66 keV	670 ± 66 keV	767 ± 76 keV	768 ± 76 keV
$K^{*+} \to K^+\gamma$	51 ± 5 keV	40 ± 4 keV	101 ± 10 keV	79 ± 8 keV
$\overline{K^{0*}} \to \overline{K^0}\gamma$	205 ± 20 keV	162 ± 16 keV	167 ± 16 keV	132 ± 13 keV

Chapter IV deals with the calibration of the spectrometer. The analysis used in determining the alignment parameters and physical positions of the various spectrometer elements is given followed by the method of calibrating the drift wire chamber (DWC) system. The performance of this system is also discussed. Following this, the determination of the energy scale is described with emphasis on the calibration of the momentum analyzing magnet and the LAC.

The major thrust of the data analysis is presented in Chapter V. Beam flux correction factors are examined, as are acceptance corrections and the final normalization of $K^{*+}(890)$ cross sections to beam kaon decays. Also, the efficacy of the Monte Carlo program is explored via a detailed comparison of Monte Carlo and real data results for beam kaon decays. The $K^{*+}(890)$ data is closely scrutinized with particular attention given to empty target subtractions, backgrounds, calculations of nb equivalents for one event, and determination of final experimental cross sections.

Fitting of the experimental differential cross sections and other experimental distributions of interest for the various targets and final states are presented in Chapter VI. A three parameter model including the radiative width of the $K^{*+}(890)$ is employed in fitting the experimental -t' distribution.

Chapter VII is devoted to a discussion of systematic errors associated with the resulting solutions for the extracted radiative width of the $K^{*+}(890)$. Final results, their consistency, and a comparison with previous results are also presented there.

CHAPTER II

COHERENT NUCLEAR PRODUCTION

A. Introduction

Coherent nuclear production is defined as the reaction $a + A \rightarrow a^* + A$, where a and a* are the incident high energy particle and the outgoing excited state, respectively. A represents the target nucleus in its ground state, or in a well-defined low-lying excited state.[34] In the present experimental study, a is identified with an incident K^+ of momentum 200 GeV/c, a* with the produced $K^{*+}(890)$, and A with either a copper or a lead nucleus. Reactions employing nuclear targets are useful in studying reactions with small cross sections on individual nucleons because of the production enhancement afforded by the constructive superposition of nucleon production amplitudes. Strict selection rules also apply for nuclear production which can help to suppress uninteresting production channels.[35]

Following Glauber,[36] coherent production of particles on complex nuclei by high energy incident particles is assumed to be a sequence of multiple interactions in the target nucleus taking place through single interactions with one or more target nucleons. Multiple interactions with single target nucleons are ignored, and in the limit of medium to heavy nuclei, correlations between nucleons in the nuclear wavefunction are deemed negligible.

The basic assumption of the Glauber model, which is known to work very well for elastic scattering of particles off nuclei[37], is that the S matrix for the particle a - nucleus A scattering is given by the product $S_1 \ldots S_N$ of the scattering matrices of the particle a on individual nucleons S_i. In other words, the nuclear production amplitude is equal to the coherent superposition of production off individual nucleons.

The quantum numbers exchanged in our specific coherent process are those of the photon. The reaction can proceed via one-photon exchange (Coulombic or Primakoff production), and also through the strong interaction. In order for this reaction to go strongly, selection rules restrict the class of final state particles a*. Care must be taken to separate these two contributions, and to understand their subsequent interference.[38]

Such reactions lend themselves well to experimental studies of the radiative decays of the ordinary, low-lying vector and tensor mesons. This is a consequence of the characteristic sharp, forward, peak in production cross sections for Coulombic production. These cross sections are directly proportional to the radiative decay width $\Gamma(a^* \rightarrow a\gamma)$ of the excited particle a*. Direct measurements of the reaction $K^{*+}(890) \rightarrow K^+\gamma$, for example, are experimentally very difficult because of the small branching ratio ($\sim$ 0.10%) of this decay channel, and also because of severe ambiguities that can arise in isolating this decay from the more predominant (B.R. = 33%)$K^+\pi^0$ final state of $K^{*+}(890)$ decay where one photon from the $\pi^0 \rightarrow 2\gamma$ decay

may go undetected, or the two photons may appear as one in the experimental detector.

At high energies, strong production is small in this forward Coulombic region. However, as the production angle increases the relative strengths of these two mechanisms reverse in importance. The region of rough equality of strength (interference region) allows a determination of the relative phase between the two production amplitudes. Separation of these two effects is best done at high energies. This was the impetus for our group's measurement of the coherent production of $K^{*+}(890)$ at a laboratory energy of 200 GeV.

The associated kinematic variables for coherent nuclear production are shown in Figure 1a. Energy and momentum conservation can be expressed in terms of four-vectors as $\mathbb{P}_a + \mathbb{P}_A = \mathbb{P}_{a^*} + \mathbb{P}_{A'}$ where the fourth component of $\mathbb{P}$ gives the particle energy, and the first three give the components of the momentum vector. Figure 1b shows the diagram for Primakoff production of a^*.

From the participating four-vectors we can form the Lorentz scalars $s = (\mathbb{P}_a + \mathbb{P}_A)^2 = (\mathbb{P}_{a^*} + \mathbb{P}_{A'})^2$ = square of the center-of-mass energy, and $q^2 \equiv t = (\mathbb{P}_a - \mathbb{P}_{a^*})^2 = (\mathbb{P}_{A'} - \mathbb{P}_A)^2$ = square of the four-momentum transfer. The squared norm of the space components of q^2 can be decomposed into transverse and longitudinal components relative to the momentum vector of particle a, which defines the z-direction, as $|\vec{q}|^2 = q_t^2 + q_z^2$.

a) Laboratory System

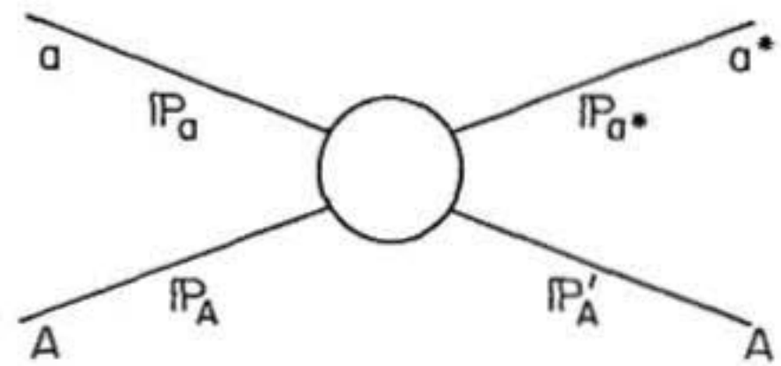

$\mathbb{P}_a = (\vec{P}_a, E_a)$ $\qquad$ $\mathbb{P}_A = (0, M_A)$

$\mathbb{P}_{a^*} = (\vec{P}_{a^*}, E_{a^*})$ $\qquad$ $\mathbb{P}'_A = (\vec{q}, E_{A'})$

$q = (\vec{q}, E_{A'} - M_A)$

b)

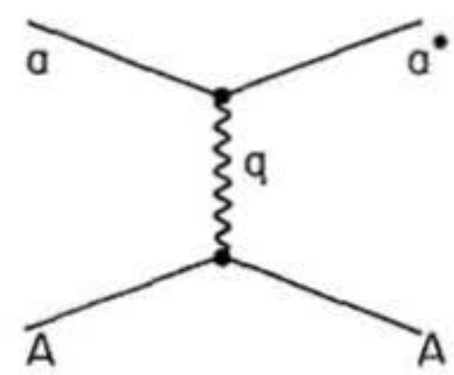

Figure 1

From energy-momentum conservation at the nucleus vertex we have

$$q^2 = 2m_A(m_A - E_{A'}) = -2m_A q_o \qquad (8)$$

where q_o is the relativistic kinetic energy imparted to the nucleus. Similarly, at the a-a* particle vertex we have $\mathbb{P}_a = \mathbb{P}_{a*} + q$. Squaring this it follows that

$$q_z = \frac{m_{a*}^2 - m_a^2 - q^2(1 + E_a/m_A)}{2P_a} \qquad (9)$$

In order for this reaction to proceed by coherent excitation, in which the structure of the nucleus is not probed beyond its gross dimensions, and the influence of individual nucleuons cannot be resolved, the following criterion must hold:

$$|\vec{q}|\ R \lesssim 1$$

where R is the nuclear radius. Taking $R = 1.2\ A^{1/3}$ fm, where A is the atomic number of the nucleus, this restriction becomes

$$|\vec{q}| \lesssim 1/1.2\ A^{1/3} \qquad (10)$$

For a lead nucleus (A = 207) this implies $|\vec{q}| \lesssim 28$ MeV/c, and it is obvious that coherence severely limits momentum transfers to small values.

This coherence condition used in conjunction with Equation (8) implies $q_o/|\vec{q}| \approx |\vec{q}|/2m_A \ll 1$. A recoiling lead nucleus could have at most a kinetic energy of $q_o \approx 4$ keV, and still satisfy the coherence condition. Using these results in Equation (9), the longitudinal

momentum transfer is small, and independent of nuclear target. For $K^{*+}(890)$ coherent production at 200 GeV/c, we have $q_z = 1.4$ MeV/c.

The kinematical minimum four-momentum transfer for production of particle a* is given by $q_{min} = \frac{m_{a*}^2 - m_a^2}{2P_a}$. For $K^{*+}(890)$ production this is 1.4 MeV/c at 200 GeV/c, and we see that, in general, using the previously derived results, that $q_z \approx q_{min}$. Furthermore, for the relation $q_{min}R \lesssim 1$ to hold, high energy incident particles are required.

Making the correspondence $t_{min} = q_{min}^2$, defining $t' \equiv t - t_{min}$, and noticing that $t_{min} = -\left[\frac{m_{a*}^2 - m_a^2}{2P_a}\right] = -q_z^2$, we can write

$$t' = q_o^2 - q_t^2 - q_z^2 + q_z^2 = -q_t^2$$

or $-t' = q_t^2$. Thus, $-t'$ is just the square of the transverse momentum transfer, which in the high energy limit of small momentum transfers is given simply by $q_t \approx P\theta$, where P is the laboratory momentum of particles a and a*, and θ is the scattering angle.

The condition $t < 0$, required by momentum-energy conservation, guarantees that any virtual particles exchanged in the scattering process are space-like. In the case of an exchanged virtual photon, $m_\gamma^2 < 0$; however, the coherence restriction forces it to be very nearly real, so $m_\gamma^2 \approx 0$.

This section is concluded with a discussion of the expected angular distributions of the $K^{*+}(890)$ decay products. In the rest frame of the excited $K^{*+}(890)$ (see Figure 2a), the incident

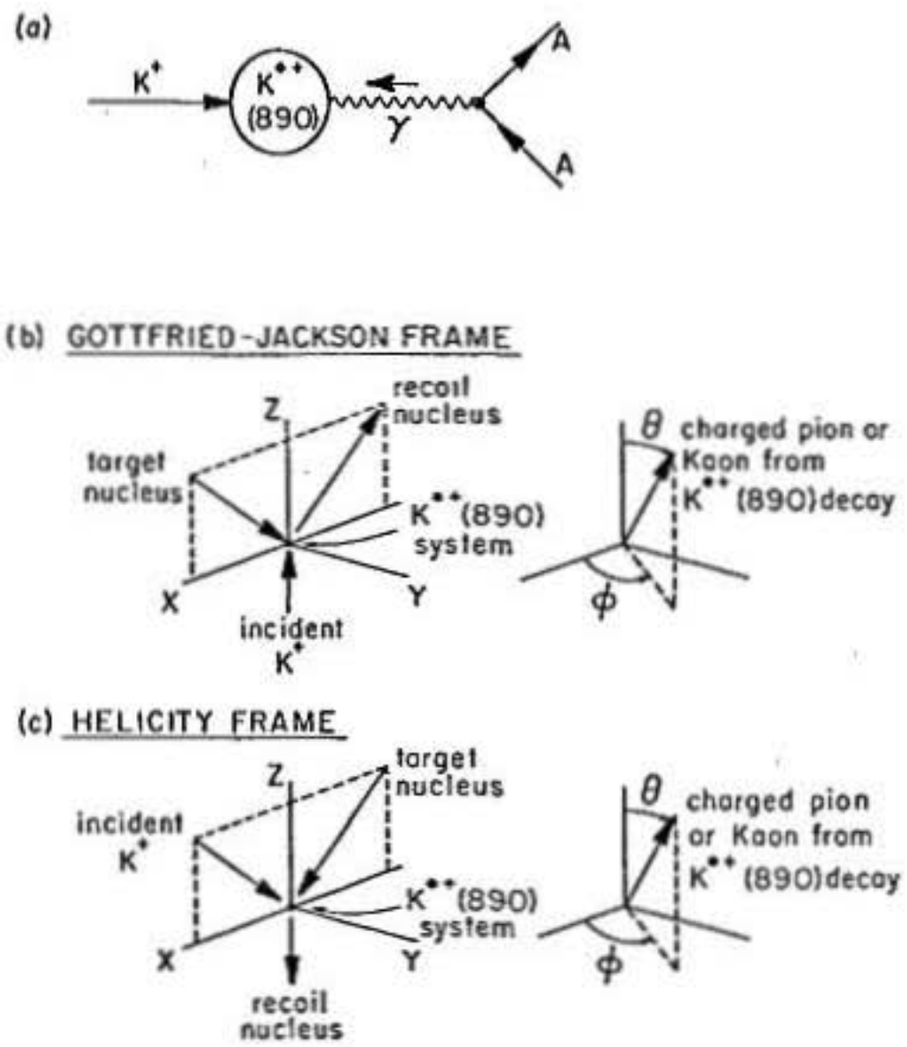

Figure 2

pseudoscalar K^+ can be taken to be a plane wave, and can be decomposed in terms of the spherical harmonics, $Y_\ell^0(\theta,\phi)$. Here, reference is made to the Gottfried-Jackson frame, where the y-axis is orthogonal to the production plane, the z-axis is defined by the incident K^+, and the angles θ and ϕ are the polar and azimuthal angles. Since the photon has spin one, but only two helicity states, in Primakoff excitation the $K^{*+}(890)$ can only couple to these helicity states. They are described by the spherical harmonics $Y_1^1(\theta,\phi)$ and $Y_1^{-1}(\theta,\phi)$. Primakoff production of the $K^{*+}(890)$ in its rest frame is pictured in Figure 2a.

For the case of strong excitation of the K^{*+}, it will shortly be shown that only an exchanged virtual, isoscalar, vector meson (ω) will be permitted. Although the ω admits three helicity states, only those with non-zero projection can couple to the incoming K^+ plane wave to yield the J=1 $K^{*+}(890)$.

Figure 2b depicts the Gottfried-Jackson frame with the trajectory of the charged kaon or pion resulting from $K^{*+}(890) \to K^+\pi^0$ or $K_S^0\pi^+$ defining the angles θ and ϕ. In this frame, both the incident K^+ and the exchanged particle travel along the z-axis. The distribution of these angles should follow the form $|Y_1^1(\theta,\phi) + Y_1^{-1}(\theta,\phi)|^2 \propto \sin^2\theta\sin^2\phi$. Evidence that it does is a strong indication that coherently produced $K^{*+}(890)$'s have been isolated. Also shown in Figure 2c is the helicity reference frame. This will be useful in examining the angular distributions of beam K^+ decays. In this case, the z-axis is defined along the momentum vector of the decaying particle, and the y-axis is again orthogonal to the

production plane.

B. Primakoff Production

The Primakoff mechanism for coherent production in the nuclear Coulomb field was first proposed as a means of measuring the π^o lifetime by using a photon beam incident on nuclear targets.[39] In this situation, the production cross section for π^o's is directly proportional to the π^o lifetime and scales with the square of the target nuclear charge Z.[40]

This same technique has been applied to the coherent excitation of 200 GeV/c K^+'s to $K^{*+}(890)$'s. The production cross section in this case is related to the radiative decay width of the $K^{*+}(890)$, $\Gamma(K^{*+}(890) \to K^+\gamma)$.[41,42] Hence, we have studied the inverse process $K^+ + \gamma_v \to K^{*+}(890)$, where the virtual photon γ_v is supplied by the nuclear Coulomb field. The rate of this reaction is guaranteed to be identical to that of the decay $K^{*+}(890) \to K^+\gamma$ by detailed balance.

The cross section for Primakoff excitation of $K^{*+}(890)$'s is written as [38,43,44,45]

$$\frac{d^2\sigma}{dtdm^2} = |F_c(t,m)|^2 = \frac{Z^2\alpha}{\pi} \frac{\sigma_\gamma(m^2)}{m^2 - m_K^2} \frac{t-t_{min}}{t^2} |f_c(t)|^2 \qquad (11)$$

where Z is the charge of the nuclear target, $\alpha = \frac{e^2}{4\pi} = 1/137$ is the fine structure constant, $\sigma_\gamma(m^2)$ is the photoproduction cross section for $K^{*+}(890)$'s on a K^+ target at the center of mass energy m , and $f_c(t)$ is the nuclear form factor with modifications to take into account scattering of the incident and outgoing states in and around

the nucleus. More will be said of this in Chapter VI.

The factor $1/t^2$ is representative of the photon propagator and causes the production to be very strongly peaked towards forward directions. However, at $t=t_{min}$, where the incident and outgoing particle trajectories are parallel, the cross section vanishes as required by current conservation.[44]

For photoproduction of the state a* of mass m, which we assume may be a resonant state of finite width, off the target a, we can write

$$\sigma_\gamma(a + \gamma \to a^*) = \frac{2\pi}{q^{*2}} \frac{(2J_{a^*} + 1)}{2(2J_a + 1)} \cdot |T(\gamma a \to a^*)|^2 \qquad (12)$$

where $q^* = \frac{m^2 - m_a^2}{2m}$ is the momentum of the photon in the a* center-of-mass system, J_a and J_{a^*} are the spins of a and a*, respectively, and $T(\gamma a \to a^*)$ is the T-matrix element.

For the case of a vector particle of resonant mass m_o decaying into two pseudoscalars, we use the relativistic form for the T-matrix[46]

$$T = \frac{m_o \Gamma_x^{1/2}(m) \Gamma_{a\gamma}^{1/2}(m)}{(m^2 - m_o^2) + i(m_o \Gamma_{tot}(m))} \qquad (13)$$

Here, $\Gamma_x(m)$ in the numerator represents the mass dependent partial width $\Gamma_x(a^* \to x)$ for the detected final state x, and $\Gamma_{tot}(m)$ in the denominator is the mass dependent total width $\Gamma_{tot}(a^* \to \text{anything})$; $\Gamma_{a\gamma}$ is the partial width for the decay $a^* \to a\gamma$. Since the K*(890) decays almost exclusively to $K\pi$ (B.R. > 99%), we will take $\Gamma_x(m) = \Gamma_{tot}(m)$. The discussion of the functional

form of the $\Gamma(m)$ will be delayed until Chapter VI.

Combining Equations (11), (12) and (13), the result

$$\frac{d^2\sigma}{dtdm^2} = 8\pi Z^2\alpha \frac{(2J_{a^*}+1)}{(2J_a+1)} \frac{m^2}{(m^2-m_a^2)^3} \Gamma(a^* \to a\gamma) \frac{t-t_{min}}{t^2} |f_c(t)|^2$$

$$\cdot \left[\frac{1}{\pi} \frac{m_o\Gamma_{tot}(m)}{(m^2-m_o^2)^2 + (m_o\Gamma_{tot}(m))^2}\right] \cdot m_o \qquad (14)$$

follows.

In the limit $\Gamma_{tot}(m) \to 0$, the Breit-Wigner term above becomes $\delta(m^2 - m_o^2)$, and the well known Primakoff production cross section formula is retrieved:[45]

$$\frac{d\sigma}{dt} = 8\pi Z^2\alpha \frac{(2J_{a^*}+1)}{(2J_a+1)} \left(\frac{m_{a^*}}{m_{a^*}^2 - m_a^2}\right)^3 \Gamma(a^* \to a\gamma) \frac{t-t_{min}}{t^2} |f_c(t)|^2$$

The form factor $f_c(t)$ depends on the nuclear charge distribution, and the effect of scattering or absorption of incident and outgoing particles whose impact parameters are less than or equal to the radius of the nucleus. At high energies and low momentun transfers, the bulk of Coulomb production is expected to take place outside the nucleus. Therefore, $f_c(t)$ depends on the gross nuclear structure or size, and only weakly on scattering or absorption effects. Therefore, for the following discussion we can take the variation of $f_c(t)$ in the very forward region to be approximately zero.

The following consequences immediately follow:

(i) As noted earlier, the production cross-section vanishes in the forward direction, then rises steeply to a maximum at $t=2t_{min}$; at larger values of t it falls off as 1/t.

(ii) The position of the maximum is independent of the target nucleus and its height grows as $Z^2P_a^2$.

(iii) The integrated cross section increases as $Z^2 \ln P_a$ as P_a tends to infinity and, because meson exchange contributions to coherent production cross-sections tend to fall at least as rapidily as $1/P_a$, the Coulomb contribution to coherent production becomes the dominant mechanism at high energies.

C. Coherent Strong Excitation

Coherent strong production of the $K^{*+}(890)$ on complex nuclei is expected to be dominated by ω exchange. In principle, exchange of the vacuum pole is permitted; however, no experimental indication of this contribution has ever been seen. This can be understood assuming that the Pomeron has vacuum quantum numbers and therefore could not provide a $J^P = 0^- \to 1^-$ transition.

We can also consider exchange of other Regge trajectories. Experimental data on the reaction $K^+ + p \to K^{*+}(890) + p$ indicate that the t-channel exchanges are isoscalar, and have natural parity (i.e. $J^P = 0^+, 1^-, 2^+, \ldots$), and that these results can be described qualitatively in terms of a simple ω-f^o exchange degenerate Regge pole analysis.[47] In the limit of large s, using the single particle

exchange model,[48] it is sufficient to consider only ω exchange as contributing to the strong coherent production on nuclear targets.

The purely strong contribution to coherent production is then given by:[38]

$$\frac{d^2\sigma}{dtdm^2} = |F_s(t,m)|^2 = A^2 C_s(t-t_{min})|f_s(t)|^2 \cdot BW \qquad (15)$$

where A is the nucleon number of the target nucleus, C_s is the normalization to production on a single nucleon, $f_s(t)$ is the nuclear form factor, which contains effects of scattering and absorption, and BW is given by the bracketed term in Equation (14).

The form factor $f_s(t)$ is numerically evaluated utilizing a detailed optical model calculation in which the distribution of nuclear matter in the nucleus is assumed to be of the same form as its charge distribution. Details are found in Chapter VI.

Neglecting corrections to $f_s(t)$ for the moment, and assuming that the nuclear matter density can be approximated by $\rho(r) \propto e^{-(r/R)^2}$ for illustrative purposes, then we have $f_s(t) \propto e^{-tR^2/4}$, and the following results concerning the strong coherent cross section of Equation (15) ensue:

(i) It vanishes in the forward direction, rises to a peak at $t=4/R^2$ (taking R to be the radius of a lead nucleus, the peak occurs at $t=0.003\ GeV^2$) and then, for the case of a uniform density distribution, slowly oscilates according to $|f_s(t)|^2$ with the amplitudes of oscillation falling as t^{-1}.

(ii) The position of the maximum is essentially independent of the incident momentum (it enters only through t_{min}, which goes to zero as P_a increases), and its height goes as $A^{4/3}P_a^{-1}$. Here use has been made of the prediction of Regge theory that at small values of t, $C_s \propto P_a^{2(\alpha_o-1)}$ and also of the fact that for the ω-trajectory, $\alpha_o \simeq 0.5$.

(iii) The integrated hadronic cross section behaves like $A^{2/3}P_a^{-1}$, thus providing further advantage in isolating Coulomb production at high energies.

D. Theoretical Coherent Production Cross Sections

The total coherent production amplitude is a coherent sum of the electromagnetic, $F_c(t,m)$, and hadronic, $F_s(t,m)$, amplitudes. The theoretical differential cross section can be written as

$$\frac{d^2\sigma}{dt'dm^2} = |F_c(t,m) + e^{i\theta} F_s(t,m)|^2 + \left.\frac{d^2\sigma}{dt'dm^2}\right)_{incoherent} \qquad (16)$$

where we have included an incoherent contribution to $K^{*+}(890)$ production, and θ is the relative phase between the Coulomb and strong amplitudes.

Here we have adopted the convention of writing the differential cross section in terms of t' since $\frac{d}{dt} = \frac{d}{dt'}$ and $-t' = q_t^2$, where q_t is the experimentally measured quantity for each $K^{*+}(890)$ event.

The experimental triggers (see Chapter III) strongly suppressed incoherent reactions and states involving nuclear excitations.

Consequently, because the incoherent contribution to the $K^{*+}(890)$ sample was expected to be small, ab initio, it was ignored in the analysis. We also assumed that non-resonant $K\pi$ production in the $K^{*+}(890)$ region (0.790 MeV < $m_{K\pi}$ < 0.990 MeV) was not important.

In Chapter VI, Equation (16) will be integrated over m^2, and t', to get expressions for the forms

$$\frac{d\sigma}{dt'} = \int dm^2 \frac{d^2\sigma}{dt'dm^2} \tag{17}$$

and

$$\frac{d\sigma}{dm} = 2m \int dt' \frac{d^2\sigma}{dt'dm^2} \tag{18}$$

respectively.

The experimental data, expressed separately as differential cross sections in t' and m, will be fit to these expressions. The different t' dependences of the Coulomb and ω exchange production mechanisms will allow an extraction of their strengths (proportional to $\Gamma(K^{*+}(890) \to K^+\gamma)$ and C_s, respectively), as well as the phase angle between their amplitudes, by means of fits to Equation (17). Equation (18) will be applied to the data in order to extract the Breit-Wigner line shape parameters, m_o and $\Gamma(m_o)$ for the $K^{*+}(890)$ resonance.

CHAPTER III

EXPERIMENTAL SET-UP

A. The Beam Line

The forward, high resolution spectrometer used in this study of the radiative width of the $K^{*+}(890)$ meson was set-up in the east leg of the M1 secondary beam line of the Meson Lab at Fermilab.

After injection and acceleration to a momentum of 400 GeV/c in the Fermilab pulsed proton synchrotron, primary protons ($\lesssim 2 \times 10^{13}$ protons per pulse) were extracted from the main ring, over a one second "flat top", and transported to the switchyard area where they were apportioned among the Neutrino, Proton, and Meson Labs. Typically, $\sim 10^{12}$ protons were delivered to the Meson-Center target (15 inches of beryllium; 1.25 proton collision lengths) in which the secondary particles to be transported through the M1 beam line were produced.

A schematic representation of the M1 beam line is given in Figure 3. The acceptance of this beam line was $\sim$1 μster for secondaries produced between 3.6 mrad and 1.9 mrad relative to the incident proton beam. Most of our data was taken at a production angle of $\lesssim$ 2.5 mrad, this setting being a compromise with other competing

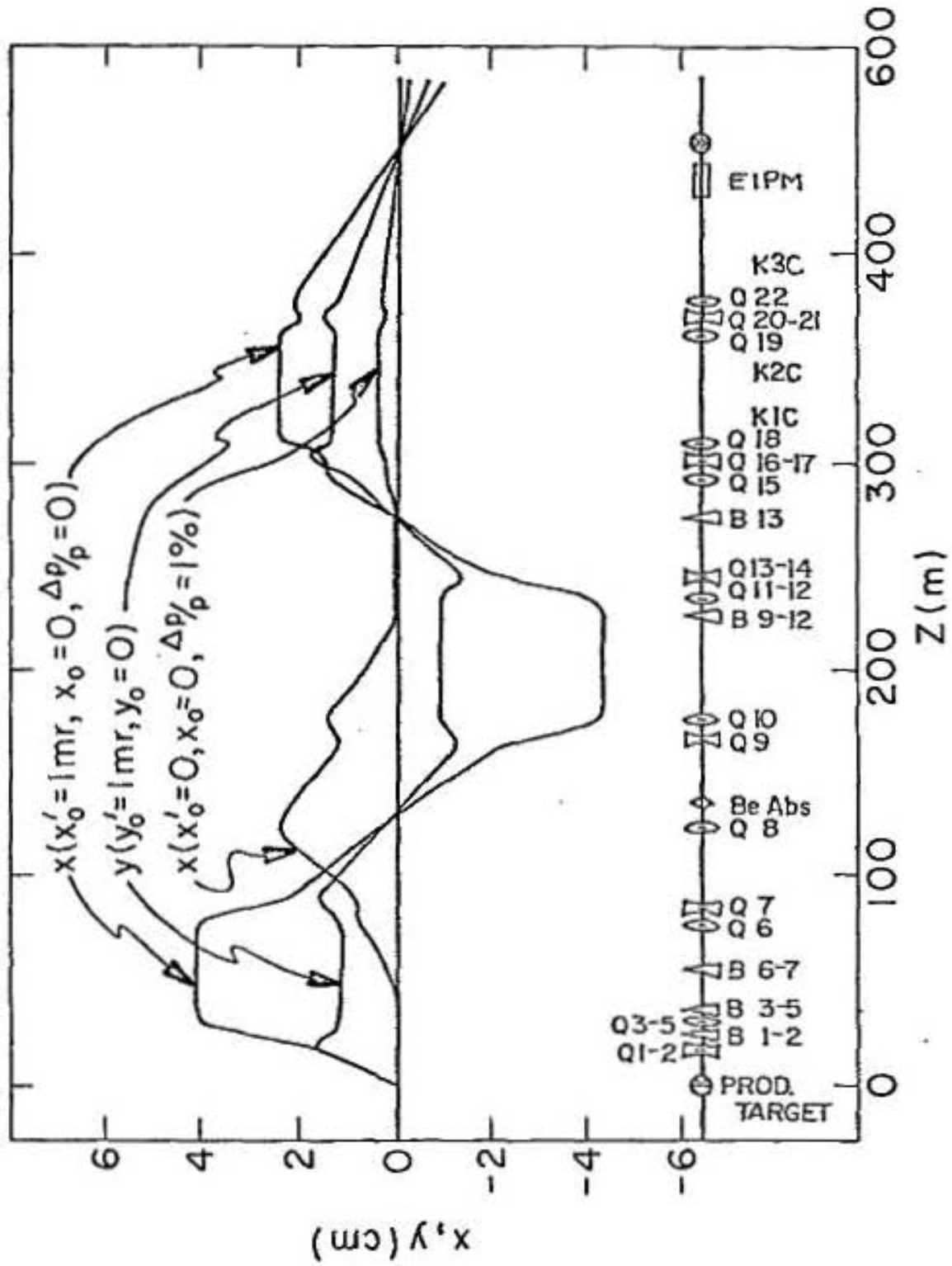

Figure 3

experimental groups dependent on the same production target. The M1 beam line elements were set to transport a positive 200 GeV/c beam. The momentum bite ($\Delta P/P$) of this beam was ~3%.

In order to maximize the kaon flux, a positively charged beam was selected since the absolute flux of K^+ is greater than K^-, and also because the K^+/π^+ ratio is larger than the K^-/π^- ratio. Further enhancement of the kaon fraction of the beam was achieved with a beryllium filter of adjustable thickness.[49] Such a scheme exploited the larger proton and pion absorption cross sections on nuclear matter. We could remotely insert a maximum of 87 inches of beryllium into the beam at the momentum dispersed focus at ~140m, where the effects of multiple Coulomb scattering on the beam were minimal. A collimator at this point defined the selected beam momentum.

Further downstream, the momentum-dispersed beam was recombined and passed through a 175 foot long parallel region which provided space for beam-species tagging by two differential Cherenkov counters (K1 and K2). A third Cherenkov counter (K3) was located further downstream. All counters were filled with helium and the pressure in K1 was adjusted so it would identify kaons. The function of the other two Cherenkov counters is immaterial to this work, and they will henceforth be ignored.

K1's helium radiator was ~100 feet long, and it had a Cherenkov angle of 7.5 mrad. At its downstream end was an aluminized spherical concave mirror, of ~100 feet focal length, which reflected the cone of Cherenkov radiation back to the upstream end of the counter, where

a ring of six phototubes was positioned. Outside of this ring was another ring of six phototubes that could be implemented for vetoing purposes. They were not used in this experiment.

Adequate isolation of the kaon signal was achieved by requiring a two-fold (K12) or three-fold (K13) coincidence of the logically OR-ed signals from the three pairs of adjacent phototubes. A pressure curve for both modes is given in Fig. 4. The counter was slightly inefficient due to the angular divergence of the beam caused by the presence of the beryllium absorber. Even with the less restrictive two-fold requirement, the pion contamination of the kaon signal was <1%. Most of our data was accumulated with the requirement of the two-fold kaon signal (K12) in the hardware trigger. Both signals, K12 and K13, were latched with every event trigger for contamination studies off-line. The raw kaon beam flux was defined as the coincidence K12·B, where B was a suitable coincidence of beam scintillation counters to be described shortly. We ran typically with kaon fluxes of 4-5 × 10^4 kaons per pulse, with the kaons comprising ∿14% of the beam. Contamination of this flux from pions and other sources will be described in Chapter V.

Two 1/16 inch thick scintillator counters, B0 and B1, were placed before and after the parallel region previously described (see Figure 5). Signals from these counters were ultimately part of the beam definition, but because of their distance (several hundred feet) from the experimental apparatus they were not immediately used to define a beam particle. Signals from two closer scintillator counters,

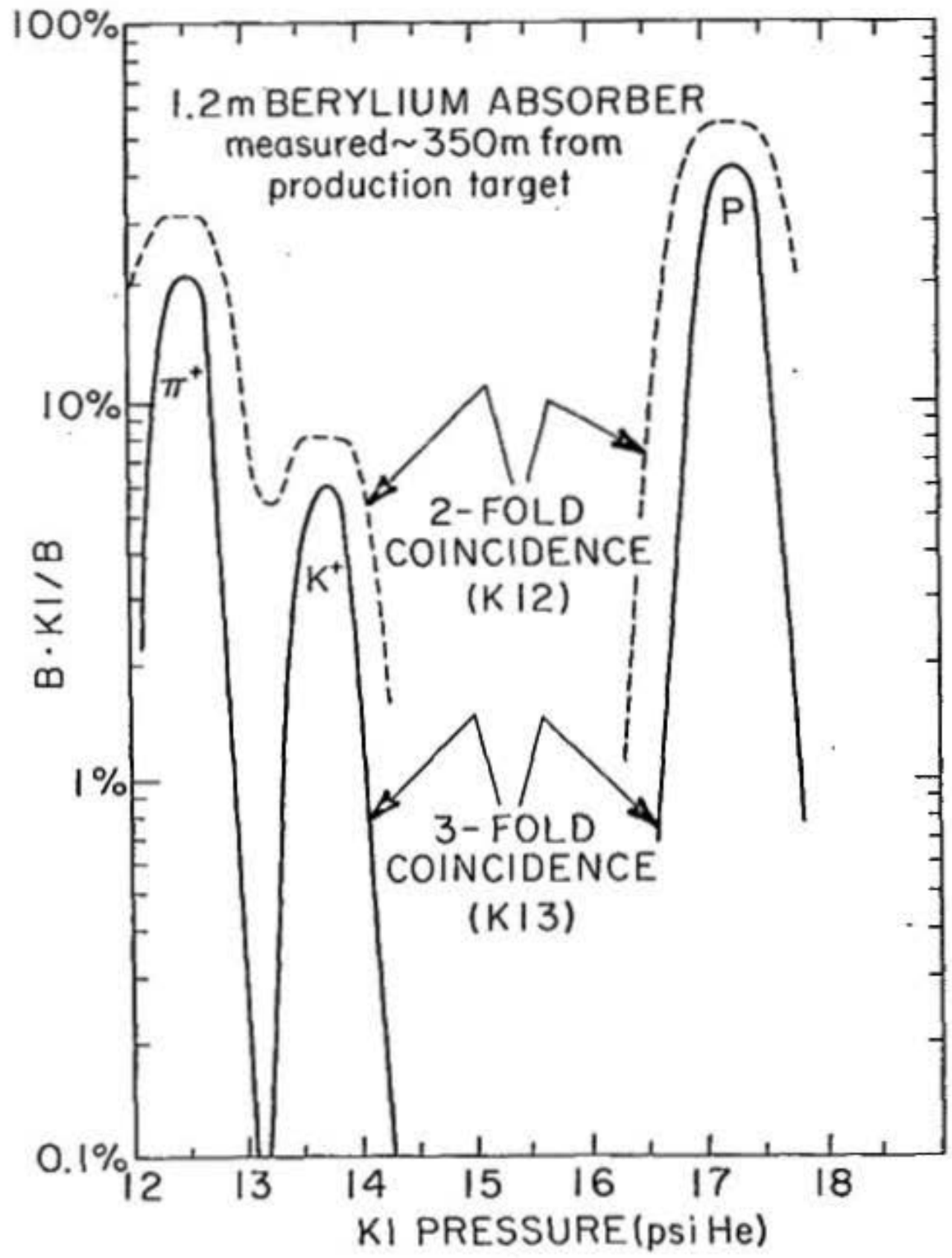

Figure 4

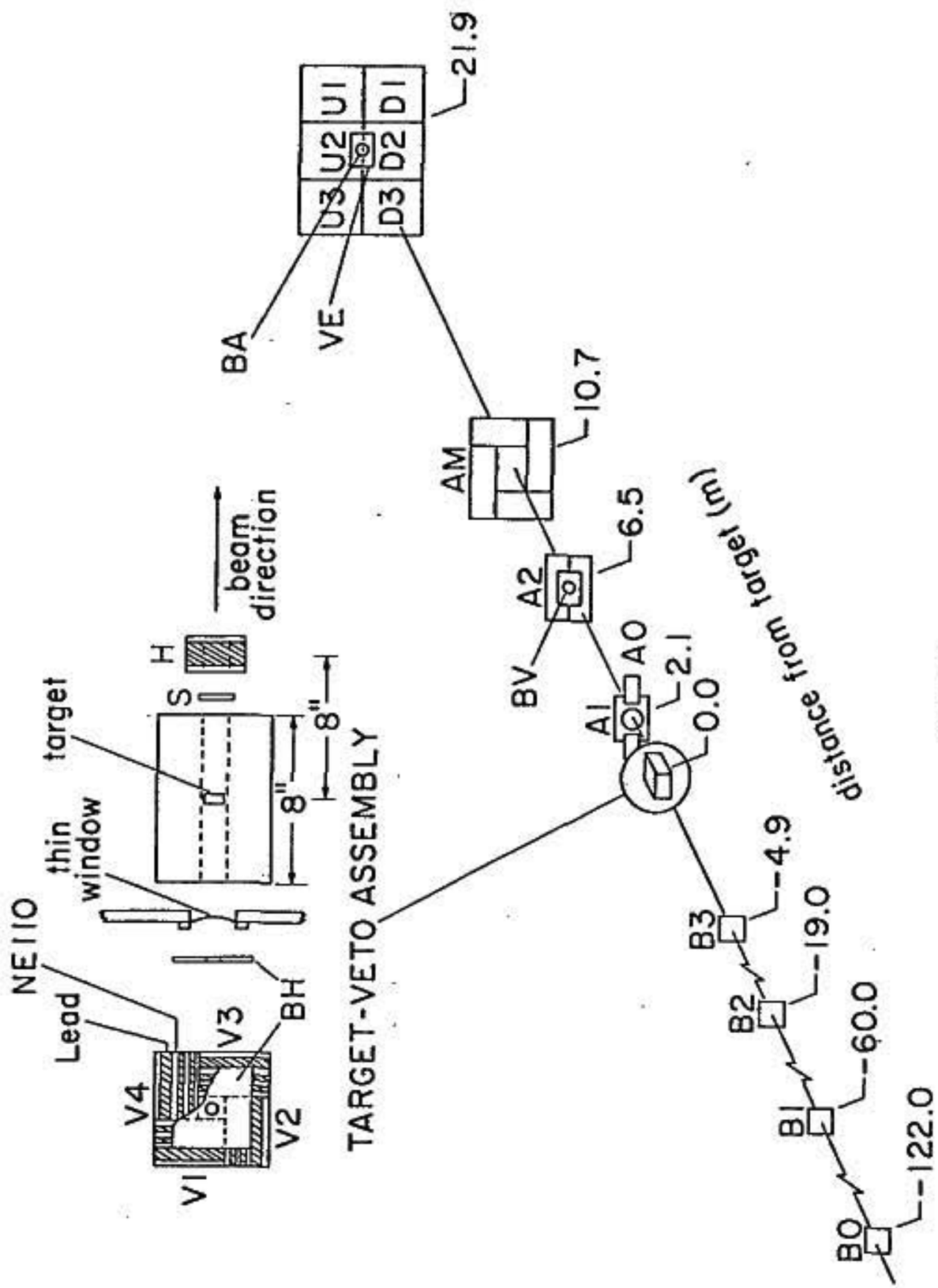

Figure 5

B2 at 62 feet upstream of the experimental target, and B3 at 16 feet upstream, were used to form the initial definition of a beam particle.

A schematic plan view of the E272 spectrometer is shown in Figure 6. The function and purpose of its various elements will be individually described below; the calibration of these elements will be discussed in Chapter IV.

B. Beam Spectrometer and Targets

A module of four small-pitch (1mm) proportional chambers (J1) was located just upstream of the beam counter B2. This module consisted of two x-planes and two y-planes, with one plane of the pair offset relative to the other by half a wire spacing to give each staggered doublet an effective wire pitch of 0.5 mm. A similar module, J2, was placed 4 feet upstream of the experimental target. These chambers used a gas mixture of 17% isobutane, 4% methylal, 0.4% freon B13, with the balance argon. Each chamber was separately plateaued using beam particles, and the voltages on the cathode planes were set between -2.9 KV and -3.1 KV.

These two modules were used to determine the incoming beam particle trajectory with an angular resolution of 0.015 mrad. Since the probability of multiple beam tracks at our intensities was at the few percent level, the number of beam tracks was restricted to one to avoid complications and ambiguities (see Chapter V). Signals from one of the x-planes, in both J1 and J2, were, in addition, used in a Matrix Beam Veto (MBV) that was part of the hardware trigger for candidate $K^{*+}(890)$ events.

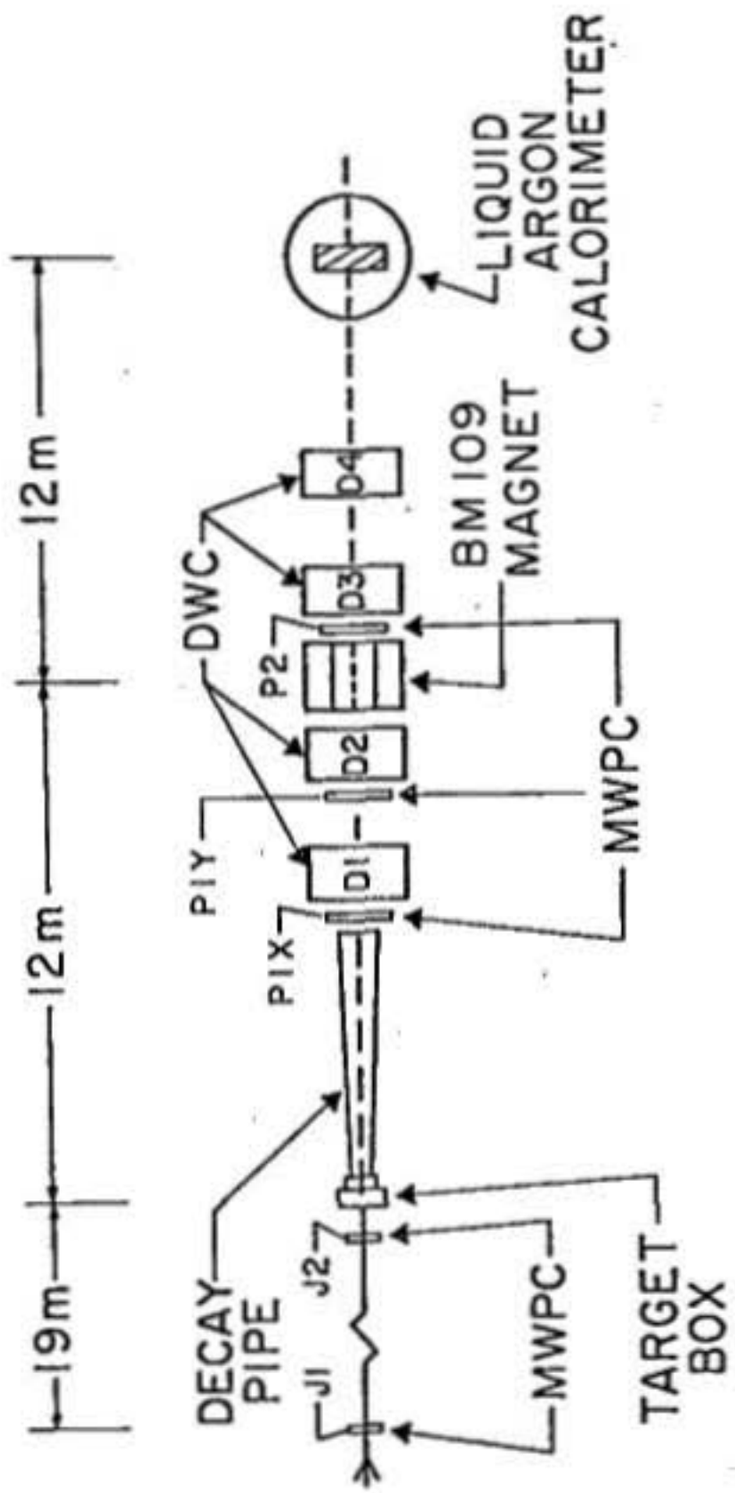

Figure 6

The targets were mounted in thin rectangular lucite holders (1.5" × 1.375" × 8") which were inserted into the target holder-veto assembly (see Figure 5). This assembly was located in an evacuated aluminum box which had a small aluminized mylar window to allow the beam to enter. The target veto assembly consisted of four lead-scintillator sandwich veto counters surrounding the target; these were used to suppress the large fraction of incoherent events and events involving nuclear excitation and/or fragmentation.

A veto scintillator counter (0.875" dia.), BH, was centered on the target and located 10 inches upstream of it outside of the target box. The incident beam was required to pass through a hole in this counter to complete the definition of an acceptable beam particle, i.e. $B \equiv B0 \cdot B1 \cdot B2 \cdot B3 \cdot \overline{BH}$.

Also located in the target box were a scintillator counter used for pulse height determination (the S-counter; 1.5" × 1.5" × 1/16"), located 6 inches downstream of the target, and a second veto counter with a hold of diameter 1.25", H, which partially defined the geometric acceptance of the spectrometer. The integrated pulse height from the S-counter was discriminated and used for triggering purposes to select the multiplicity of charged particles leaving the target. The analog signal was also digitized for off-line scrutiny.

The detailed parameters of the targets used in this experiment are presented in Table V. We used both copper (Cu) and lead (Pb) targets to ensure that we understood the scaling behavior of the

Table V

Parameters of the Experimental Targets

Element	Atomic Number	Atomic Weight	Thickness[a] (in.)	Thickness[a] (gr/cm^2)	Number of Radiation Lengths (Ref.50)	Number of Absorption Lengths[b] (Ref.51)	Density (gr/cm^3)	$A/N_o\ell$ (barns)
Copper (Cu)	29	63.54	0.251	5.666±0.006	0.441 ± 0.001	0.043 ± 0.000	8.888 ± 0.037	18.62 ± 0.02
Lead (Pb)	82	207.19	0.049	1.378±0.002	0.216 ± 0.000	0.007 ± 0.000	11.07 ± 0.23	249.7 ± 0.4

(a) area:

Cu: 1.471 in × 1.348 in.

Pb: 1.475 in × 1.348 in.

(b) for neutrons; assume protons same.

Coulombic and strong production processes with nuclear charge and nucleon number. Also available was an empty (MT) lucite target holder with which data was taken to make target-empty subtractions from target-induced cross sections.

The target thicknesses were chosen to maximize coherent $K^{*+}(890)$ production, but to simultaneously keep multiple Coulomb scattering and photon conversion in the target to a minimum; the former is an important source of transverse momentum resolution degradation.

The dimensions of the targets were measured to ± 0.001 inches and their masses were determined to better than 0.01 grams.

The integrated, gated (i.e. usable; see Section E) kaon flux, $(K12\cdot B)_{gated}$, used in determining cross-sections on each target, was:

Target	Total gated K^+ flux
MT	2.745×10^8
Cu	4.777×10^8
Pb	1.4363×10^9

C. Charged Particle Spectrometer

The design of the charged particle spectrometer was optimized for precision charged particle tracking and momentum determination.

A 250 inch long decay tank was hermetically coupled to the target box at its downstream side. This provided an evacuated volume in which beam kaon decays and neutral vee decays (such as $K_s^o \to \pi^+\pi^-$) could be detected, unencumbered by complications arising from beam interactions in this region.

Two lead-scintillator veto counters, AOL and AOR, at the decay tank's upstream neck defined a four-inch diameter entrance hole, and similar veto assemblies, A1 and A2, located farther downstream along its length, further defined this fiducial volume. The A2 counter had an opening to match the 8 in. × 24 in. aperture of the momentum analyzing magnet (BM109). Surrounding the magnet aperture, and lining the downstream half of the aperture sides, were six lead-scintillator veto counters known collectively as AM. The AM counters around the magnet aperture also set the final limits on the geometric acceptance of the spectrometer, while those inside the magnet vetoed low-momentum charged particles that curled up inside the magnet, and that would otherwise not have been detected.

At the very end of the charged particle spectrometer, but in front of the LAC, were the counters BA, VE, and six counters U1-U3, D1-D3. BA was a small 1.25 inch diameter counter centered on the deflected beam, used to veto non-interacting beam particles. VE and the U and D counters were used in conjunction with logic signals from the LAC to veto elastic scattering background (see Section E).

In summary, the charged veto logic, strobed by the beam signal B2·B3, can be written as:

$$\text{CHARGE VETO} \equiv B2\cdot B3\cdot\overline{BH}\cdot\overline{BA}\cdot\overline{\Sigma V_i}\cdot\overline{(AOL + AOR + H)}\cdot\overline{A1}\cdot\overline{A2}\cdot\overline{AM}$$

(see Figure 7).

The tracking elements of the spectrometer consisted of multi-wire proportional chambers (MWPC's) and drift wire chambers (DWC's). The MWPC's were used both for triggering purposes, and as an aid in the

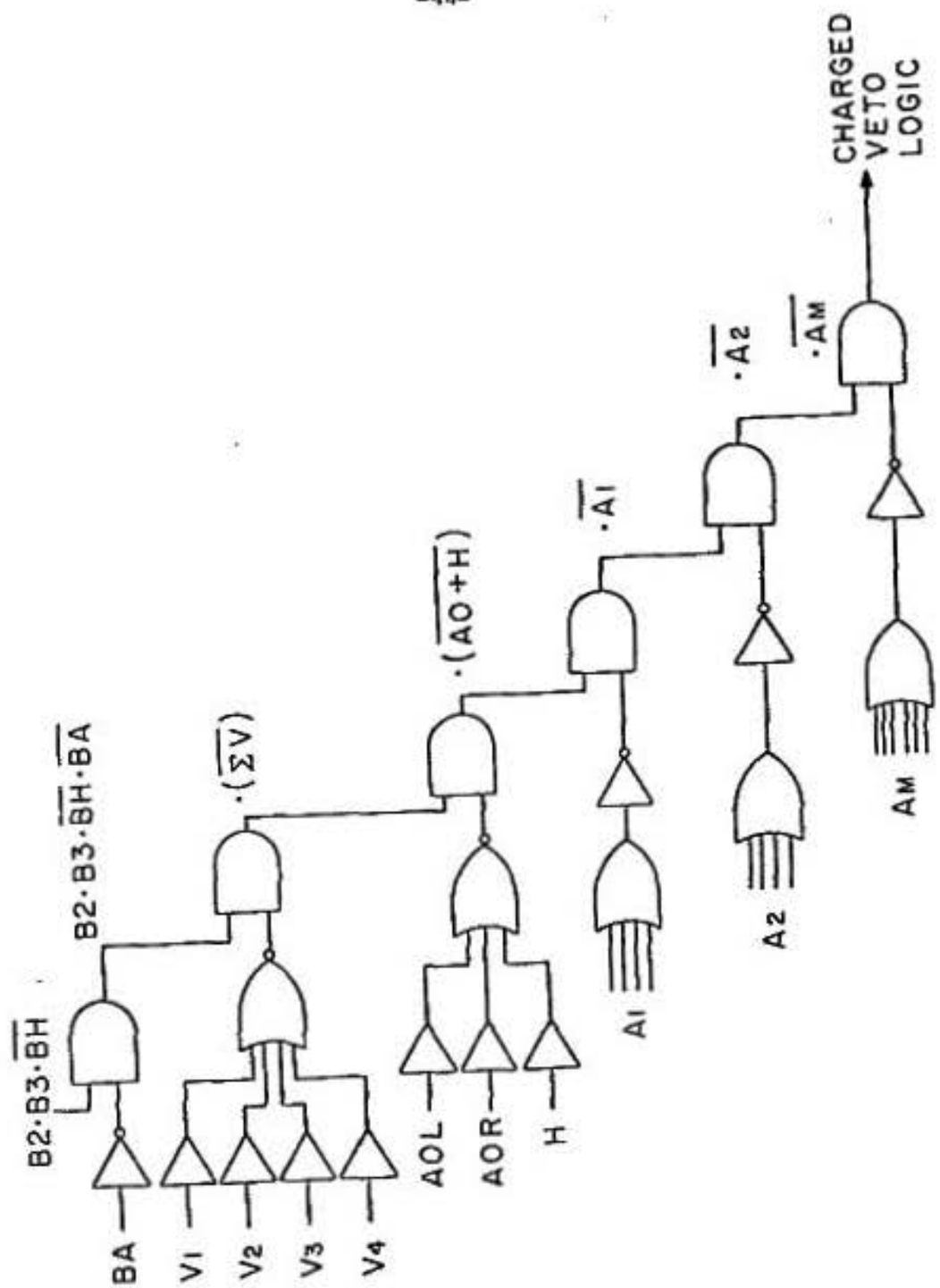

Figure 7

off-line reconstruction events. The DWC's were completely passive during data acquisition. Their high-precision tracking capability provided high-resolution information for charged-particle trajectories.

The spectrometer utilized six planes of 0.1 inch pitch MWPC's with a total of 1344 sense wires. The planes were arranged in doublets, each one offset from its partner by half a wire spacing. There were two x-doublets, P1X and P2, and one y-doublet, P1Y. P1X and P1Y were located upstream of the magnet, and had 8 in. × 24 in. active areas to match the magnet aperture. P2 had an 18 in. × 35.2 in. active area, and was mounted flush to the downstream face of the BM109 magnet. These chambers used a 24% isobutane, 4% methylal, 0.1% freon B13, and remainder argon gas mixture,[52] and were operated with -2.9 kV on their cathode planes. The P1X and P1Y doublets were contained in gas-tight boxes, with each member of the pair electrically isolated from the other by a ground plane. The two P2 chambers were constructed in stand-alone fashion. Both boxes and free-standing chambers has aluminized mylar windows for shielding purposes.

Means were provided for capacitively coupling a negative 1 volt, 10 ns wide, 1 ns rise-time pulse to the high voltage cables supplying these chambers. The pulse was terminated through 50Ω to the ground of the pulsing cable. This pulse, transmitted through the chamber cathode planes, was then capacitively coupled to the anode plane, and caused all chamber anode wires to trigger their amplifier channels. This pulse was computer initiated, and a fast trigger pulse, used to latch the chamber amplifier signals, was simultaneously generated.

This electronics testing scheme was invaluable in debugging MWPC amplifier electronics and the associated latching circuitry. A diagram of this scheme is shown in Figure 8.

Each MWPC amplifier card (8 channels per card) fed a driver board which could produce three different sets of output. One set, an ECL differential pair, went through 150 foot long delay cables to the input of latch cards. The presence of a suitable signal (in our case $B2 \cdot B3 \cdot \overline{BH} \cdot \overline{BA}$) in coincidence with the chamber signal on the latch card would cause a binary switch to be set. Upon receipt of a final trigger, this information was strobed into a buffer memory to be read by the on-line computer (PDP-15), and then written onto magnetic tape along with other digitized information.

Another set of outputs was utilized only on the P1X doublet. These signals were used in concert with a similar set of signals from J1 and J2 to form a Matrix Beam Veto, as already mentioned. In order to eliminate as a possible source of background those beam particles interacting in the spectrometer itself (~0.03 proton absorption lengths), and those from non-interacting beam halo missing the BA veto counter, signals from the wires hit in J1 and J2 were used to project the beam particle's trajectory to the P1X doublet. Only the 1.2 inch wide central region of this doublet was implemented for use in this veto. If a wire in this region of the doublet signaled the passage of a charged particle through the region, as projected by J1 and J2, an MBV logic pulse was formed. However, in order not to veto events which may have scattered at large angles only in the y-direction.

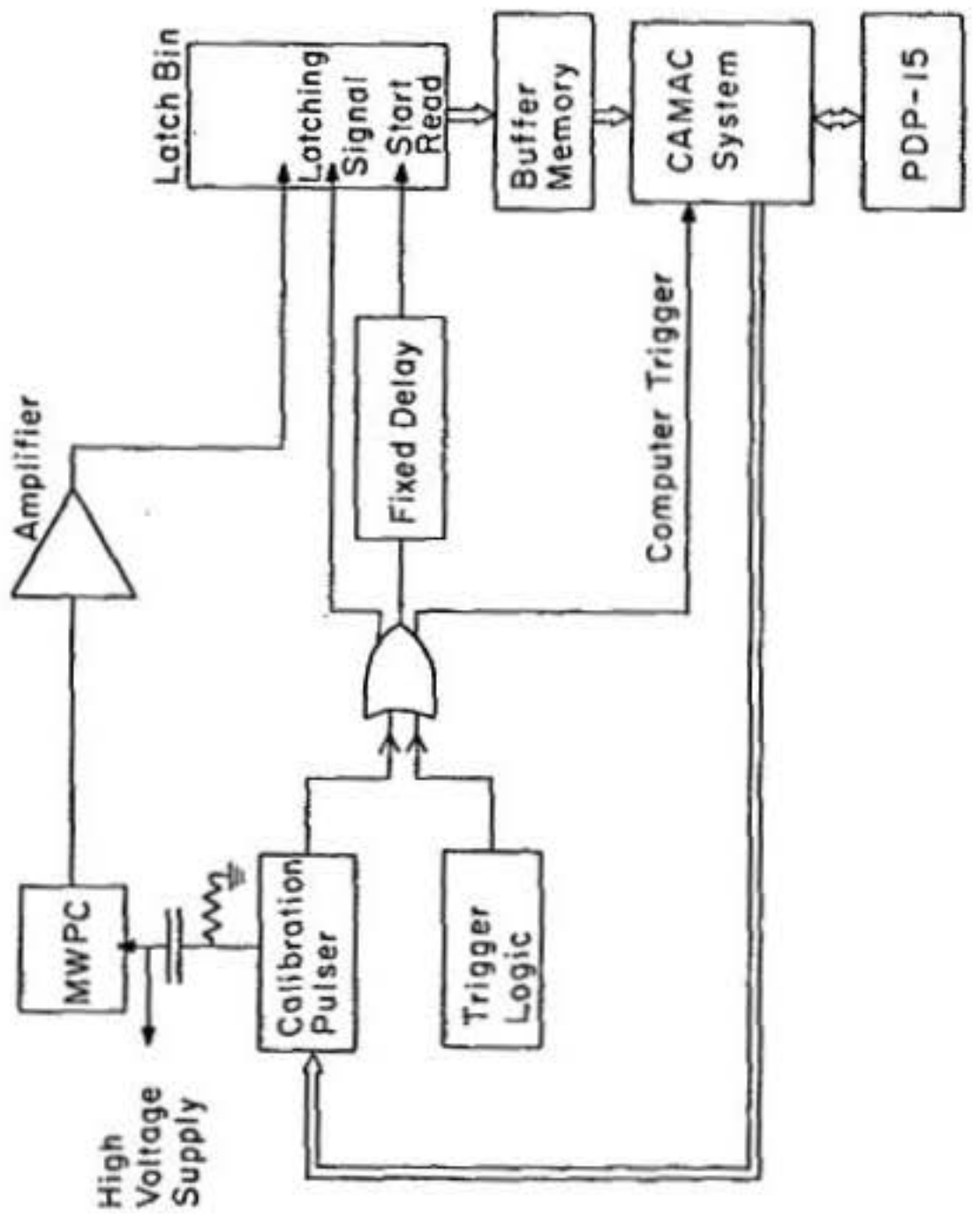

Figure 8

This veto was not used unless a scintillator counter, BV, (1.0 in. dia. × 1/16" thick) directly behind P1X and centered on it, also signaled the traversal of a charged particle. This signal was defined as $MBV^2 = MBV \cdot BV$.

An additional set of outputs utilized signals from all the MWPC wires in every chamber for a fast multilevel preprocessor built by Fermilab, that was used to count the number of contiguous "hits" or wire firings in a plane.[53] The P1X and P1Y doublets were used in such a way that their two sets of wires were interleaved into one grid; however, each plane of P2 was used separately in this counting process because the charged tracks were often at large angles downstream of the BM109 magnet and could not be expected to fire the alternating neighboring wires in the P2 doublet. This counting scheme was referred to as track counting, and the units themselves as track counters (TC). Each unit allowed separate output signals for 1,2,3,4 or ≥ 5 contiguous bunches of "hits" per plane. These units were strobed by the coincident signal $B2 \cdot B3 \cdot \overline{BH}$ to determine their status.

The twenty-four planes of DWC's were separated into four modules, DI-DIV. The sense wires were spaced at 0.8 inches for a maximum drift space of 0.4 inches. There were a total of 1032 sense wires. The modules DI and DII upstream of the magnet were self-contained, gas tight, boxes with separate gas supplies. The chambers in the modules downstream of the magnet were configured in stand-alone mode with the pairs of chambers forming a doublet sharing a common gas supply. We used a 50% ethane, 50% argon gas mixture in these chambers. Each chamber was individually supplied with its two high voltages, HVS,

the voltage on the field shaping wire directly opposite the sense wire, and, HVD, the voltage on the field wires at the edge of the drift space or cell. The wire geometries for the upstream and downstream chambers are shown in Fig. 9, as are some typical plateau curves. All DWC's were operated with HVS=-1.8 KV and HVD=-2.8 KV, giving a field gradient of about 1.0 KV/cm across the drift space. This was nominally above the drift velocity saturation point for this gas mixture.[54]

Each module consisted of three pairs or doublets arranged in staggered fashion to aid in removing left-right ambiguities, i.e., which side of the sense wire the charged particle passed. In DI, there were x, y and u (wires oriented at +30° to the vertical) doublets of 8 in. × 24 in. active area. The DII module was of a similar arrangement with the u-doublet replaced by a v-doublet (wires at -30° to the vertical). The downstream DWC's had larger active areas (DIII: 18 in. × 44.8 in., DIV: 24 in. × 57.6 in.) and the modules consisted of an x-doublet, a u-doublet with wires at +18.5° to the vertical, and a v-doublet with wires at -18.5° to the vertical. Further details on construction can be found in Reference 55.

In reconstructing charged particle trajectories, information from the upstream DWC's was used in conjunction with data from the beam defining chambers to determine the scattering angle of emerging particles. Information from the downstream DWC's gave the bending angle through the magnet, and hence the particle's momentum. These data allowed determination of the transverse momentum for each charged

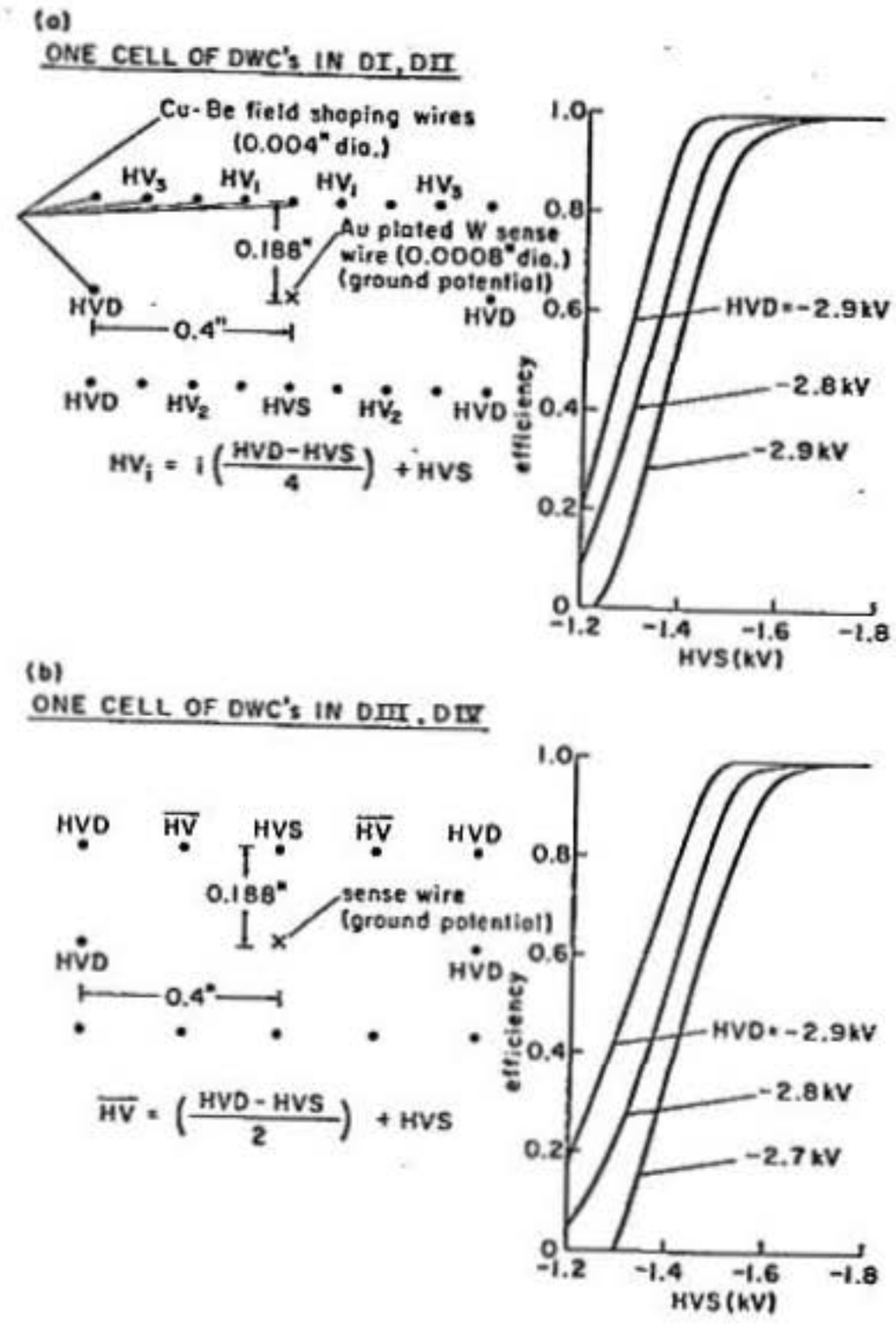

Figure 9

particle, needed for determining $-t' = (\Sigma \vec{P}_{t_i})^2$ for the parent particle. Here the summation index i runs over all detected decay particles.

Signals from the DWC sense wires were discriminated, amplified, and shaped to ECL differential pair output signals by amplifier cards mounted on the chambers. Each amplifier card had eight channels with a common discriminator threshold. The cards on modules DI-DII and DIII-DIV had separately adjustable thresholds, which were set to ~3 mV on the cards. After traveling through a 150 foot-long flat cable, the ECL level outputs were digitized using LeCroy 2770A 96- channel Drift Chamber Digitizers. The leading edge of a differential pair input started the time digitizer counting process, which was terminated by the leading edge of a stop signal. This stop signal was common to all channels of the time digitizer, and was supplied by the final event trigger which also gated off the experiment via the data acquisition computer, and initiated the transfer of digital information for that event to the computer through the experiment-computer CAMAC interface. This digital information was then written to magnetic tape for permanent storage.

Since these time digitizing units would reset with each start input, it was necessary to define a $\pm$ 200 ns window around each useable incoming beam particle in which no other beam particle was allowed to appear. This restriction will be discussed in more detail in Section E.

A short length of twisted wire, terminated through 50 Ω to the

ground of the amplifier, was taped across the input pads of each amplifier card. A pulse identical to that used to pulse the MWPC high voltage line was sent through this wire for the purpose of calibrating the time digitizers. The scheme employed a technique similar to that for pulsing the MWPC's. However, in this case the time delay between pulsing the DWC's amplifier cards, and sending a stop pulse to the time digitizers was cycled through four standard values set by a programmable delay unit under computer control. The differences between these delays were well known, and were used to calibrate each channel of the time digitizers by calculating a gain (slope) and offset (intercept) from the relationship between actual elapsed time and the number of counts the time digitizer recorded. A diagram of this scheme is shown in Figure 10. The analysis of this calibration data will be presented in Chapter IV.

As previously mentioned, the momenta of charged particles was measured with the aid of a BM109 dipole magnet of aperture 8 in. (vertical) and 24 in. (horizontal). A current of 2900 amperes supplied the magnet with a resulting integrated field length of $\int \vec{B}\cdot d\vec{\ell} = 36.07$ kG-m, yielding a transverse impulse of 1.082 GeV/c. The method of calibration of the BM109 is found in Chapter IV.

To minimize background interactions in the spectrometer itself, any open areas free of experimental elements were filled with helium filled bags. These included the spaces between DI and DII, between DIII and DIV, between DIV and the LAC, and inside the magnet.

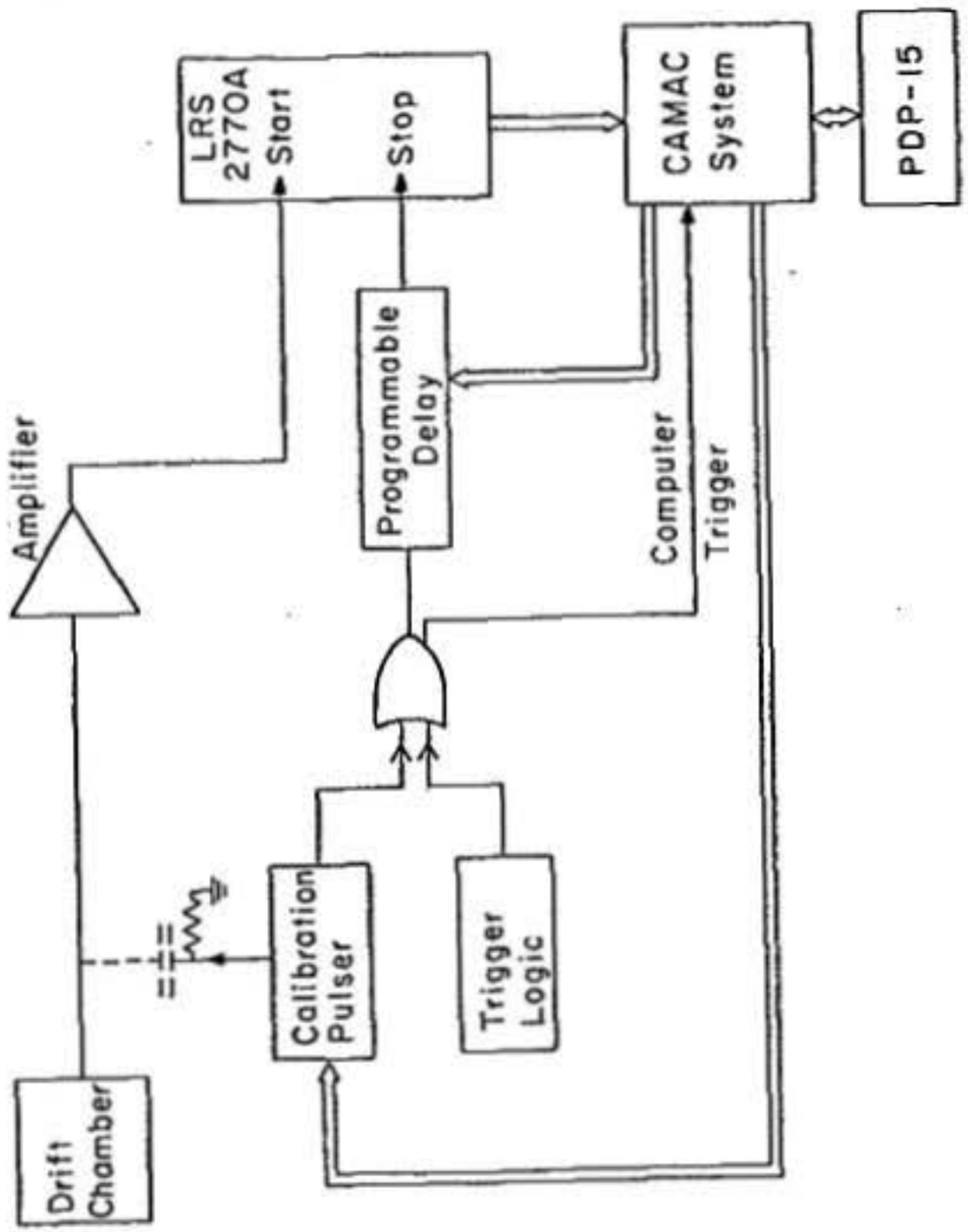

Figure 10

D. Liquid Argon Calorimeter

A liquid argon calorimeter (LAC) of 32 in. × 56 in. active area was used to measure, with high precision, the positions and energies of high energy photons in the final state. It had a layered construction, two layers of which are shown in Fig. 11. Each layer consisted of 0.063 in. of copper-clad G-10 printed circuit board, and a 0.080 in. lead plate held 0.080 in. apart by G-10 spacers around the edges, and by small G-10 button spacers in the active area. All voids were filled with liquid argon.

Each copper-clad G-10 board was alternately etched with vertical or horizontal 0.5 in. wide strips; these strips collected the charge from the ionization of the argon atoms produced by the cascading electromagnetic shower, initiated by the incident high energy photon. The vertical strips (x-strips) extended the full length of the boards while the horizontal strips (y-strips) were bisected by a thin etched gap into left and right halves.

The detector was comprised of 61 such cells for a total of 25 radiation lengths of material. This amounted to 1.6 proton interaction lengths. All of the x-strips at a common x coordinate in the front and back halves of the detector were electrically connected, as were all y-strips at a common y-coordinate; the independence of the left and right y-strips was maintained, however. Each of these ganged groups of strips were held at ground potential, and fed to a charge sensitive amplifier. The lead plates were maintained at a voltage of -3.0 KV. Further details on construction of the LAC can be found in Reference 56.

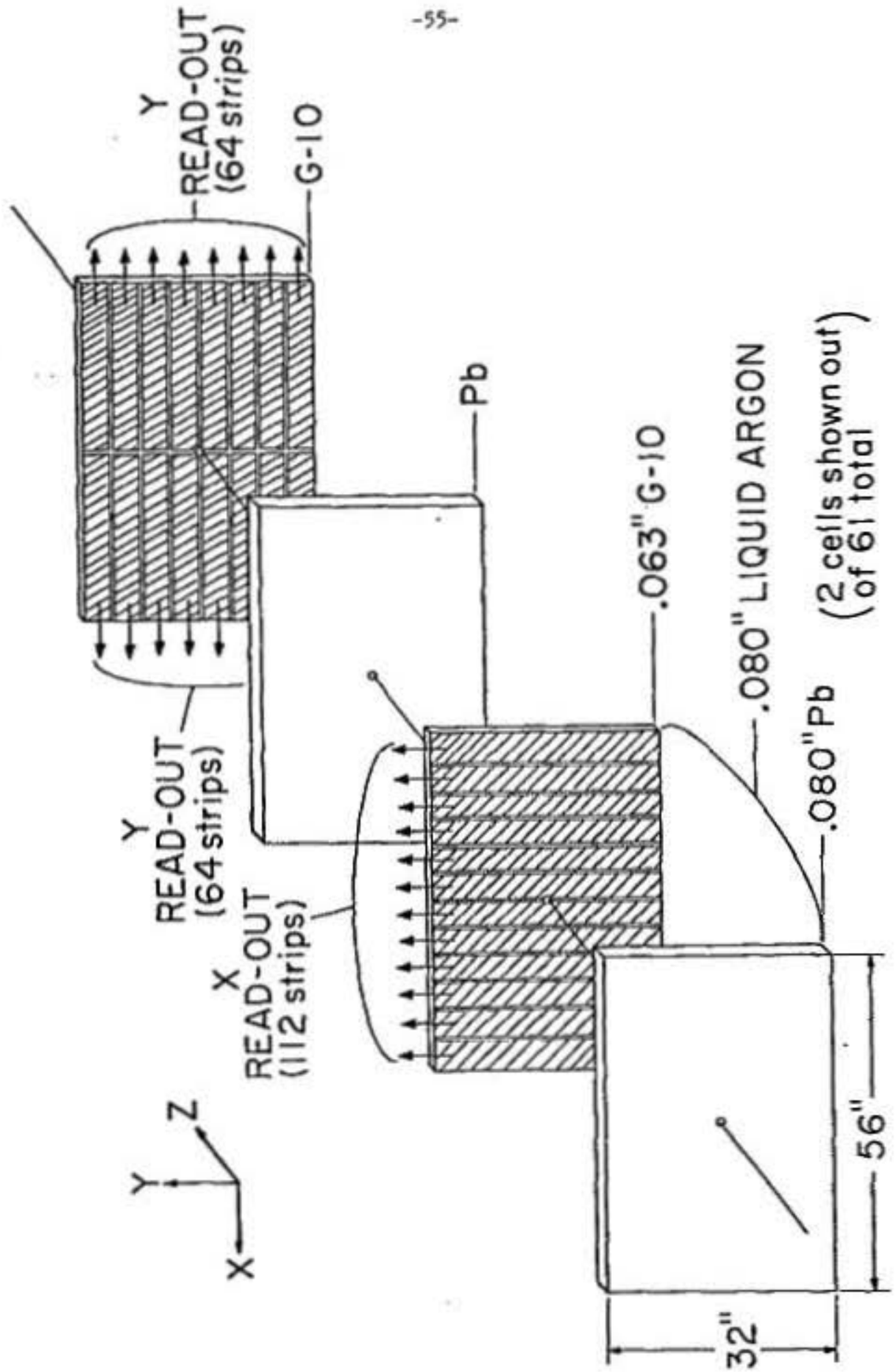

Figure 11

The output from each charge sensitive amplifier channel provided the pulse height (proportional to the charge collected on the copper strips) as well as a fast analog signal for triggering purposes. These analog signals, also proportional to the collected charge (i.e. to the energy deposited by the high energy photon) could be individually weighted, summed, and discriminated to form an overall trigger decision for the calorimeter. Reference 57 provides a detailed description of the amplifier electronics, the pulse height digitizing electronics, and the system for making this digital information accessible to the on-line computer.

The sensitive portion of the detector was immersed in liquid argon contained in a stainless steel cryostat cooled by liquid nitrogen. There was ∿1 radiation length of material in front of the active volume of the detector. This consisted of the walls of the cryostat, the vacuum jacket walls, and ∿20 inches of microspheres (evacuated glass spheres of 50-150 μm diameter and density ∿0.079 gr/cm^3) used to fill the void between the detector itself and the wall of the cryostat. There was a 0.75 in. hole through the middle of the detector for the beam to pass through. This was filled with an evacuated quartz tube to minimize beam interactions in the detector.

The detector read-out was initiated by receipt of a final trigger pulse. Each channel was interrogated by a scanning module to see if its digitized pulse height signal was above a pre-selected threshold (∿100 MeV). If it was, the level and strip address were

strobed into a buffer memory to be accessed by the on-line computer.

Similar to the MWPC's and DWC's, a pulsing system was implemented to inject a known amount of charge into the input of each amplifier for calibration purposes. This allowed the gain of each amplifier to be monitored throughout the running period. This scheme could also be employed in a mode where no charge was injected, and the read-out threshold was set to zero; in this case, the digitized signal from the amplifier was merely the pedestal of its internal pulse height digitizer. Thus, drifts in pedestals could also be monitored. In practice, these two modes were alternated with each calibration trigger (see Section E). An absolute calibration of the LAC was obtained using 50 GeV/c electrons in the beam. This will be discussed in Chapter IV.

For triggering purposes, the fast analog signals from the amplifiers for the upper half of the front y-strips were summed together to form the signal E_{up}. The amplitude of this signal was proportional to the energy deposited by a photon in the front upper half of the detector (~13 radiation lengths). The hadron induced background in this signal was expected to be very small. A similar sum was performed with the lower y-strips to form the signal E_{down}. A noise subtraction from these signals was achieved by taking the signal from edge strips of the detector outside of the spectrometer acceptance, matching it in strength to the noise on the E_{up} and E_{down} signals, inverting it, and adding it, through a passive fan-in, to the E_{up} and E_{down} signals. A total energy signal E_{tot}, proportional to the total energy deposited

in the detector, was derived from the sum $E_{tot} = E_{up} + E_{down}$. The analog circuitry from which these signals are derived is diagrammed in Figure 12, as is the means of specifying thresholds for the E_{up}, E_{down}, and E_{tot} signals by inputting these signals to pulse height discrimination units and selecting the appropriate discrimination level.

E. Experimental Triggers and Data Acquisition

Even though our experiment supported eight different, operationally concurrent triggers, only those germain to the $K^{*+}(890)$ study will be explored. These include data triggers for selection of $K^{*+}(890)$ events, beam triggers for monitoring beam flux, and a calibration trigger which initiated pulsing of the MWPC, DWC, and LAC systems, as previously mentioned.

The $K^{*+}(890)$ event triggers were designed to isolate the $K^{*+}(890) \rightarrow K^+\pi^0 \rightarrow K^+\gamma\gamma$, and the $K^{*+}(890) \rightarrow K^0_s\pi^+ \rightarrow \pi^+\pi^-\pi^+$ final state. Concurrently with these events, beam kaon decays in the decay tank, of the sort $K^+ \rightarrow \pi^+\pi^0 \rightarrow \pi^+\gamma\gamma$ and $K^+ \rightarrow \pi^+\pi^+\pi^-$, were recorded for normalization purposes. This will be discussed in Chapter V.

The first aforementioned decay mode was isolated by the "p-trigger", where the name is derived from its use in detecting coherently excited ρ mesons with their subsequent decay to $\pi^+\pi^0$. This pion-induced data was accumulated concurrently with the $K^{*+}(890)$

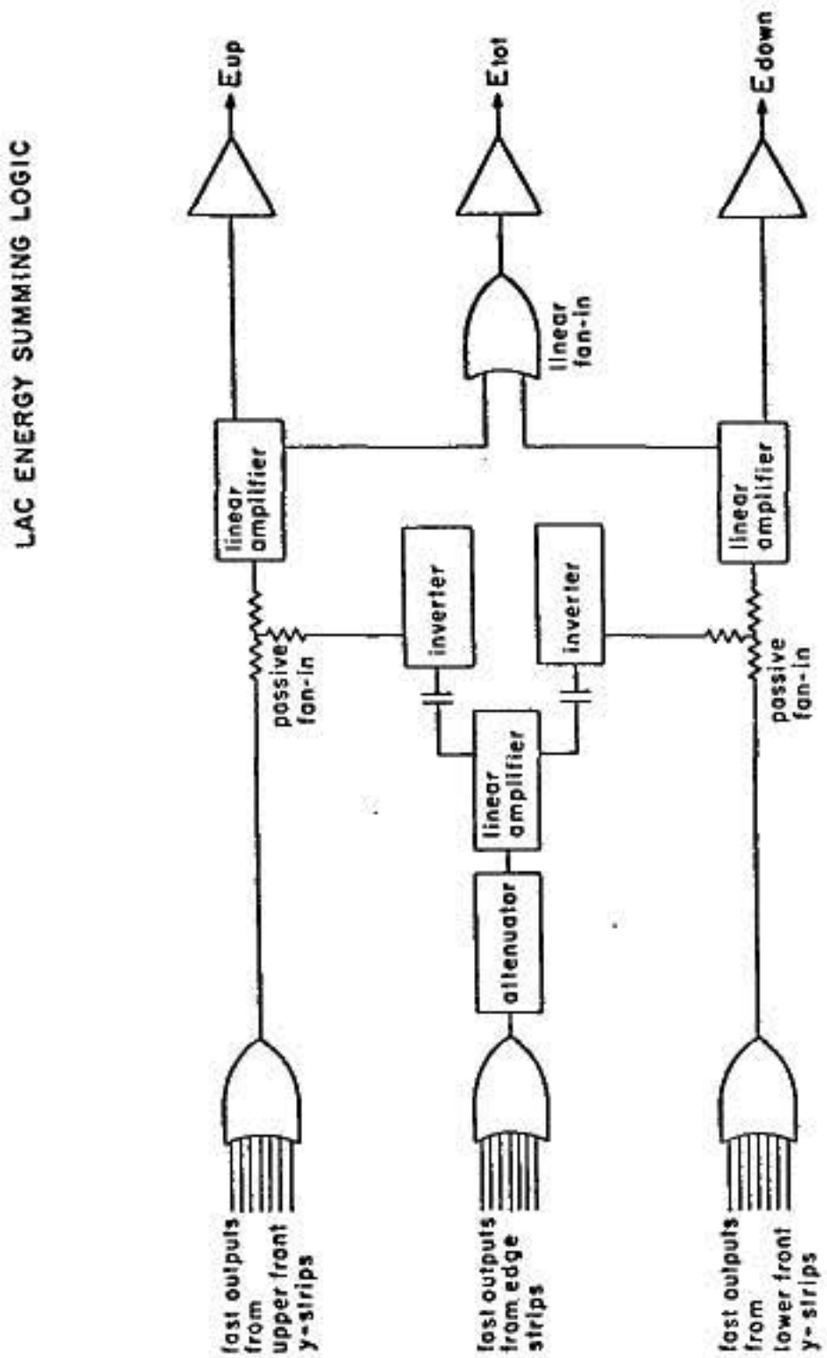

Figure 12

data. The second final state was isolated by the "V-trigger," where the name arises from the fact that it was set to detect final states with neutral particles emerging from the target, and decaying into a charged particle pair in the decay tank.

Specifically, the ρ-trigger was set-up to detect one charged particle in the charged particle spectrometer and at least one photon in the LAC. The V-trigger was tuned to isolate three charged particles in the spectrometer, but with only one leaving the target. The V-trigger made no use whatsoever of calorimetric information from the LAC, whereas the ρ-trigger demanded a minimum of energy deposited in the LAC, and other requirements utilizing the LAC, the VE counter, and the U and D counters. These details will be described shortly.

As mentioned earlier, an acceptable incident beam particle was defined by the logical product $B \equiv B0 \cdot B1 \cdot B2 \cdot B3 \cdot \overline{BH}$. All of the timing of logic signals was relative to the leading edge of the signal from B3, the beam counter nearest the target. After suitable delay, the B2·B3 signal was used to form a ± 200 nsec dead-time window bracketing itself. This was the first stage of all real data triggers, and forced all acceptable beam particles to be isolated in time from any other by ± 200 nsec. This was necessitated by the single hit capacity of the DWC time-to-digital converters (LRS 2770A). Because the maximum drift time of electrons in the DWC's was 200 nsec, a charged track associated with an event induced by another beam particle within this ± 200 nsec window would have had its hits registered in the time digitizers if its ionized electrons were the last to drift to

the DWC's sense wire. Therefore, this window eliminated any ambiguity or confusion that might otherwise have occurred in reconstructing charged tracks. This gating introduced a contribution to the overall experimental dead-time of ∿10% at the intensities at which we typically took data (3-6 × 10^5 particles/spill).

For the ρ-trigger, only a lower limit of 30 mV (corresponding to the lowest threshold available in the relevant discriminator unit (LRS 621BL) was applied to the S-counter pulse height ($S_\rho \geq S0$). To isolate single charged-particle production for the V-trigger from the more copious three charged particle production rate, an upper cut-off S1 was imposed on the S-counter pulse height. The lower limit on S was the same as for the ρ-trigger, and the S-counter requirement for the V-trigger can either be written as $S0 < S_V \leq S1$ or $S_V = S0 \cdot \overline{S1}$. Corrections to production rates necessitated by these S-counter thresholds will be discussed in Chapter V. The S-counter pulse height for each event was digitized, and became a part of the event-data record written to magnetic tape. This information facilitated off-line analysis of the requisite corrections for these pulse-height windows imposed on the S-counter signal.

The MBV[2] logic described in Section C was utilized as a veto in both the ρ and V triggers for reasons previously elucidated. Any charged particle in the final state within a 0.3 mrad scattering angle of the incident beam particle trajectory, as determined by the J1 and J2 chambers, and passing through the BV counter, would, assuming perfect efficiency, activate this veto. In practice, its efficiency

was limited to ∿92% by chamber inefficiency (efficiency ∿0.98), and the matrix electronics efficiency (∿0.98). The status of the MBV and BV counter signals (on or off) were separately latched in a coincidence register by the associated event trigger, and subsequently written to magnetic tape for off-line study.

The track counter logic used in the ρ and V-triggers is shown in Figure 13. The trigger requirements of these signals were relatively loose to allow the possibility of δ-rays being produced in the chambers, and to take account of noise in the MWPC's.

The ρ-trigger required only a three-of-four coincidence of any of the four TC's registering one or two clusters. The V-trigger required two, three, or four clusters in either P2 chambers, with a veto if both recorded two, and it also demanded ≤ 4 tracks in the P1X or P1Y doublet, again, with a veto if both doublets registered one or four tracks. This logic can be written as:

$$TC\rho = \sum_{j=1}^{4} \prod_{i=1}^{3} (P_i = 1 \text{ or } 2)$$

where i labels the four different track counters (P1X, P1Y, P2X1, and P2X2), and j labels the possible combinations of three of them.

$$TC_V = (P1X=1,2,3,\text{or } 4)\cdot(P1Y=1,2,3,\text{or } 4)\cdot\overline{(P1X=1\cdot P1Y=1)}\cdot\overline{(P1X=4\cdot P1Y=4)}$$

$$\cdot(P2X1=2,3,\text{ or } 4)\cdot(P2X2=2,3,\text{ or } 4)\cdot\overline{(P2X1=2\cdot P2X2=2)}$$

In order to suppress the background in the ρ-trigger due to elastic scattering of the incident beam hadron with energy deposition

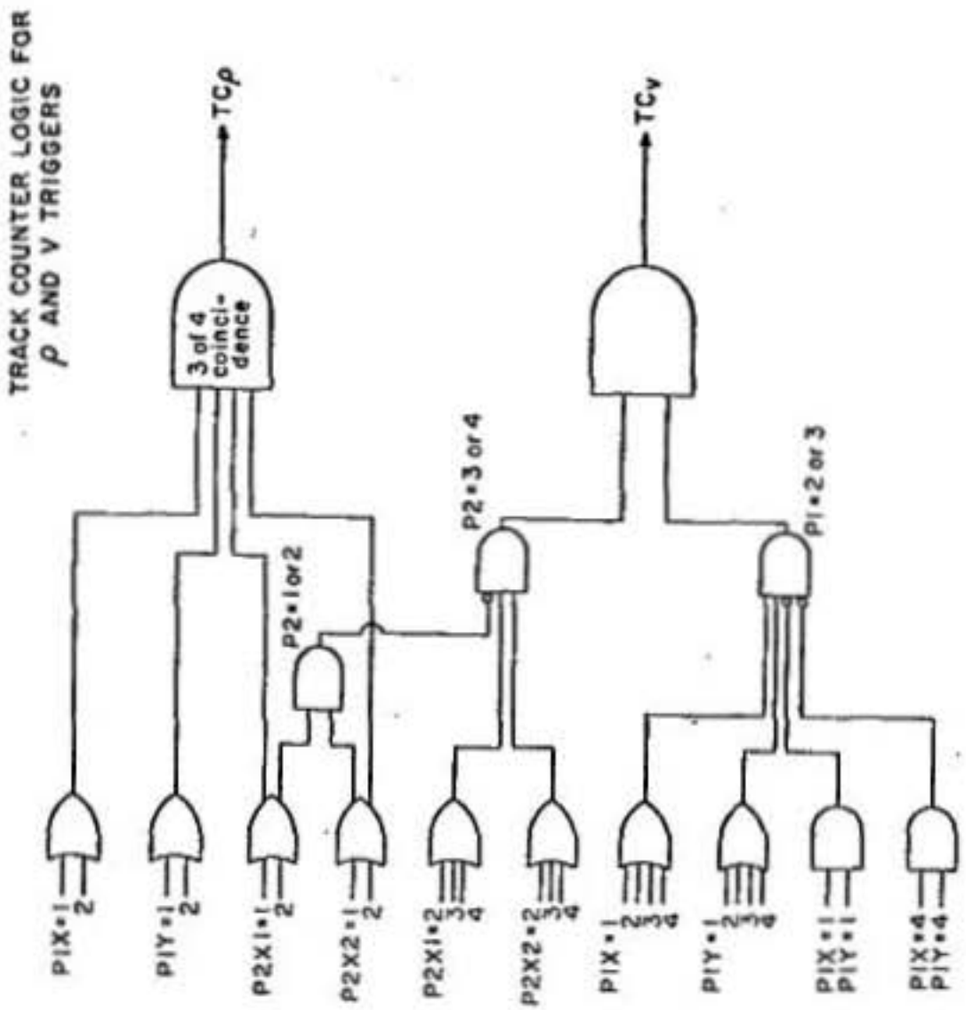

Figure 13

in the LAC greater than the E_{tot} threshold, two approaches were used. The first method exploited momentum conservation in $K^{*+}(890)$ decays, and the forward production of coherent events. In an average sense, the charged and neutral energy from decays such as $K^{*+}(890) \rightarrow K^{+}\pi^{o}$ would tend to fall on either side of a horizontal plane bisecting the LAC. For this reason, a wall of six scintillator counters (U1,2,3 and D1,2,3; each 18 in.×16 in.×1/8 in.) was mounted in front of the active area of the LAC; the U counters above the center-line, and the D counters below. The E_{up} and E_{down} signals, described earlier in Section D, were used in association with signals from these counters to ensure that the K^{+} and the photons did indeed fall on opposite sides of this median plane. Energy above threshold deposited in the upper half of the LAC was required to have no same-half accompanying charged particle; the same was true for the lower half of the LAC. Also, events with more than one U or D counter registering passage of a charged particle were vetoed.

The above technique was supplemented by a veto signal from the VE counter when a charged particle passed through it. This counter covered the region of up/down ambiguity near the center-line of the LAC, and was positioned to intercept the majority of small angle elastic scatterers with only a small loss of $K^{*+}(890)$ events. This counter was 7 in. × 1.625 in. in area with its small side aligned with the edge of the BA scintillator counter.

The final LAC calorimetric requirement in the ρ-trigger was for the energy deposited in the detector to be above the total energy threshold set by the discrimination level on E_{tot}. The total ρ-trigger LAC logic requirements are detailed in Figure 14.

One last remark concerns the relatively slow response of the LAC electronics in digitizing the strip pulse heights (see Reference 58 for details). In order to minimize dead-time caused by this relatively slow process, the fast charged particle logic for the ρ and V triggers was formed first into pre-triggers. If these pre-triggers were satisfied, a signal was sent to the LAC to initiate pulse height digitizing and read-out. These pre-triggers were:

$$\text{PRE } \rho \equiv \text{CHARGED VETO LOGIC} \cdot \text{SO} \cdot \text{TC}_{\rho} \cdot \overline{(\text{MBV}^2 + \text{VE})}$$

$$\text{PRE V} \equiv \text{CHARGED VETO LOGIC} \cdot \text{SO} \cdot \overline{\text{S1}} \cdot \text{TC}_{V} \cdot \overline{\text{MBV}^2}$$

In the case of the ρ-trigger, if the further requirements imposed by the LAC γ-logic were not met, a fast abort signal was sent to the LAC read-out system to clear it and ready it for the next trigger. If the LAC γ-logic was satisfied for the ρ-trigger (and always for the V-trigger) digitizing and read-out continued to conclusion as long as the beam signal B0·B1 was also satisfied. After an abort, a 150 μsec settling time was required by the digitizing system. During this period the trigger logic was gated off by the LAC Clear Busy (LCB) signal. A schematic of the pre-trigger logic is included in Figure 15.

The total ρ and V-trigger logic can be written as:

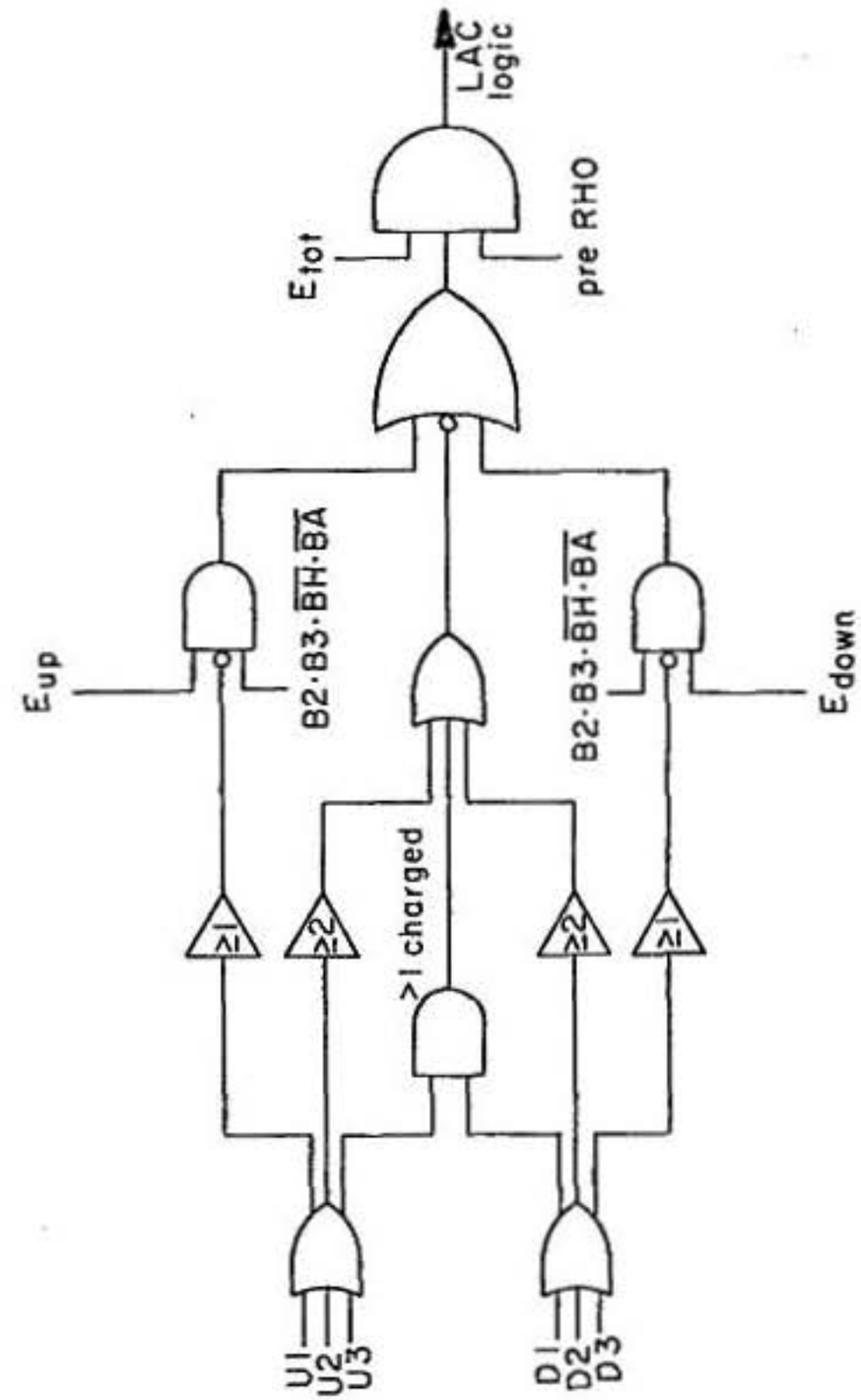

Figure 14

$$\rho \equiv B_{gated} \cdot \text{CHARGED VETO LOGIC} \cdot SO \cdot TC_{\rho} \cdot \overline{(MBV^2 + VE)} \cdot \check{C}(OR) \cdot \gamma\text{-LOGIC}$$

$$V \equiv B_{gated} \cdot \text{CHARGED VETO LOGIC} \cdot SO \cdot \overline{S1} \cdot TC_{V} \cdot \overline{MBV^2} \cdot \check{C}(OR)$$

where $\check{C}(OR)$ is the logical sum of tagging signals from the three Cherenkov counters, i.e. each trigger required a species (π^+,K^+, or P) identifying signal. Specifically, all candidate $K^{*+}(890)$, or beam kaon decay triggers, required that the signal X12 be present. B_{gated} was that portion of the beam flux signal B, taken during the one second "spill" of beam particles, remaining after imposition of the $\pm$200 nsec dead time and the LCB gates, and further gated by the data acquisition computer.

Typical ρ and V-trigger rates on the lead target were $\sim 1.2 \times 10^{-4}$ and $\sim 1.5 \times 10^{-5}$ per incident kaon, respectively. Special data tapes were also written with various signals (such as MBV^2,VE,TC_{ρ},TC_V) removed from the triggers, for purposes of studying their effects in order to tune the Monte Carlo program for calculation of geometric acceptances and reconstruction efficiencies.

Other triggers of interest included two types of non-interacting beam triggers. One of these was the "random beam-trigger" whose requirements were given by the logical product

$$\text{RANDOM BEAM} \equiv B_{gated} \cdot BV \cdot BA \cdot PULSER$$

when the BM109 magnet was on. Triggers of this type, taken concurrently with other data, were generated by a well-defined beam particle gated by a pulser whose rate was adjusted to accept $\sim$5 of these type of triggers per spill. Data from this trigger were used to determine:

(i) beam flux corrections

(ii) target related flux corrections

(iii) spectrometer related flux corrections

(iv) beam intensity related effects in the DWC's

(v) efficiency of data acquisition and contamination of various data signals.

Items (i), (ii), (iii), and (v) will be discussed in greater detail in Chapter V, and item (iv) will be addressed in Chapter IV.

For purposes of obtaining alignment data for the MWPC's and DWC's, this trigger was also used with the BM109 magnet off, and the BA and pulser requirements removed, to accept "straight-through" beam particles.

The other beam trigger was known as the "first beam-trigger" because it had the same definition as the random beam trigger, but with the pulser gate removed and replaced with a gate generator that gated this trigger off for the remainder of the spill after its first fulfillment. This initial trigger was almost assuredly the first well defined, unscattered beam particle to enter the spectrometer after the gate defining the spill was opened. This spill gate opened 0.01 sec after protons from the main ring were delivered to the Meson-Center target and beam began to come down the M1 beam line and was closed at the end of the 1 sec duration "flat-top." This trigger was useful for obtaining DWC alignment data with the BM109 magnet on before the time that beam generated space-charge in the DWC's became deleterious.

The last trigger of interest was the calibration trigger. This trigger was initiated by the on-line computer between spills, and was associated with the calibration pulsing of the MWPC's, DWC's, and LAC, as previously described. The elements of these five triggers are diagrammed in Figure 15.

For the absolute energy calibration of the LAC, a special trigger was set-up utilizing elements of the ρ-trigger. The MBV^2 and VE vetoes were removed as was the LAC γ-logic. The M1 beam line was tuned to transport 50 GeV/c negative secondaries, and the K1 Cherenkov counter was set to identify electrons. This was the sole Cherenkov signal used in this trigger. The TC logic was modified to take account of the possibility of bremsstrahlung photons from electrons radiating in the MWPC's. A series of dedicated runs were executed with this trigger, results from which will be discussed in the next chapter.

Upon fulfillment of any of these triggers, the on-line computer gated off the experiment (i.e. beam counting scalers, data acquisition logic, and other digitizing modules), and reading of digital information via the CAMAC interface was initiated. This data was then written to magnetic tape at 800 bpi for permanent storage and analysis by the off-line reconstruction and analysis programs. A block diagram of the data flow is given in Figure 16.

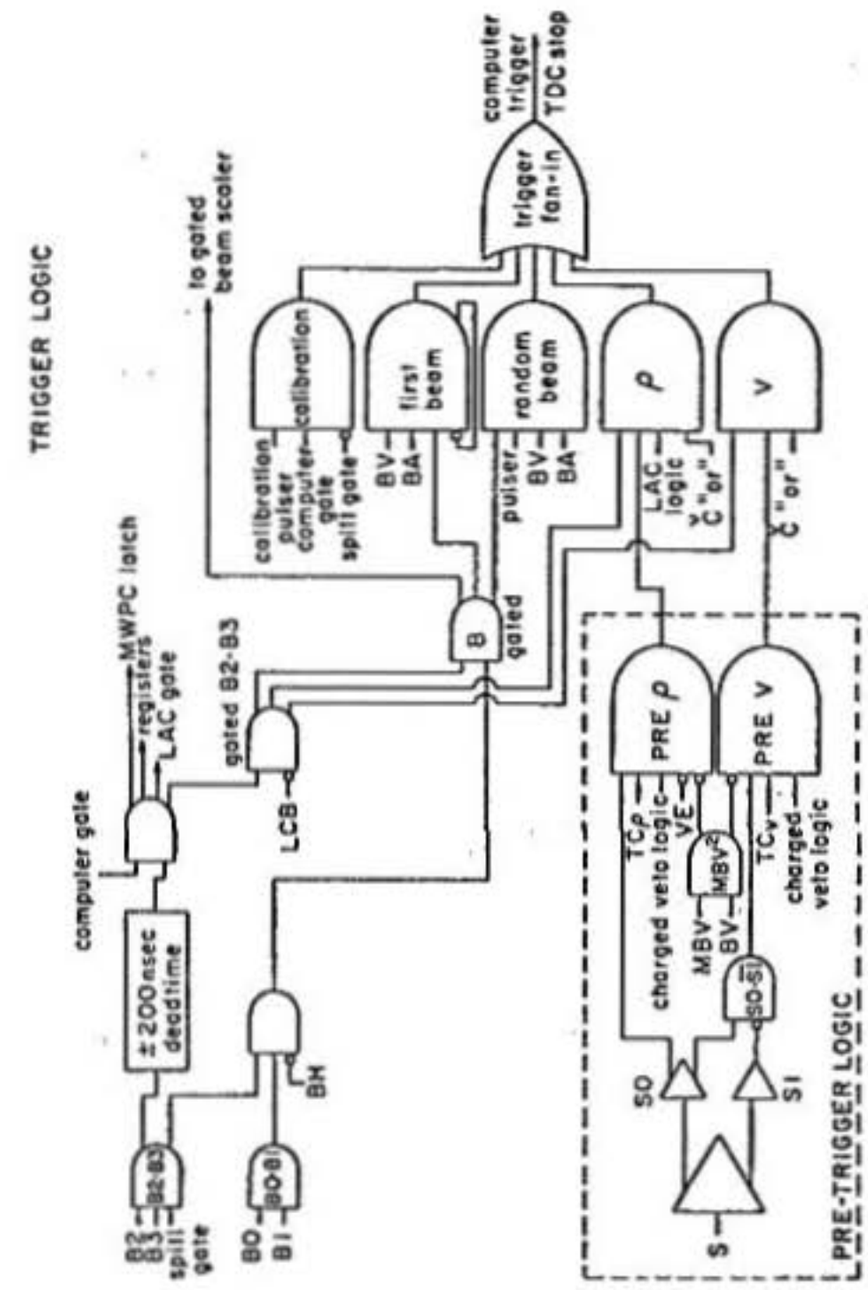

Figure 15

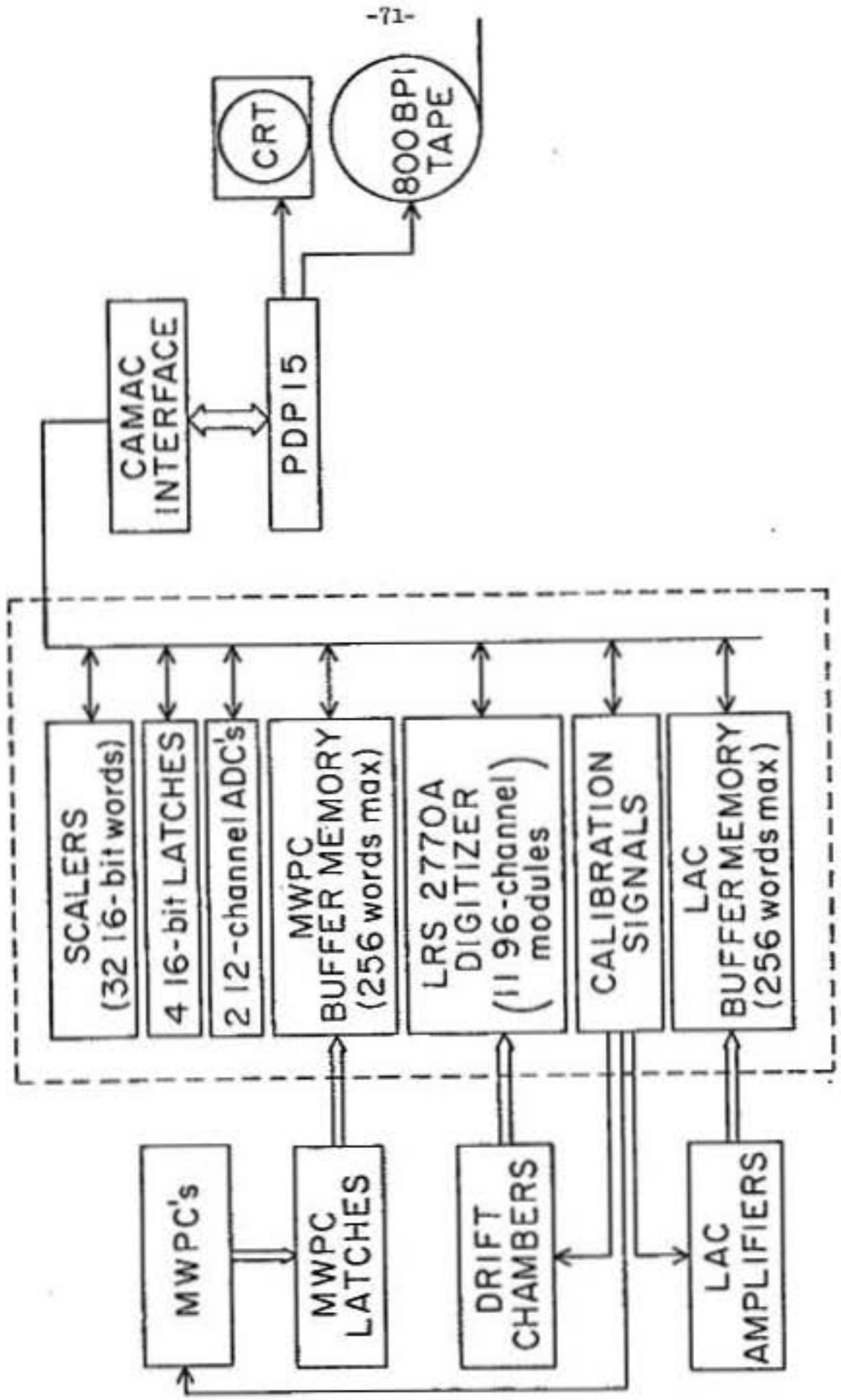

Figure 16

CHAPTER IV

CALIBRATION OF SPECTROMETER

A. Alignment and Calibration of the Wire Chambers

Data from straight-through beam triggers, described in Chapter III Section E, were used to align the MWPC's and provided initial alignment and calibration data for the DWC's. This data was taken with the BM109 magnet off.

The beam defining MWPC's, J1 and J2, were used to define the laboratory coordinate system with the z-axis defined by, and pointing along, the central axis of the beam for a nominal beam tune. The positive y-axis pointed vertically, and the x-axis was defined to have a right-handed coordinate system.

The z-positions for all of the MWPC's were measured with a tape measure, and the chambers were assumed to be perpendicular to the z-axis and at their designed angular orientations. Also, the sense wire spacings were assumed to be constant across the active area of each chamber and at their nominal values. The alignment parameters for the MWPC's were thus limited to their z-positions, and their transverse positions, which were defined by the distances of the sense wires farthest from the z-axis.

The alignment parameters for the J1 and J2 chambers were measured relative to the centroids of x and y distributions for the aforementioned beam tune. Data from hits in these chambers was

then used to project each beam track trajectory to the downstream MWPC planes, and to predict the position of the track in these chambers. The deviation between this projected position and the assumed position of the wire that signaled the passage of the particle was formed, summed over all events, and then minimized. Thus, the offset of the assumed chamber position from its actual position was defined by the mean of the deviations. The distribution of the deviations had a characteristic width due to the finite resolution of the MWPC's. No correlations were found between the deviations of the x and y chambers. This result justified the assumption that the MWPC's were mounted at their designed angular orientations.

A similar projection of beam particle trajectories to each of the DWC planes was performed to extract a relationship between position in the traversed drift cell and the measured drift time, as well as to determine the alignment parameter characterizing the plane's transverse position. Again, the z-positions of the chambers were determined with a tape measure, and perpendicularity to the z-axis, nominal angular orientations, and fixed nominal sense wire spacings were assumed. These last two assumptions were relaxed in a later analysis. In principle, the absolute space-time calibration of each chamber could yield the ionization electron drift velocity in the argon-ethane gas mixture (assuming a linear relationship), and an overall zero point for timing measurements. These parameters are related to the slope and intercept of the position versus time, respectively.

One final approximation assumed throughout this analysis is that the measured drift time does not correspond to the charged track's distance of closest approach to the sense wire, but to the distance measured perpendicularly to the z-axis. The distinction is unimportant for the small angles of inclination considered here, or in our subsequent analysis.

Before pursuing the methodology of this first approach to DWC calibration, an aside on the calibration of the drift time digitizers is in order. As mentioned in Section C of Chapter III, between spills, computer controlled pulsing of the DWC amplifiers was performed. The time delay between these pulses and the ensuing calibration trigger, which also acted as a stop signal to the digitizers, was cycled through four delays that were spaced at 50 nanoseconds. A fit by a least squares method to a straight line established a relationship between absolute time, t, and the related number of digitizer counts, c. The parameters of this relationship consisted of a gain, g, and an offset, b, for each digitizer channel for every data run. For real data, the absolute drift time in a given DWC cell was then given by $t = g \cdot c + b$.

The preliminary DWC calibration and alignment consisted of fitting the distribution of the J1 and J2 projected positions x_p at each DWC plane versus measured drift time, summed over all events, to the form $|x_p - s| = v_D(t - t_o)$. A plot of these distributions for typical upstream and downstream chambers is shown in Figures 17a and b. Here, s is the assumed position of the firing sense wire, v_D is

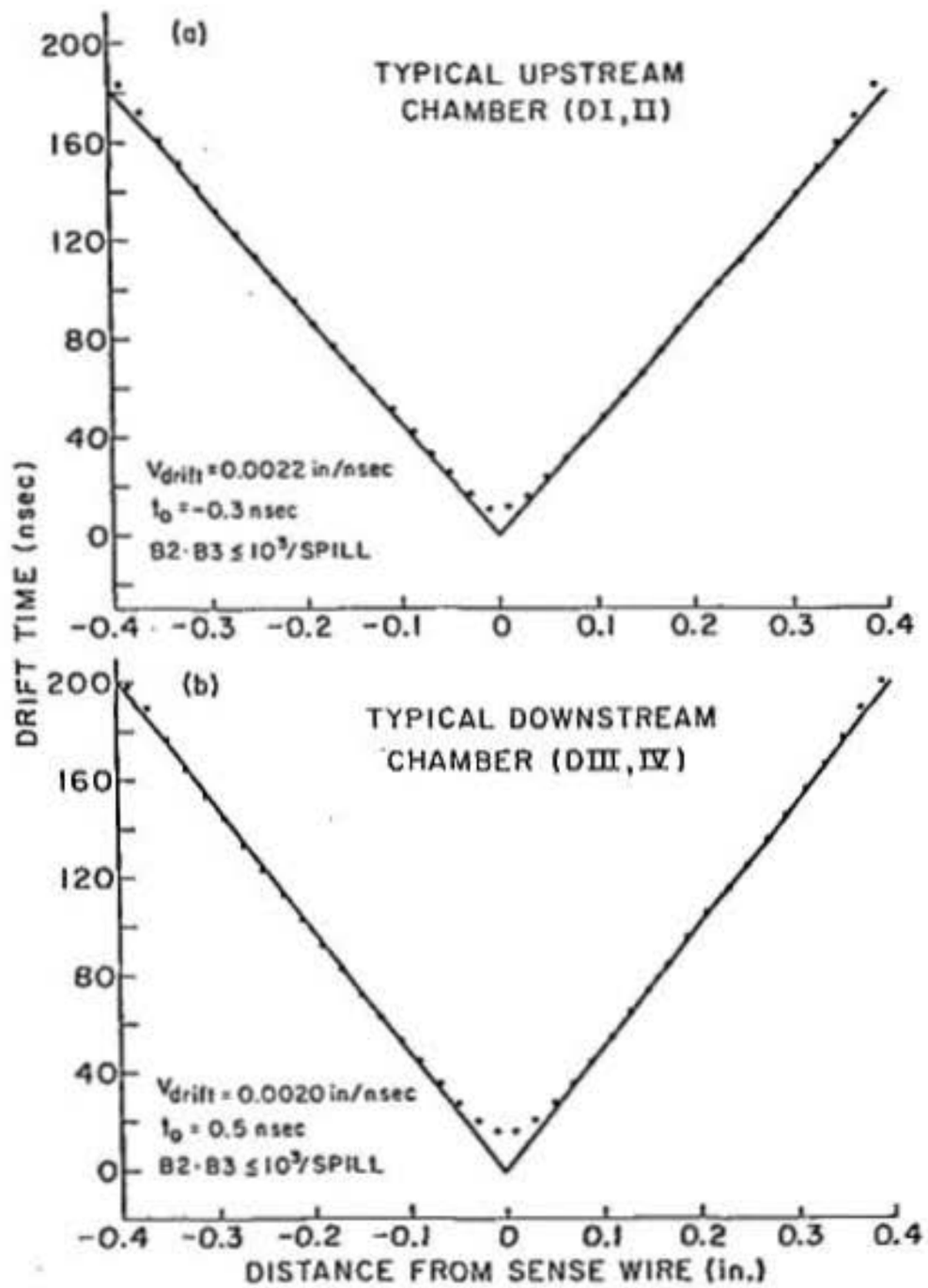

Figure 17

the drift velocity, and t_o is an overall time offset relative to the actual time of the charged particle's passage through the chamber. We can write $s = x_o + \varepsilon$, where x_o is the actual position of the signalling wire, and ε is a correction to be applied to the assumed position. The parameters ε, v_D, and t_o were then solved for by a least squares method for each chamber.

The resultant corrections ε were applied to the starting values for the DWC alignment parameters, and an average drift velocity and time offset were separately calculated for the upstream and downstream chambers. This upstream/downstream separation was maintained because of their differing field wire geometries. This method was iterated until the parameters converged (5 iterations).

This procedure suffered from four shortcomings. One was that the error in the projected position of the beam particle trajectory worsened with distance from the beam MWPC's ($\sigma \sim 0.02$ inches at the position of DIV), and consequently discontinuities in the space-time relationship near the sense wire, and at the edge of the drift cell, became smeared and rounded out. Another was that it sampled only the central portion (radius $\lesssim 0.5$ inches) of each chamber. The third problem was that, even at low beam intensities ($\sim 40\text{-}50 \times 10^3$ particles/spill), these space-time distributions became distorted by the presence of the beam as a result of the build-up of space-charge in this region. Figures 18a and 18b show this effect on two representative chambers. This accumulation of space-charge also manifested itself in a local reduction in chamber efficiency in

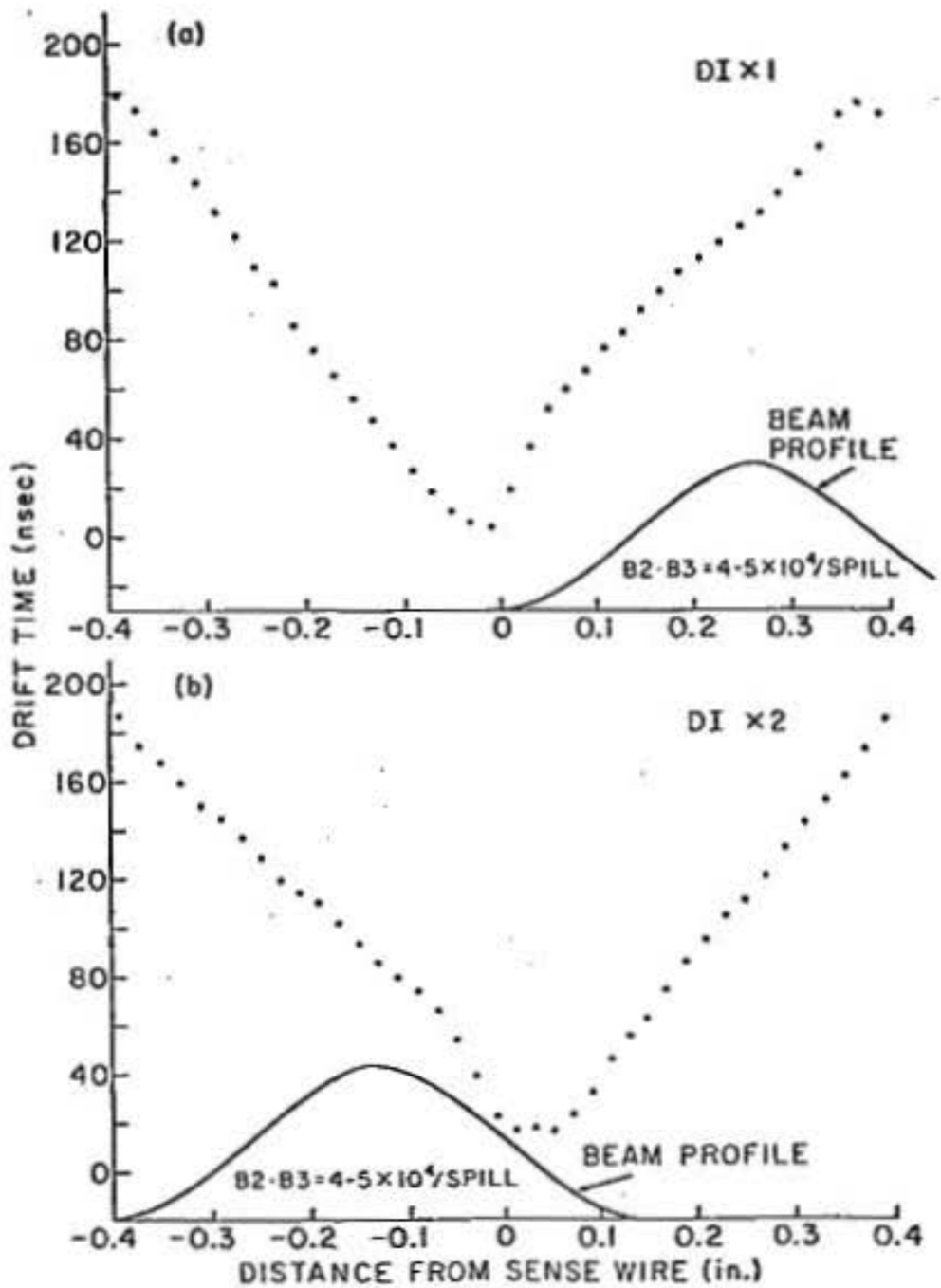

Figure 18

the beam region. This was reflected in the reconstruction efficiencies for "first beam" events, which consisted of beam triggers taken near the beginning of the spill, and random beam triggers, which selected beam events throughout the spill. In the former case, reconstruction of the beam track through the DWC's exceeded 95% efficiency while only ~5% of the latter type events were reconstructed. This effect limited the straight-through beam DWC calibration data to just two tapes taken at intensities of $\lesssim 10^3$ particles/spill. The final drawback was that only a limited region of each drift cell was sampled due to the small size of the beam relative to the drift space. Such an effect certainly caused bias in the fits.

In order to circumvent these difficulties, a more sophisticated approach to fine-tune the calibration was employed. Again, each chamber was separately fit for the parameters ε, v_b, and t_o; however, deviations in the chamber angular orientations, $\Delta\theta$, in its z-position, Δz, and a possible uniform scaling factor in the sense wire spacing, ε', were also admitted. For this analysis, two samples of ρ-triggers, with one and only one hit in each of the twelve upstream and downstream chambers, were selected. These data were obtained with the BM109 magnet on, and therefore the upstream and downstream chambers were treated separately with no connection made between the two.

This fitting procedure made use of the better resolution of the DWC's per se to find the charged particle trajectory. Also, because

the major fraction of the data upstream of the BM109 was outside of the beam region, and the BM109 magnet further dispersed the tracks, this facilitated sampling across the area of the downstream chambers, and provided a uniform sampling across the drift cell.

The data were used to form the deviations ϵ_{ij} between the measured and the expected position of passage of each particle through each plane, with upstream and downstream data treated separately. That is

$$\epsilon_{ij} = b_{xj}z_i\cos\theta_i + b_{yj}z_i\sin\theta_i + x_{oj}\cos\theta_i + y_{oj}\sin\theta_i \mp v_{D_i}(t-t_{o_i}) - s_{ij}$$

where the subscripts label the jth event in the ith plane and

$$\epsilon_{ij} = \epsilon_i + \epsilon_i' U_{ij} + \Delta\theta_i V_{ij} + \Delta z_i W_{ij}$$

is the total deviation, with contributions from an overall transverse displacement of the chamber, a uniform scaling of the sense wire spacing, an offset in the angular orientation of the chamber, and an offset in the chamber's measured z-position. Only terms to first order in the corrections have been retained. Here

$$U_{ij} = b_{xj}z_i\cos\theta_i + b_{yj}z_i\sin\theta_i + x_{oj}\cos\theta_i + y_{oj}\sin\theta_i$$
$$V_{ij} = -b_{yj}z_i\cos\theta_i + b_{xj}z_i\sin\theta_i - y_{oj}\cos\theta_i + x_{oj}\sin\theta_i$$
$$W_{ij} = -b_{xj}\cos\theta_i - b_{yj}\sin\theta_i$$

and the +/- sign multiplying v_D results from the left-right ambiguity of position within a drift cell. The proper sign for each

event in each plane was chosen using the charged particle reconstruction program, using initial calibration constants for the DWC's. This was the only input from the reconstruction program to the calibration analysis.

In the above expressions, z_i and θ_i are the assumed z-position and angular orientation of the ith DWC, and b_{xj}, b_{yj}, x_{oj}, and y_{oj} are the x and y slopes and intercepts, respectively, of the jth particle trajectory. The trajectory parameters were obtained using data from the other eleven DWC's, with the ith chamber completely passive. The over-determined set of equations given above were then solved by a least squares method to give ϵ_i, ϵ_i', $\Delta\theta_i$, Δz_i, and a drift velocity v_{D_i} and time offset t_{o_i}, for each plane. Starting values for ϵ_i, v_{D_i}, and t_{o_i} were from the preliminary DWC calibration, and it was initially assumed that $\epsilon_i' = \Delta\theta_i = \Delta z_i = 0$. This procedure was then iterated until the parameters converged (6 iterations).

In practice, the scattering angles for the upstream tracks were too small for this procedure to be sensitive to $\Delta\theta_i$, Δz_i, or ϵ_i'. However, the angles of the downstream data proved to be sufficiently large to show that these parameters were consistent with the nominal values (i.e. $\Delta\theta_i = \Delta z_i = \epsilon_i' = 0$).

Final results of the fitting showed that none of the DWC transverse positions changed by more than 0.005 inches relative to the first pass alignment analysis, and that for the downstream chambers $|\Delta z| < 0.05$ inches, $|\Delta\theta| < 0.5$ mrad, and $|\epsilon'| < 3 \times 10^{-4}$. Once it

was seen that these extra terms gave a negligible contribution to the deviations, the fits were limited to the three parameters ϵ_i, v_{D_i}, and t_{o_i} for each plane. Again, an iterative procedure was initiated until stable values were reached. An average of the upstream drift velocities and time offsets gave 0.00202 inch/nsec and -14.8 nsec, respectively, and for the downstream set of chambers, the averages were 0.00194 inch/nsec and -17.4 nsec. Figures 19a and 19b show the space-time relationship, summed over all upstream and downstream chambers, respectively, using linear fits to the data and using the values quoted above. In the reconstruction of real data, separately fitted drift velocities and time offsets were used for each chamber.

Figures 20a, and 20b show, respectively, the distribution of deviations of measured from predicted positions (using results of the final analysis) for data summed over all upstream, and downstream chambers. Unfolding the error in the extrapolated charged-particle position, these distributions give RMS widths of 0.008 inches and 0.010 inches for upstream and downstream results, respectively; these values reflect the resolution of the DWC's, and imply angular resolutions of $\Delta\theta_x = 0.06$ mrad, $\Delta\theta_y = 0.08$ mrad, and $\Delta\theta_x = 0.04$ mrad, $\Delta\theta_y = 0.15$ mrad, for the upstream, and downstream sets of DWC's, respectively.

Figures 21a and 21b show, for data summed over all upstream and downstream chambers, respectively, the distribution of deviations as a function of position within a drift cell. The differences

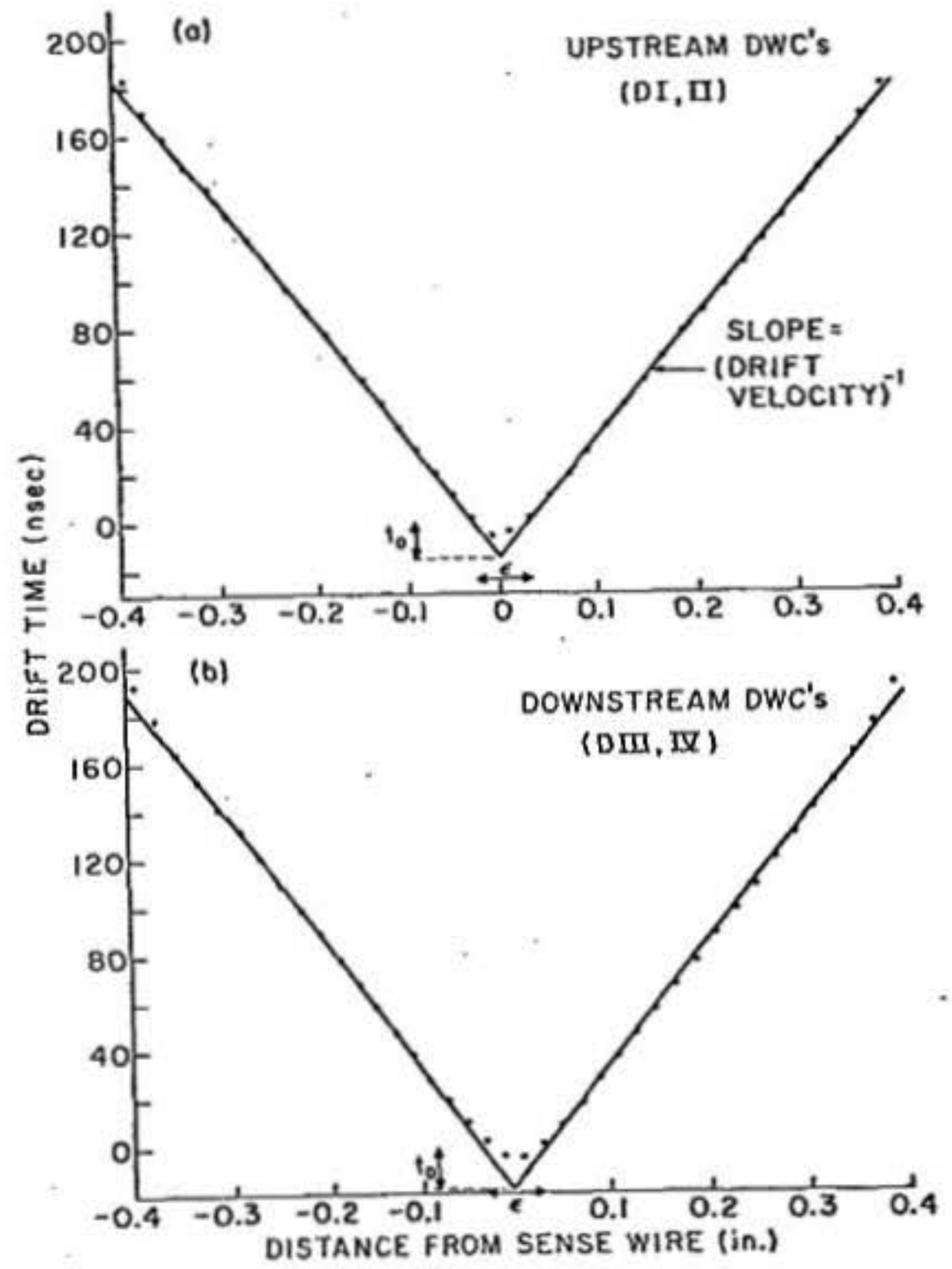

Figure 19

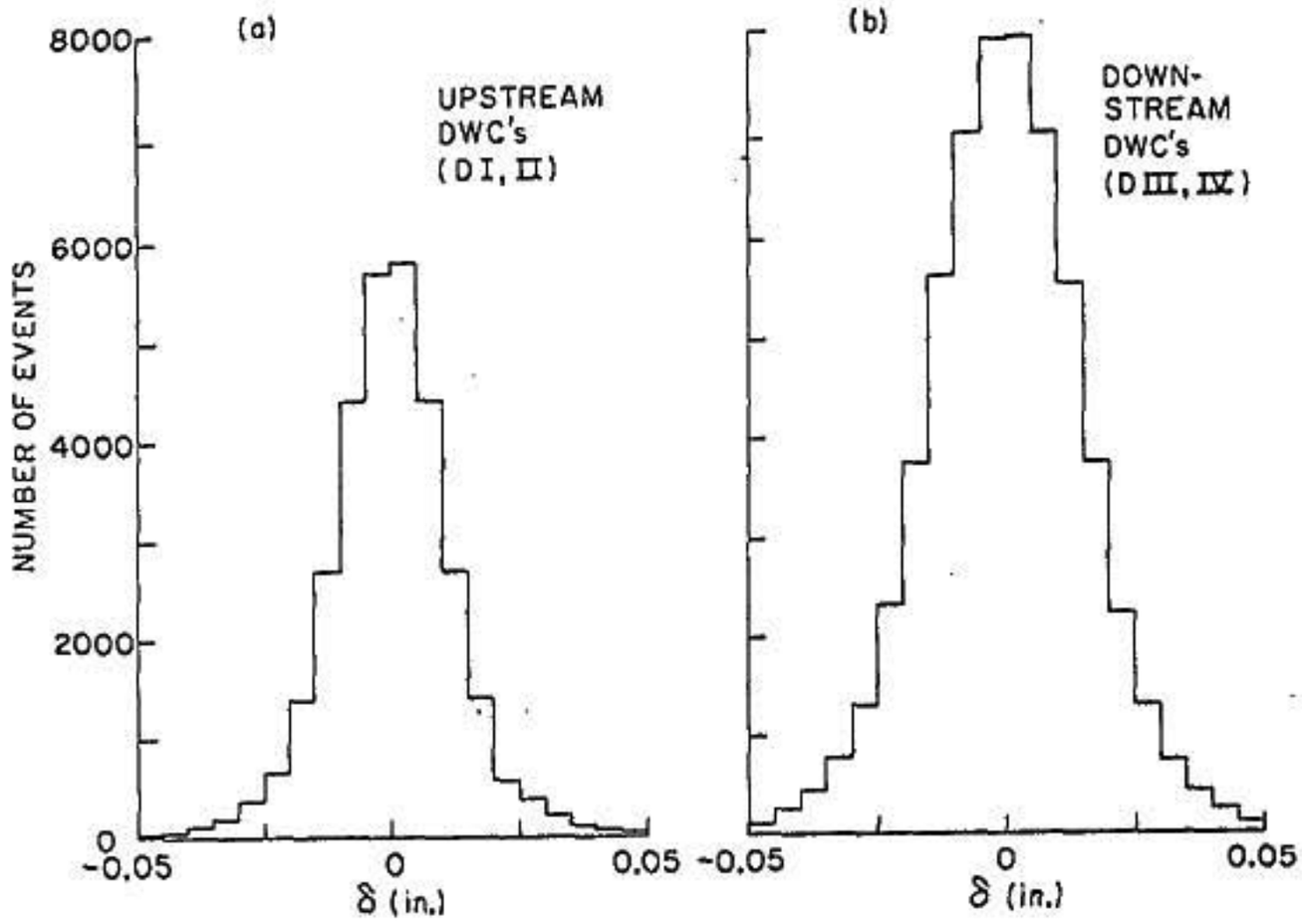

Figure 20

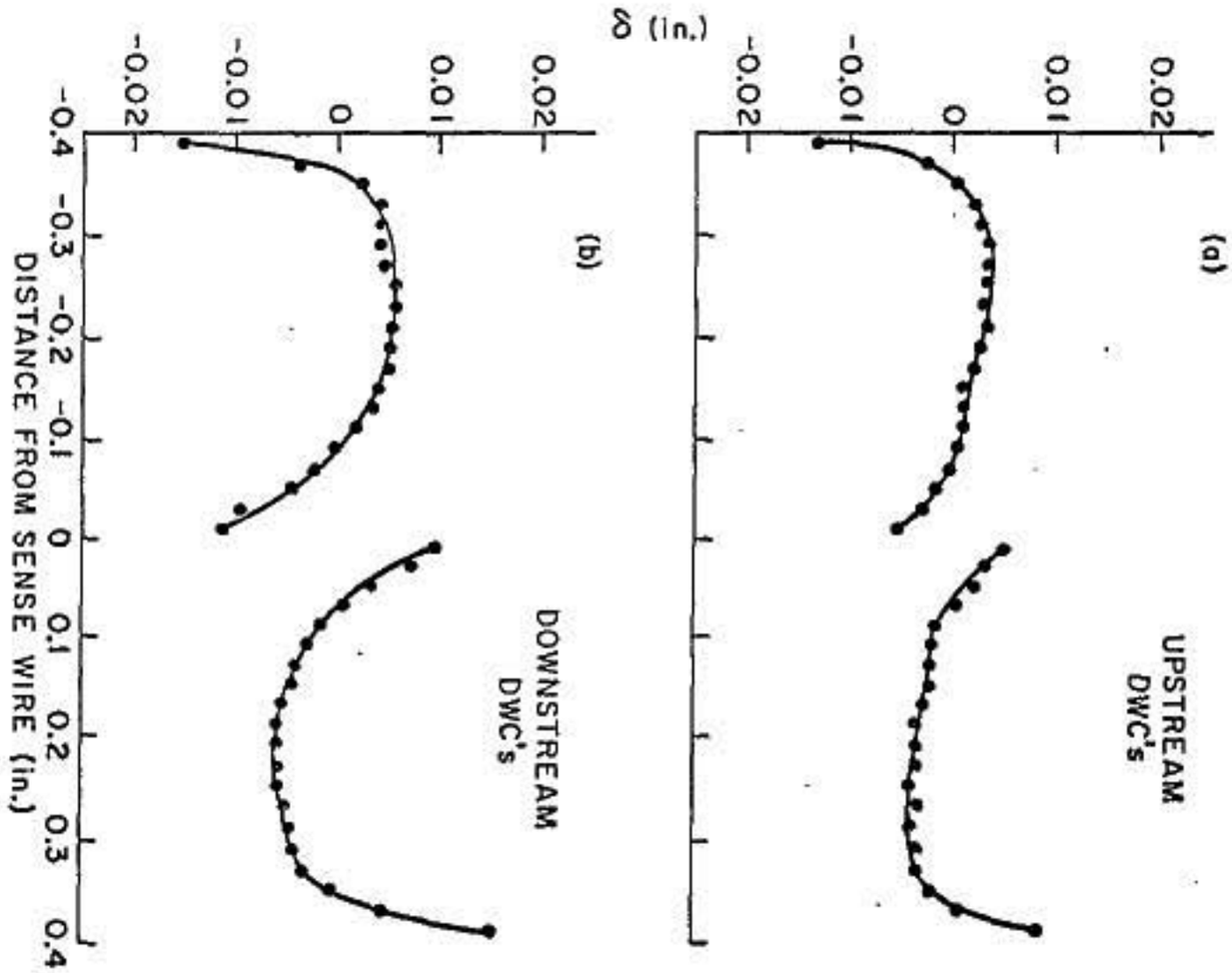

Figure 21

between the two can be attributed to the different field-shaping wire geometries (see Figures 9a and 9b).

These distributions exhibit a departure from linearity in the space-time relationships near the sense wire and at the edge of the drift space, and can be attributed to the non-uniformity of the electric fields in these regions. Also, effects from the time development of the induced pulse on the sense wire come into play for those particles passing very near to the sense wire.[59] An interesting consequence of the antisymmetry of the deviations about the sense wire is that the deviations from pairs of chambers mounted in the offset doublet configuration are anticorrelated for small angle trajectories and, providing each chamber detects the passage of a given charged particle, the effects of this non-uniformity in determining its position tend to cancel.

Figures 22a and 22b show, for upstream and downstream chambers, respectively, the RMS widths of the distributions of deviations with projection errors removed, as a function of distance from the sense wire. The decrease in resolution error near the sense wire is presumably a result of primary ionization statistics, and that near the edge of the drift cell can be attributed to dispersing effects over large drift distances.[60] The effect of having more field shaping wires in the upstream chambers on the resolution is also apparent.

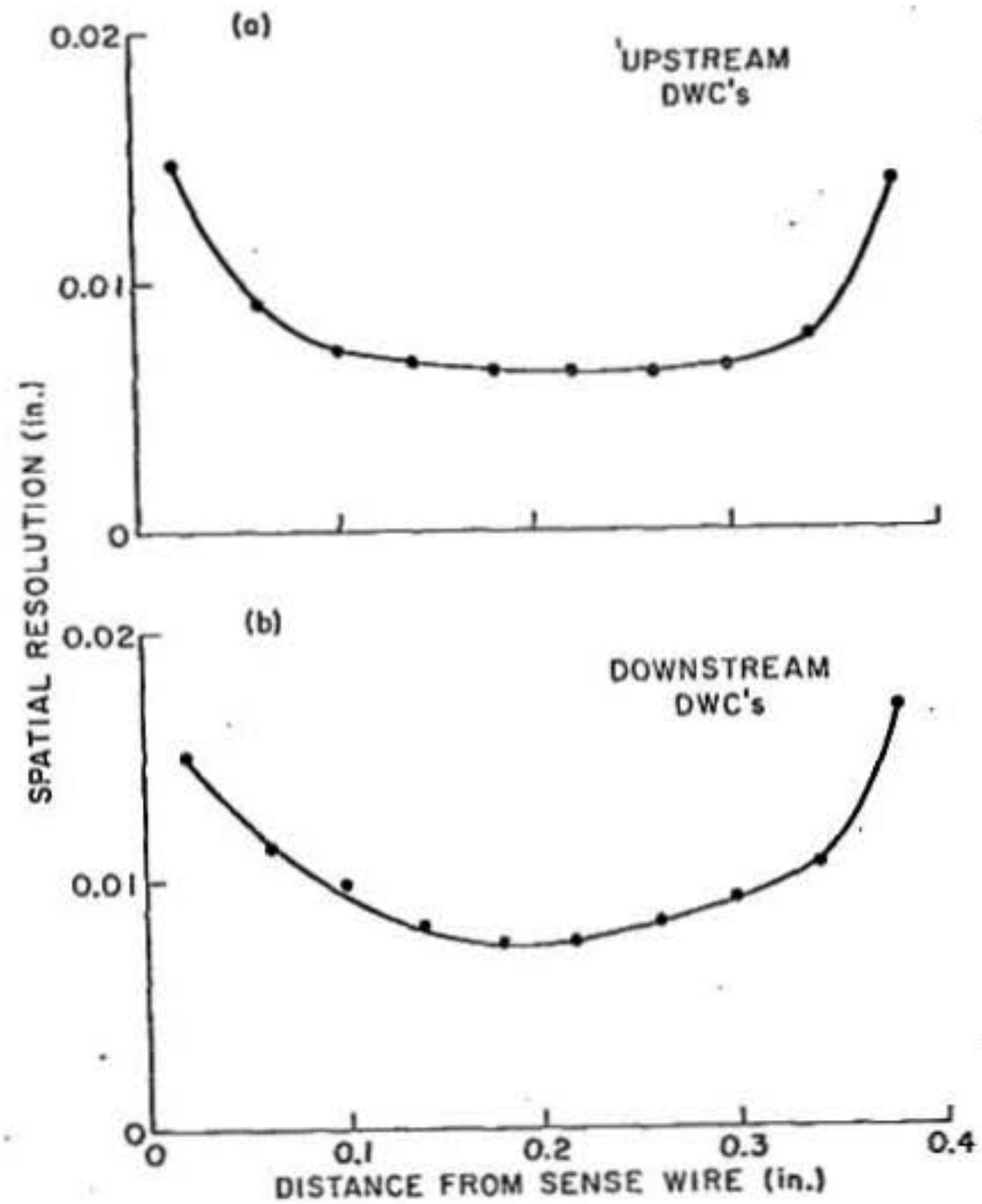

Figure 22

B. Calibration of the Momentum Analyzing Magnet

The BM109 dipole magnet was used to determine charged-particle momenta. It was assumed that the integral of the magnetic field along a trajectory was constant, and, in fact, a study showed that the impulse was entirely in the bending (x-z) plane. A possible rotation of the field about the z-axis (or a rotation of the upstream DWC system relative to the downstream system; the effects are the same) was investigated using ρ-trigger events that had one and only one hit in each of the DWC's. A rotation of this sort would manifest itself in causing the measured downstream x and y slopes of the trajectory, b_x' and b_y', to be mixtures of the true slopes, b_x and b_y (here we treat the problem as if these were rotations of the chambers). That is, $b_x' = b_x\cos\theta + b_y\sin\theta$ and $b_y' = b_y\cos\theta - b_x\sin\theta$. Assuming θ is small, we have $\theta = (b_y - b_y')/b_x'$. The true slope b_y can be equated with the upstream y-slope, because the magnet is assumed to bend in only the x-z plane. The mean of the distribution of θ obtained from these events showed that any such a rotation was negligible.

The z-position of the center of the magnet was determined by finding the z-position of the intersection (z_{vertex}) of upstream and downstream particle trajectories extrapolated to the magnet. For upstream trajectories with x and y slopes near zero, and a bending angle of ψ through the magnet, the z-position of the center of the magnet z_o is given by $z_o = z_{vertex} - L\psi^2/8$. Here L is the length of the magnet, and an approximation for small ψ has been used. The

term proportional to ψ^2 arises from the momentum dependence of the z_{vertex} position; this sort of term was negligible for the sample of data used to determine z_o.

Charged-particle momenta were calculated in the small bending angle impulse approximation, i.e. $p = \lambda/\psi$. Here ψ is the bending angle through the magnet, given by the difference in the horizontal slopes of the entrance and exit particle trajectories, and λ is the transverse impulse δp imparted to the charged particle.

Since the magnet position and angular orientation were well established, calibration of the BM109 magnet consisted merely of determining λ. This was done to first order by scaling with magnet current values obtained from other operating currents. A fine tuning of λ was performed using the reconstructed mass of $K_s^o \to \pi^+\pi^-$ events resulting from $K^{*+}(890)$ decay. These events were first reconstructed using the initial value for λ, and λ was then modified according to $\lambda \to (1 + \varepsilon)\lambda$ so that the mean of the $\pi^+\pi^-$ mass spectrum (assuming it to be Gaussian-distributed) coincided with the accepted value for the mass of the K_s^o.

It can be shown in the high energy limit that, if we measure a mean mass of m' for the K_s^o when its true value is m, ε is given by $\varepsilon = (m^2 - m'^2)/2(m'^2 - 2m_\pi^2)$. An analysis of this sort indicated that λ had to be increased by a factor of 1.017, giving a final value for the magnet transverse kick of 1.082 GeV/c. A Gaussian fit to the $\pi^+\pi^-$ mass spectrum (ignoring non-Gaussian tails), applying this correction to the K_s^o mass is shown in Figure 23a.

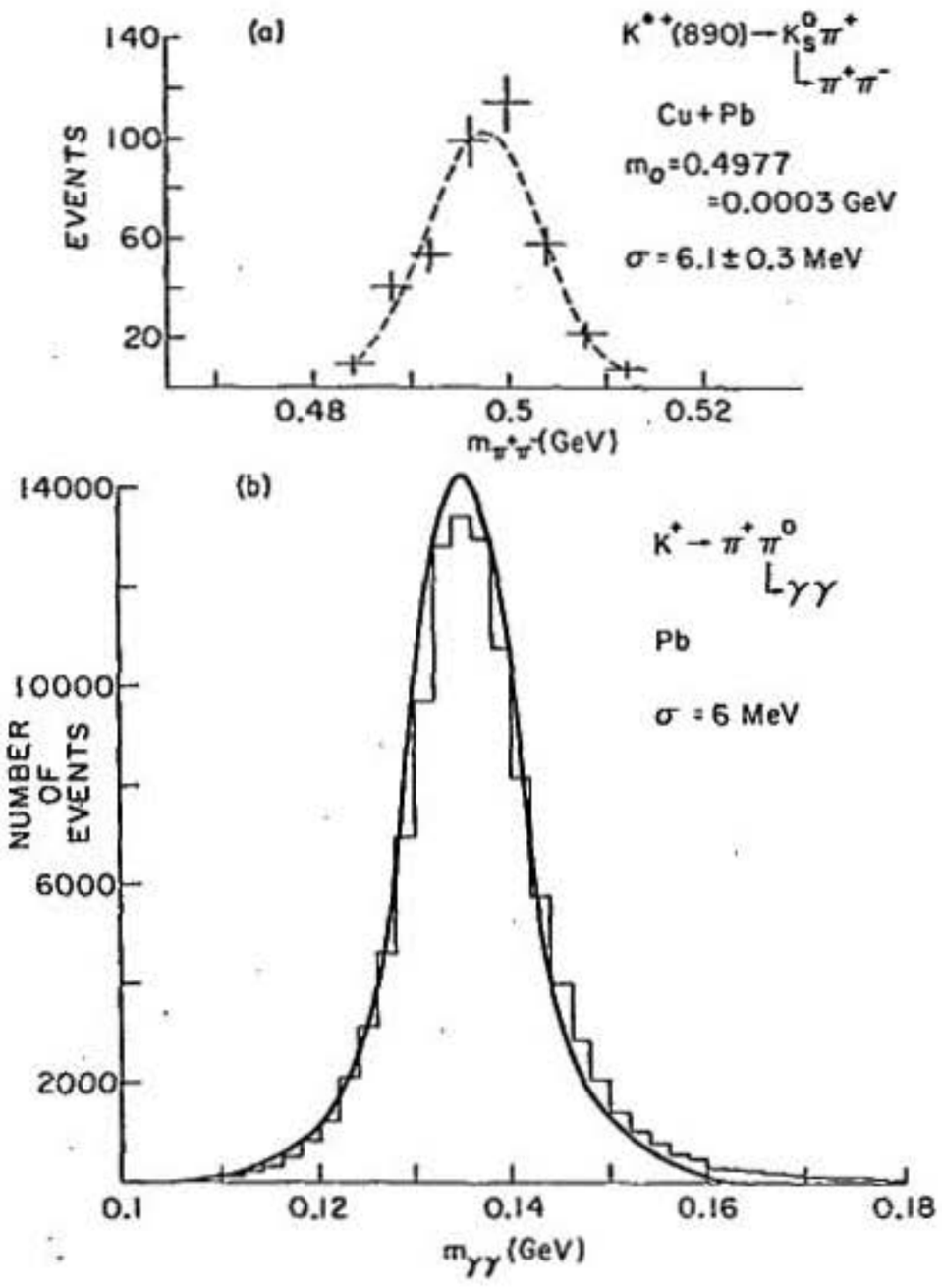

Figure 23

The mean of the $\pi^+\pi^-$ mass in this fit coincides with the accepted K^0_S mass[51], and indicates a resolution of 6 MeV for the $\pi^+\pi^-$ invariant mass.

Subsequent to the correction of the magnetic field, the total energy of these same $K^{*+}(890)$ events was recalculated, and from a Gaussian fit to this distribution, yielded a mean value of 203.6 ± 0.1 GeV. To check for consistency, the energies of a sample of beam $K^+ \to \pi^+\pi^+\pi^-$ decays from the target region was also fitted to a Gaussian for the reconstructed total energy and provided a mean value of 203.4 ± 0.1 GeV; a Gaussian fit to the reconstructed $\pi^+\pi^+\pi^-$ invariant mass gave a mean value of 494 MeV, in excellent agreement with the accepted value. These results implied the true incident beam momentum was approximately 204 GeV/c.

As a final remark, the angular resolutions of the DWC's implied a resolution on the bending angle of ± 0.07 mrad. This translated into a momentum resolution of $\Delta p/p = 6.5 \times 10^{-5}$ p for each charged track. The reconstructed momentum distribution for beam triggers accumulated with the BM109 magnet on (via the "first beam" trigger) had an RMS width of ∿7 GeV/c. Unfolding the contribution to this width from the uncertainty in measuring momentum indicated a momentum spread of the incident beam of ∿6 GeV/c (RMS dispersion).

C. Calibration of the Liquid Argon Calorimeter

In analogy with the calibration of the drift time digitizers, the pulse-height digitizers for each of the LAC channel amplifiers

were pulsed with calibration triggers between spills to extract the analogous electronic calibration parameters, namely, the gain and pedestal. For every data run, an average pedestal and gain were calculated for every channel. The variations in electronic gains throughout the running period were negligible, and all were therefore set to unity. The absolute calibration of the LAC using beam electrons compensated for channel-to-channel variations in overall gain. The calculated mean values for the channel pedestals for each run were subtracted from the number of digitizer counts in real data. The pedestal levels varied somewhat with incident beam intensity, especially near the beam hole of the detector. An empirically determined pedestal correction, depending on beam intensity, was therefore applied to the channels in this region.

The overall calibration for converting the counts in each LAC channel digitizer to an absolute was obtained using a 50 GeV/c electron beam. At this momentum, the M-1 secondary beam contained ∿10% electrons. These electrons were tagged with the K1 Cherenkov counter, and their momenta were determined using the DWC system and the BM109 magnet. The beam was swept veritcally across the LAC in two y scans of the detector at two separate x positions, using a dipole magnet (E1PM; see Figure 3) just upstream of the target region. To calibrate the x-strips of the LAC, the beam was pitched at two different y coordinates (again, using the E1PM dipole), and the LAC was stepped horizontally across the beam.

Once the pion background falsely tagged by the K1 counter as electrons, and electrons with accompanying bremsstrahlung photons, were eliminated from the data, the quantity $\chi^2 = \sum_i (E_i^o - E_i)^2$ was formed for each LAC channel. Here the sum on i is over all events; E_i is the energy as measured by the LAC, separately in the x and y views, and E_i^o is given by $E_i^o = P_i/2 - E_i^{BACK}$, where P_i is the momentum of the electron as measured by the charged particle spectrometer, and E_i^{BACK} is the energy deposited in the back half of the LAC; E_i^o is the energy deposited in the front of the LAC (either in the x or in the y strips).

We can write $E_i = \sum_j a_j n_{ij}$, and $E_i^{BACK} = \sum_j a_j^{BACK} n_{ij}$, where n_{ij} are the digitizer counts in the jth channel for the ith event, a_j is the calibration constant for the jth channel in the front of the LAC, and a_j^{BACK} is the same for the jth channel in the back of the LAC. Because little electromagnetic energy was deposited in the back half of the detector, these latter constants were poorly determined, and therefore assigned the constant value of 13 MeV/count. Also, energy resolution studies indicated that if the strips entering the summation above were limited to the five strips about the shower maximum, the resolution was optimized. Minimization of the χ^2 yielded the absolute calibration constants for the front channels of the LAC.

Data from these electron-induced showers were also used to determine the parameters describing the lateral development of electromagnetic showers for use in reconstructing multiphoton events. Such shape parameters were useful in separating overlapping energy

distributions for these kinds of events.

Through the experimental running period (~3 months), a slight increase in the overall gain of the detector was noted, as evidenced by an increase in the two photon invariant mass from samples of beam $K^+ \to \pi^+\pi^o \to \pi^+\gamma\gamma$ decays. As already stated, the electronic gains were essentially constant, and even though the cause of this effect is uncertain, it may be related to the gradual freezing out of electronegative impurities in the liquid argon.

To first order, this gradual increase in gain was taken into account by monitoring the two-photon invariant mass from $K^+ \to \pi^+\pi^o$ decays, and applying a linear time-dependent correction to the gains in order to force the mean of this mass distribution to roughly coincide with the accepted value for the mass of the π^o.[51] Small run-to-run variations in the π^o mass that still remained (typically <1%) were corrected further by empirically changing the gains so as to force the mean of the two-photon invariant mass in any run to coincide exactly with the mass of the π^o.

Further study of $K^+ \to \pi^+\pi^o$ data indicated a dependence of the total reconstructed energy of the K^+ on the energy of the reconstructed π^o. At high π^o energies, the total reconstructed energy distribution tended to fall off. This was attributed to leakage of some of the π^o energy out of the back of the LAC. To correct for this, each photon energy was redefined according to $E \to E' = \alpha E + \beta E^2$, where E was the original reconstructed photon energy, and α and β were parameters to be determined. These constants were obtained

from $K^+ \to \pi^+\pi^o \to \pi^+\gamma\gamma$ data by a least squares solution to the overdetermined set of equations

$$\alpha(E_{1i} + E_{2i}) + \beta(E_{1i}^2 + E_{2i}^2) = E_{total} - E_{charged\ i}$$

and

$$\alpha m_{\gamma\gamma i} + \beta m_{\gamma\gamma i}\,(E_{1i} + E_{2i})/2 = m_{\pi^o}\,.$$

Here E_{1i} and E_{2i} are the original reconstructed photon energies, $m_{\gamma\gamma i}$ is the original reconstructed two-photon invariant mass, and $E_{charged\ i}$ is the energy of the π^+, as determined by the charged particle spectrometer for the ith K^+ decay. The total energy of the event E_{total} was fixed at the previously determined value of 204 GeV, and the mass m_{π^o} was set to its accepted value. The first equation above follows from energy conservation; the second results from recalculating the two-photon mass after redefining the π^o energy, and retaining terms to first order in β.

The least squares solution yielded $\alpha = 0.9956$ and $\beta = 1.789 \times 10^{-4}\ \mathrm{GeV}^{-1}$, and all of the energy measurements from the LAC were correspondingly adjusted.

Figure 23b shows the two-photon invariant mass distribution for photons from $K^+ \to \pi^+\pi^o$ decays after the final LAC energy calibration. No restrictions have been applied to the photon energies other than those resulting from geometric acceptance, reconstruction efficiency

and cuts applied to kinematic variables of the parent K^+ (see Chapter VI for a description of cuts used to isolate K^+ decays). Ignoring the non-Gaussian tails, an RMS width of 6 MeV was found for this distribution. The superimposed smooth curve is a Monte Carlo prediction (our resolution function) normalized to the number of events with 0.110 GeV < $m_{\gamma\gamma}$ < 0.160 GeV.

Once the energy calibration of the LAC was established, a study of corrections to its nominal alignment and position parameters was initiated. Again, the position of the LAC and its rotation about the z-axis, were investigated using the $K^+ \to \pi^+\pi^o$ data. These decays occur at t = 0, and therefore the transverse momentum of the reconstructed π^o must balance that of the π^+. In the small angle approximation, the components of $\vec{P}_t$ for the π^o are given by $P_{t_x} = (E_1x_1 + E_2x_2)/z$ and $P_{t_y} = (E_1y_1 + E_2y_2)/z$, where $E_{1,2}$ are the π^o decay photon energies, $x_{1,2}$ and $y_{1,2}$ are the x and y distances of the reconstructed photons from the extrapolated beam K^+ trajectory at the LAC, and z is the distance from the point of decay of the K^+ to the LAC. The z coordinate of the point of decay was given by the z-coordinate of the midpoint of the shortest line segment joining the incident beam K^+ trajectory and the π^+ trajectory.

Defining position offsets Δx, Δy, and Δz, and an angular offset $\Delta\theta$ for the LAC, we can write for the ith reconstructed π^o:

$$P_{tx_i} = (E_1^{(i)}\ \xi_1^{(i)} + E_2^{(i)}\ \xi_2^{(i)})/z_i$$

and

$$P_{ty_i} = (E_1^{(i)}\ \eta_1^{(i)} + E_2^{(i)}\ \eta_2^{(i)})/z_i$$

where, retaining only first order terms in offsets,

$$\xi_j^{(i)} = x_j^{(i)} + \Delta x + y_j^{(i)}\ \Delta\theta - x_j^{(i)}\Delta z/z_i$$

and

$$\eta_j^{(i)} = y_j^{(i)} + \Delta y - x_j^{(i)}\ \Delta\theta - y_j^{(i)}\Delta z/z_i \quad .$$

Assuming that $-P_{tx_i}$ and $-P_{ty_i}$ are given by values from the charged-particle spectrometer for the π^+, we can extract a least-squares solution for the offsets. Results indicated that $\Delta\theta = \Delta z = 0$, to within statistical accuracy, but the x and y positions of the LAC were shifted by -0.032 inches and -0.004 inches, respectively. Such small corrections may seem negligible, but through their application the P_T resolution for $K^+ \to \pi^+\pi^o$ decays (see Chapter V) improved by ~10%, indicating the sensitivity of the data to such small effects.

The LAC energy and position resolutions for electromagnetically induced showers were determined from positrons from $K^+ \to e^+\pi^o\nu$ (K_{e3}) decays also collected along with the ρ-trigger. Figure 24a shows the correlation between the energy of the positron as measured by the LAC(E_{LAC}) and that determined by the charged-particle spectrometer (E_{SP}); the deviation between these two measurements as a function of

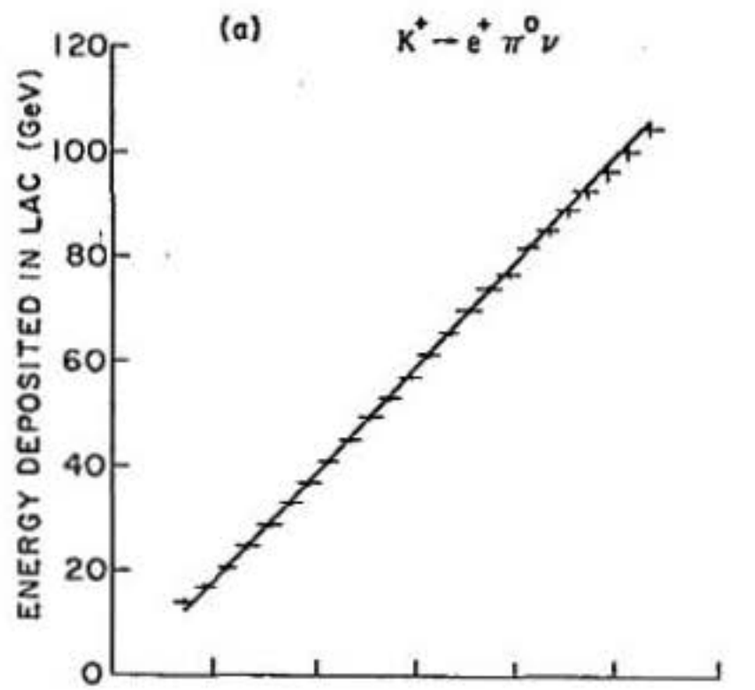

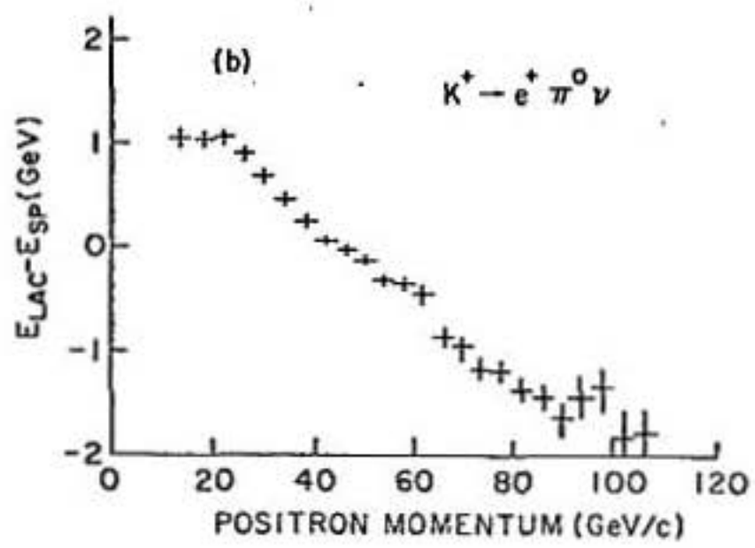

Figure 24

positron energy is displayed in Figure 24b. The linearity of response of the LAC is seen to be better than 3% over this energy range.

Figure 25 displays the variance of the deviations between the positron energy as measured by the LAC and that determined by the charged particle spectrometer, as a function of positron energy. The superimposed fit to the data has the form $\sigma^2 = (0.14\sqrt{E})^2 + (0.55)^2$. The first term reflects the sampling statistics of the detector, while the second term has its source in amplifier noise, reconstruction difficulties, drifts in amplifier pedestals and gains, and a small non-uniformity of response along the length of the charge collecting strips.

Figure 26a shows the deviation in the x-view of the reconstructed position of the positron in the LAC from its position projected by the DWC's. Unfolding errors in the DWC projection gives a spatial resolution of <0.04 inches.

Figure 26b shows the position resolution obtained for hadronic showers from π^-'s resulting from $K^+ \to \pi^+\pi^+\pi^-$ decays. This kind of data was accepted by the V-trigger concurrently with $K^{*+}(890)$ candidate events. Again, the deviations are between the position of the showering π^- as determined by the LAC and that determined from the DWC projected position in the x-view. A resolution of <0.4 inches for hadronic showers is indicated. In reconstruction of events, any distribution of energy in the LAC whose center coincided within 0.75 inches of an extrapolated charged track was tagged as a "charged-photon overlap", and this "photon" was eliminated from further consideration. Due to the large uncertainty in measuring the

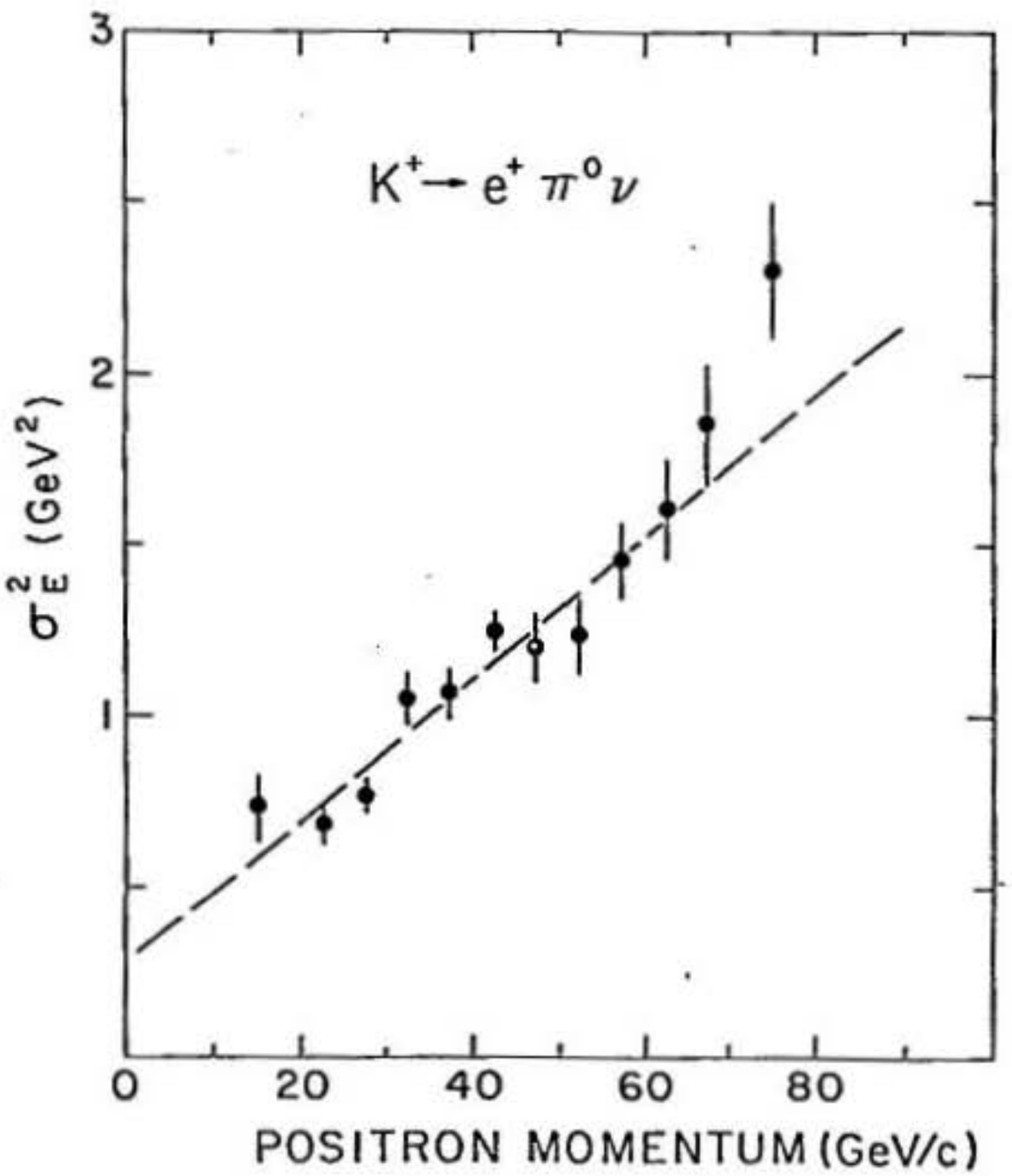

Figure 25

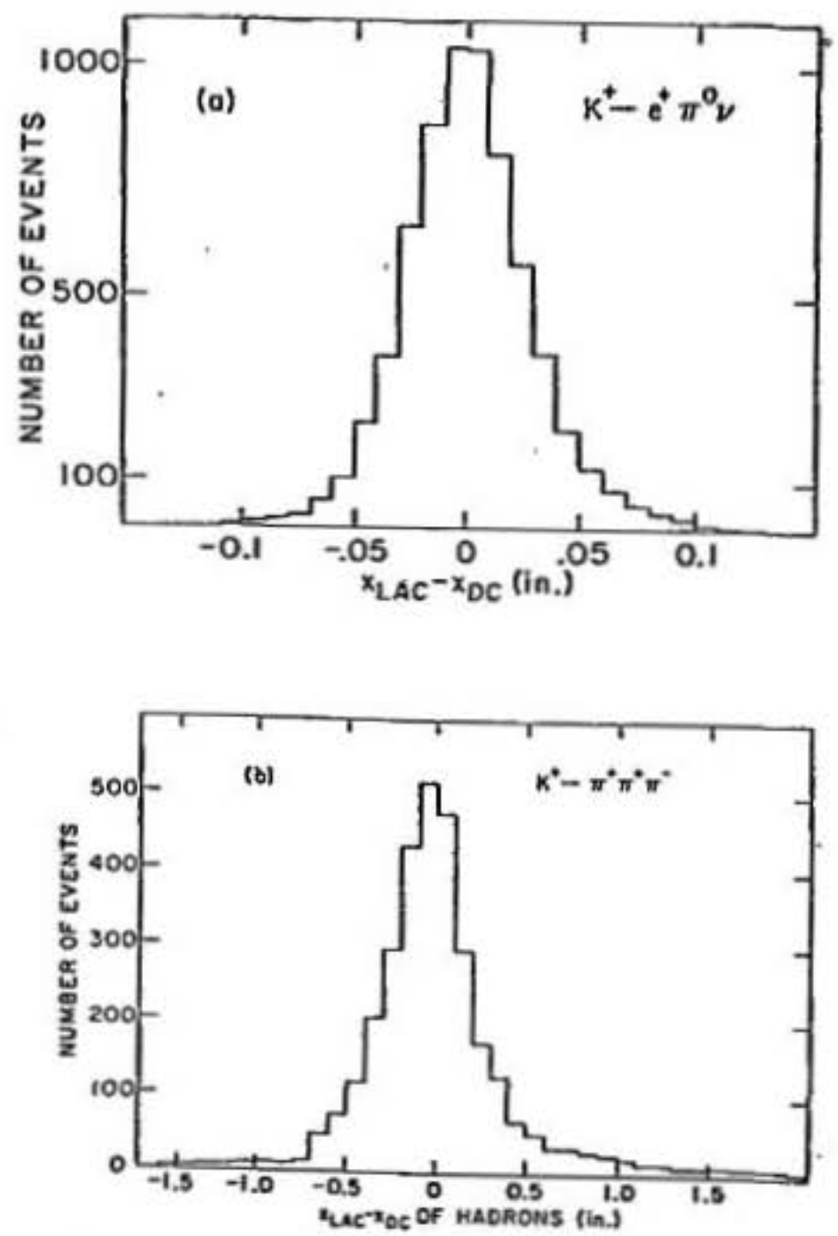

Figure 26

position of hadronic showers in the LAC, occasionally interacting hadrons would be mistakenly treated as photons. Hence, final states containing n charged hadrons and m photons could be incorrectly reconstructed as having up to as many as m + n photons. These kind of problems will be discussed in Chapter V.

All the alignment and calibration parameters were incorporated into the Monte Carlo model for the experiment. A description of the Monte Carlo, and a critical comparison between it and data for beam $K^+ \to \pi^+\pi^0$ and $K^+ \to \pi^+\pi^+\pi^-$ decays is presented in the following chapter.

CHAPTER V

ANALYSIS OF EXPERIMENTAL DATA

A. Monte Carlo Model of Experiment

In order to obtain absolute cross sections, a thorough understanding of the detection efficiency of the experimental apparatus is required. This entails a detailed knowledge of the geometric acceptance of the spectrometer, its triggering and tracking efficiency, and the efficacy of the LAC in detecting photons. Also, the event reconstruction efficiency, and the effects of the restrictions and cuts applied to the data need to be known. All of these effects were calculated using a Monte Carlo event generator, and a software simulation of the spectrometer.

Events were generated according to certain default distributions, or else were weighted by input distributions in invariant mass, four-momentum transfer, and decay angle. For example, beam K^+ decays were generated according to delta function distributions in mass and in t, and with an isotropic distribution of decay angles in the K^+ rest frame, whereas $K^{*+}(890)$ events were generated according to the input distributions expected for coherent production, and with decay angles in the Gottfried-Jackson frame distributed as $\sin^2\theta\sin^2\phi$, as expected for the decay of coherently produced J = 1 objects. These events were then passed through the software

simulation of the experimental apparatus whereby geometric acceptances and triggering efficiencies were imposed.

The parameters defining the computer simulated incident beam were derived from the true beam. Coherent $K^{*+}(890)$ events were generated randomly along the thickness of the target, while K^+ decay events were generated with a uniform decay distribution in the range from z = -50 inches to +300 inches relative to the target. This distribution exceeded the region occupied by the decay tank to avoid edge effects from finite resolution on the reconstructed decay z-vertex. Multiple scattering of charged particles within the target was taken into account.[61] The orientation of the production plane about the beam trajectory was generated randomly. Secondary decays of π^0's and K_s^0's were generated with isotropic angular distributions in their rest frames. Final-state particles were then traced through the spectrometer, and geometric and triggering constraints imposed. The combination of these two effects can be defined as the geometric acceptance, and determined quantitatively from the ratio of the number of events passing these restrictions to the number originally generated. For $K^{*+}(890)$ events, the geometric acceptance for the final states $K^+\gamma\gamma$ and $\pi^+\pi^+\pi^-$ were 0.56 and 0.52, respectively. This portion of the Monte Carlo model was known as the event generator.

The next step was to mimick the spectrometer by putting appropriate hits in the wire chambers, and depositing energy in the

LAC when called for. Experimentally determined resolutions, efficiencies, and other parameters characterizing the operation of the chambers and the LAC, were used in this process. This computer simulated Monte Carlo data was then "written to tape", and treated just like real data in any further analysis.

The input parameters to the computer simulation of the spectrometer included:

(i) spatial resolutions of the DWC's, as well as their positions, sizes of active areas, and deleterious effects due to the beam

(ii) energy and position resolutions of the LAC for electromagnetic and hadronic showers

(iii) the aperture, length, and position of the BM109, its magnetic field strength, and its effective length

(iv) the presence of the beam hole in the LAC, the size of its sensitive area, and its position

(v) the angular divergence, momentum dispersion, and transverse size of the incident beam

(vi) the positions of the scintillator counters BV, BA, VE and the U and D counters

(vii) the efficiencies of the MBV and TC logic

(viii) the efficiencies and noise rates for the MWPC's and the DWC's

(ix) noise rates for individual LAC channels

(x) the transverse distribution of energy deposited in the LAC by electromagnetically and hadronically induced showers

(xi) the fraction of energy deposited in the back half of the LAC for both types of showers

(xii) the rate of hadronic interaction in the LAC

(xiii) energy thresholds for E_{up}, E_{down}, and E_{tot} (3 GeV, 3 GeV, and 6 GeV, respectively) for use in simulating the LAC γ-logic

(xiv) limitations arising from the fact that each of the drift time digitizer channels had single hit capability.

As a test of the Monte Carlo technique, comparisons were made between Monte Carlo predictions, and real data distributions for various kinematical variables for beam $K^+ \to \pi^+\pi^o \to \pi^+\gamma\gamma$ and $K^+ \to \pi^+\pi^+\pi^-$ decays. For the Monte Carlo simulation of the latter decays, events were generated to uniformly populate the final state phase space. In the comparative analysis, the cuts applied to the Monte Carlo data were identical to those imposed on the real data.

For the $K^+ \to \pi^+\pi^o \to \pi^+\gamma\gamma$ data, events were isolated using the kinematical cuts:

(i) The total reconstructed energy of the event had to be between 194 GeV and 214 GeV.

(ii) The reconstructed two-photon invariant mass had to be in the range 0.110 GeV to 0.160 GeV.

(iii) The energy deposited by the charged particle in the LAC could be no more than 90% of its total energy. This eliminated $K^+ \to e^+\pi^o\nu$ events which survived other cuts.

(iv) The event had to have a reconstructed t of <0.002 GeV^2. The physical events occur at t=0; however, the finite transverse

momentum resolution of the experimental apparatus caused these events to be distributed according to a Gaussian (or very nearly Gaussian) distribution in P_T.

(v) Assuming that the charged particle was a pion, the reconstructed invariant mass had to be in the range 0.450 GeV to 0.550 GeV.

(vi) A cut on the K^+ decay vertex was imposed; the latter was defined as the mid-point of the shortest line segment joining the incident beam track and the π^+ trajectory. The range of this cut was varied, but generally was restricted to be in the decay tank. This will be expanded on later.

Besides these kinematic cuts, other cuts used to select candidate events included:

(i) An initial cut applied to the data to ensure its quality: A possibility existed (at the level of ~1%) that the MWPC information for any given event was associated with hits generated by a beam particle arriving later in time. This resulted from not being able to gate off soon enough subsequent MWPC latching signals. This condition was detected by monitoring the time interval between the last MWPC latching signal and the time for the accepted event trigger. When this time interval was not proper, the events were eliminated from further consideration.

(ii) A requirement that there be one and only one reconstructed incident beam track. At the beam intensities we took data, a small probability existed for there to be more than one beam particle in

an RF "bucket". Rather than try to decide which one of the tracks initiated the event, these events were simply disregarded. More than one beam track could also be produced as a result of spurious signals in the J1 and/or J2 chambers. Again, to avoid confusion as to the correct beam particle trajectory, these events were also eliminated.

(iii) All events were required to be tagged as kaon-induced (K12 signal).

(iv) A requirement that there be a single reconstructed charged track in the final state. This track was also required to have the same charge as the incident K^+.

(v) A requirement that two photons (not including "charged-photon overlaps") be reconstructed in the LAC.

As stated in Section C of Chapter IV, if the median of the energy deposited in the LAC was outside of a 0.75 inch radius of the position of an extrapolated charged-track trajectory to the LAC, this energy was considered to be deposited by a real photon. Consequently, due to the finite spatial resolution of the LAC for hadronic showers, some $K^+ \to \pi^+\pi^0 \to \pi^+\gamma\gamma$ events were reconstructed with three photons in the final state. In order to avoid losing these events (they occurred at a rate of ~3%/charged track), the three invariant masses for pair combinations of photons were calculated, and the pair with a mass closest to the π^0 was retained and used to recalculate total energy, t, and the $\pi^+\pi^0$ mass,

completely ignoring the extraneous "photon". Thus, these events were extracted using all the previously listed cuts, with the exception that there could be three reconstructed photons in the event. This sample was combined with the events found in the two-photon mode. A similar approach was used with the $K^{*+}(890) \to K^+\pi^0 \to K^+\gamma\gamma$ data.

The first three cuts of the "non-kinematic" variety just discussed were also imposed on the $K^+ \to \pi^+\pi^+\pi^-$ candidates. These events were further subjected to the requirement that in the final state there be three reconstructed charged tracks whose total charge was that of the incident K^+. LAC information was not used in the analysis of these events. Additional kinematic cuts included that:

(i) The total reconstructed energy of the three charged particles be between 194 GeV and 214 GeV.

(ii) Due to the poorer P_T resolution in this mode, the reconstructed t had to be < 0.004 GeV^2.

(iii) Assuming the charged particles were all pions, the invariant mass of the event was in the range 0.450 GeV to 0.550 GeV.

(iv) A range for the z-vertices for the K^+ decay that was reasonable. The decay point was defined as the z position that minimized the RMS dispersion of the three charged tracks about the incident beam track. A discussion of the criteria used to cut on z-vertex now follows.

Preliminary Monte Carlo studies of the decay z-vertex resolutions for the $K^+ \to \pi^+\pi^0$ and $K^+ \to \pi^+\pi^+\pi^-$ data gave values for the RMS dispersion of ~8 inches and ~20 inches, respectively. To obtain

an unbiased sample of real K^+ decays for comparison with Monte Carlo predictions (especially for absolute decay rates), a z-vertex cut on $K^+ \to \pi^+\pi^0$ decays from 40 inches to 140 inches from the target was imposed. For the $K^+ \to \pi^+\pi^+\pi^-$ events a cut of 90 - 190 inches was used. These choices were dictated by the following considerations. For the $K^+ \to \pi^+\pi^0$ decay mode, absolute certainty was required that all the decays occurred downstream of the S-counter. Because, had the decay actually occurred upstream of the S-counter, despite having been reconstructed downstream of it (because of resolution), a bias relative to the Monte Carlo data would have been introduced due to the suppression of real events in the target region caused by the conversion of photons from π^0 decay to e^+e^- pairs in the target. Such events would typically be vetoed by the ρ-trigger. Since this effect was not incorporated into the Monte Carlo simulation, a lower cut-off was imposed on the vertex distribution. The upper limit on the z-vertex cut was chosen to avoid decays too close to the PIX MWPC, where modeling of the MBV^2 veto would become overly sensitive to details of π^+ trajectories close to those of the incident K^+. This same sort of argument applied for the choice of the upper cut-off for the $K^+ \to \pi^+\pi^+\pi^-$ decay z-vertex distribution.

The more conservative lower cut-off in the latter mode was chosen to take into account the poor vertex resolution for these events. Again, to avoid biases in comparison to Monte Carlo predictions, it was necessary to assure that these decays occurred

downstream of the S-counter; if they did not, there would be a suppression of real events originating in front of the S-counter, relative to the Monte Carlo rate, because the S-counter requirement of having only one charged particle (i.e. $\overline{S1}$) in the V-trigger was not taken properly into account in the Monte Carlo model.

The above z-vertex cuts are used in the following comparisons of Monte Carlo and real data for K^+ decays. Unless otherwise noted, Monte Carlo data and real data are compared using the lead target.

Figures 27a, and b show, respectively, the histograms of z-vertex distributions for $K^+ \to \pi^+\pi^0$, and $K^+ \to \pi^+\pi^+\pi^-$ decays. The solid curves are Monte Carlo predictions normalized to the numbers of events in the accepted regions of z-vertex (as indicated by the arrows). The reasons for the losses near the target region have already been mentioned. Also, both graphs show a slightly faster fall-off of the Monte Carlo predictions relative to the data. A discussion of this effect, as it applies to the normalization of the observed $K^{*+}(890)$ yields to the observed K^+ decays, will be presented in Section B.

The K^+ decay distributions for total reconstructed energy are presented in Figures 28a and b. The superimposed curves are the Monte Carlo predictions normalized to the number of events between the arrows (194-214 GeV). Because the incident beam momentum had a spread of ~6 GeV/c, the excess widths of these distributions is attributed to the resolution of the spectrometer. There is reasonable agreement between data and Monte Carlo.

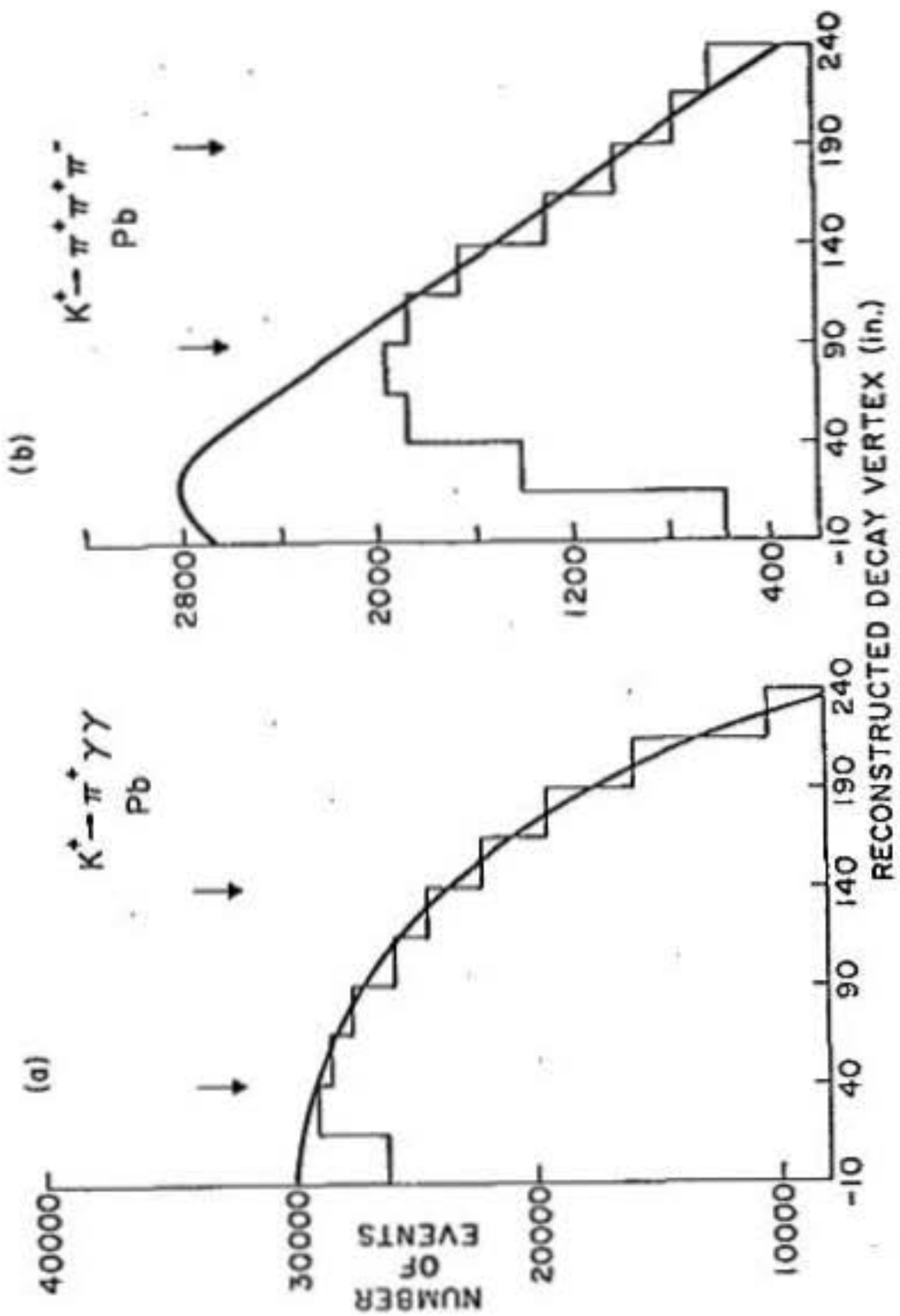

Figure 27

The two-photon mass distribution resulting from π^0 decay and the Monte Carlo prediction have already been presented in Figure 23b. Figure 29a shows the distribution of the energy asymmetry $|E_1 - E_2|/(E_1 + E_2)$ for the two photons from these same decays. Ignoring acceptance and reconstruction efficiencies, this distribution would be flat. The fall-off at high asymmetry (i.e. when the photons from the π^0 decay emerge in the π^0 rest frame close to the flight direction of the π^0) is a result of reconstruction losses when the two photons energies differ substantially and overlap in the LAC. (A low-energy photon lost on the tail of the energy distribution of its more energetic partner.) The loss is ~12% of the total number of events. This corresponds exactly to the fraction of $K^+ \to \pi^+\pi^0$ events reconstructed, where only one photon is required in the final state (the missing low energy photon does not adversely affect calculations of total energy, t, or invariant mass). The Monte Carlo prediction is given by the solid curve, and is normalized to the total number of events. Again, the agreement is good.

Figure 29b shows the distribution of the cosine of the polar decay angle of the π^+ from $K^+ \to \pi^+\pi^0$ decays in the helicity frame of the K^+. The superimposed curve is the Monte Carlo result normalized to the total number of events. Since $K^+ \to \pi^+\pi^0$ decays are isotropic in the helicity frame, the loss of events as $\cos\theta_{HEL}$

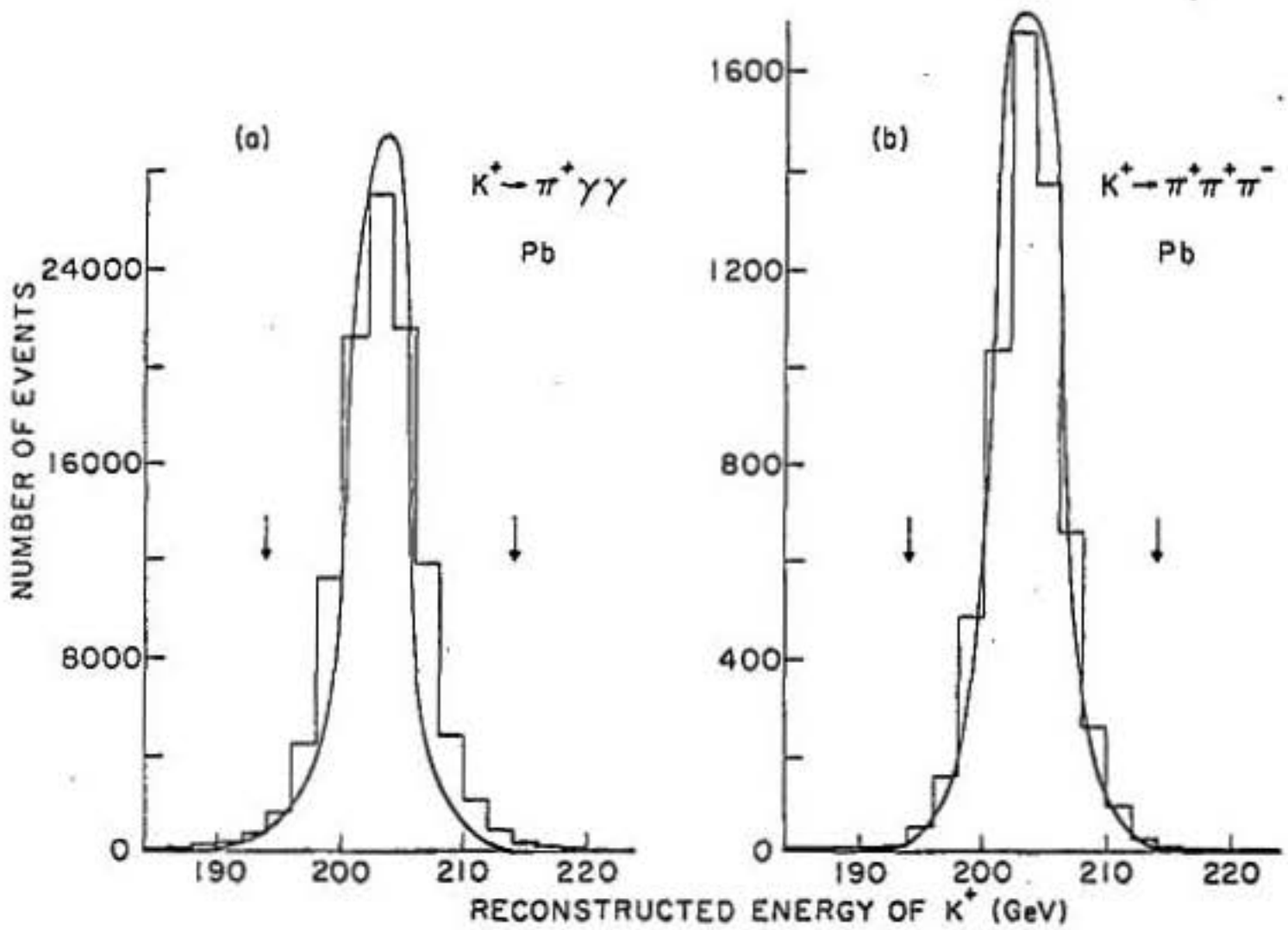

Figure 28

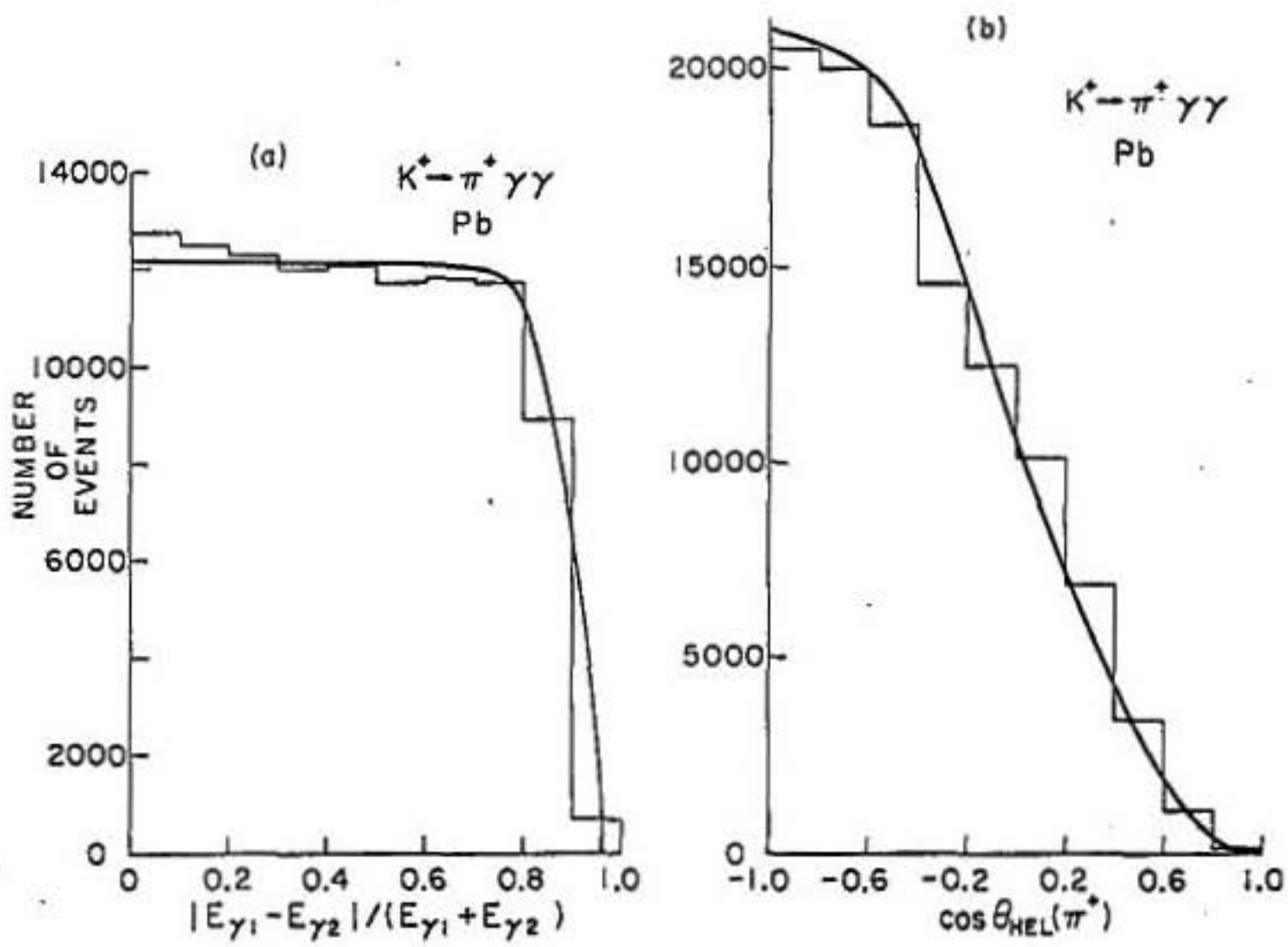

Figure 29

increases (i.e. as the π^+ direction in the rest frame of the K^+ becomes close to the flight direction of the K^+ in the laboratory) is explained by the losses of these events due to the triggering of the XBV^2 veto by the outgoing π^+. As these π^+'s approach the kinematical limit in the momentum, they are also vetoed by the VE counter. Since the π^0's in this regime are of low momentum, there are additional losses when the decay photons hit the AX counters, or when the LAC energy does not exceed the E_{tot} threshold value in the LAC γ-logic. The agreement between the data and Monte Carlo is good.

Figures 30a and 30b show the reconstructed invariant mass for candidate $K^+ \to \pi^+\pi^0$ and $K^+ \to \pi^+\pi^+\pi^-$ events, respectively. The Monte Carlo expectation is given by the solid curves, which are normalized to the number of events between the arrows (i.e. between 0.450 GeV and 0.550 GeV). The data indicate RMS widths or resolutions of ∿8 MeV and ∿7 MeV for the $\pi^+\gamma\gamma$ and $\pi^+\pi^+\pi^-$ invariant masses, respectively. The Monte Carlo predictions are in good agreement with the data. It is interesting to note that the Monte Carlo result for $\pi^+\pi^+\pi^-$ invariant mass peaks at a somewhat larger value than expected for the data. In fact, studies have shown that the reconstructed K^+ mass for this decay mode increases, from its nominal value in the target region, as the range of the z-vertex cut is set further downstream from the target (≈3% increase at z = 215 inches). In this regard, the Monte Carlo result tracks the data extremely well.

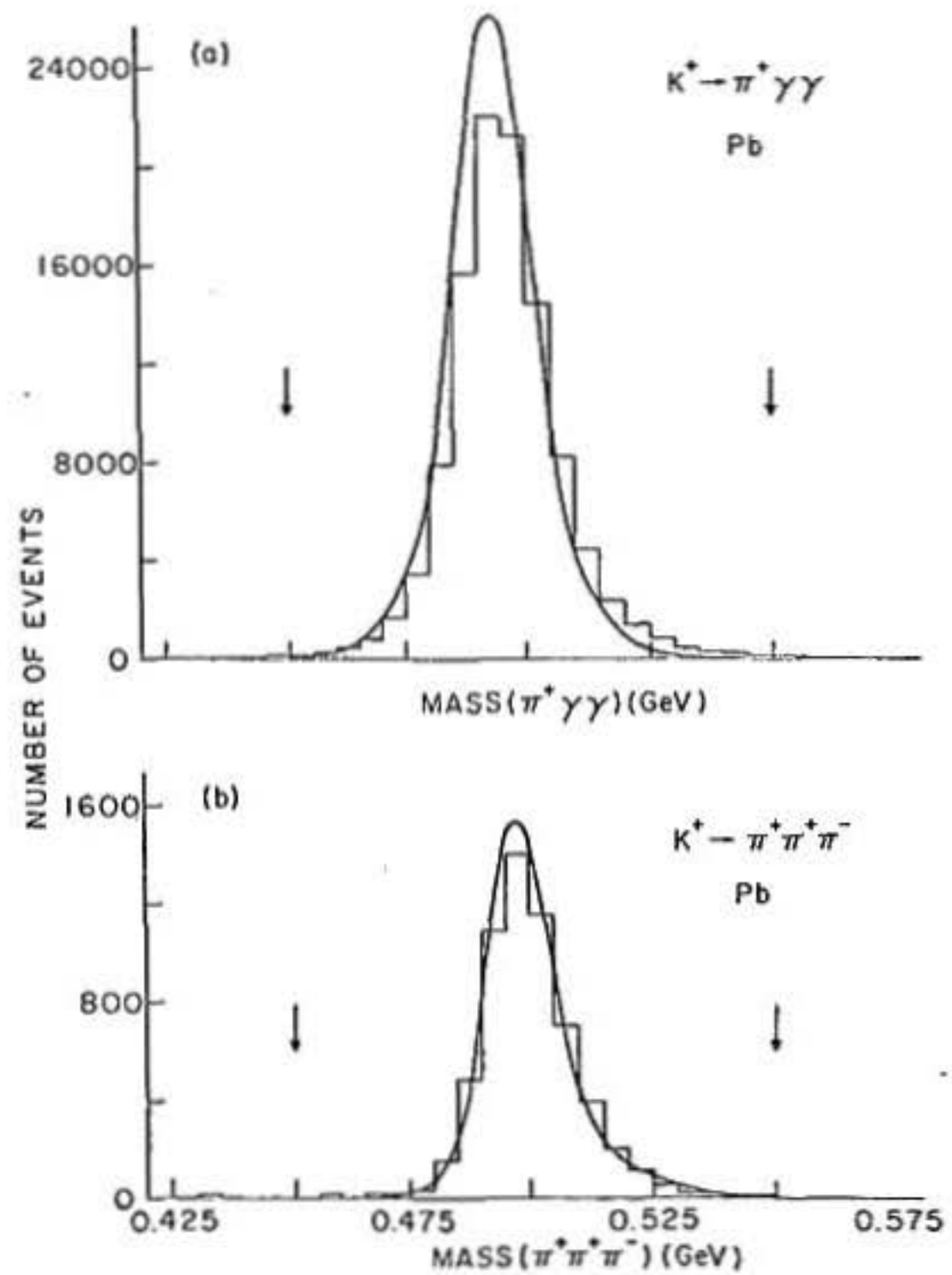

Figure 30

Figures 31a, 31b and 31c show a comparison of the t-distributions for $K^+ \to \pi^+\pi^0$ and $K^+ \to \pi^+\pi^+\pi^-$ on the empty, copper, and lead targets, respectively. The solid lines are the Monte Carlo predictions normalized to the number of events with $t < 0.001\ GeV^2$. As already noted, the Monte Carlo contained corrections for multiple Coulomb scattering of charged tracks within the target. Nevertheless, these graphs indicate that the Monte Carlo slightly underestimates the actual P_T resolution of the experimental apparatus.

Assuming that the P_T resolution function $R(\vec{P}_T, \vec{\tilde{P}}_T)$ can be parameterized by a Gaussian distribution

$$R(\vec{P}_T, \vec{\tilde{P}}_T) = \frac{1}{2\pi\sigma_{P_T}} e^{-(\vec{P}_T - \vec{\tilde{P}}_T)^2/2\sigma_{P_T}^2} \qquad (19)$$

which gives the probability of measuring a transverse momentum $\vec{P}_T$ for an event when its true value was $\vec{\tilde{P}}_T$, we would expect the t-distribution for K^+ decays to have the form expected for resolution smearing of decays at t = 0:

$$\frac{1}{N_o}\frac{dN}{dt} = \int d\vec{\tilde{P}}_T\, R(\vec{P}_T, \vec{\tilde{P}}_T)\,\delta^{(2)}(\vec{P}_T) \propto e^{-t/2\sigma_{P_T}^2}$$

Both the data and Monte Carlo distributions support this assumption, as indicated by the exponential forms of these distributions. In

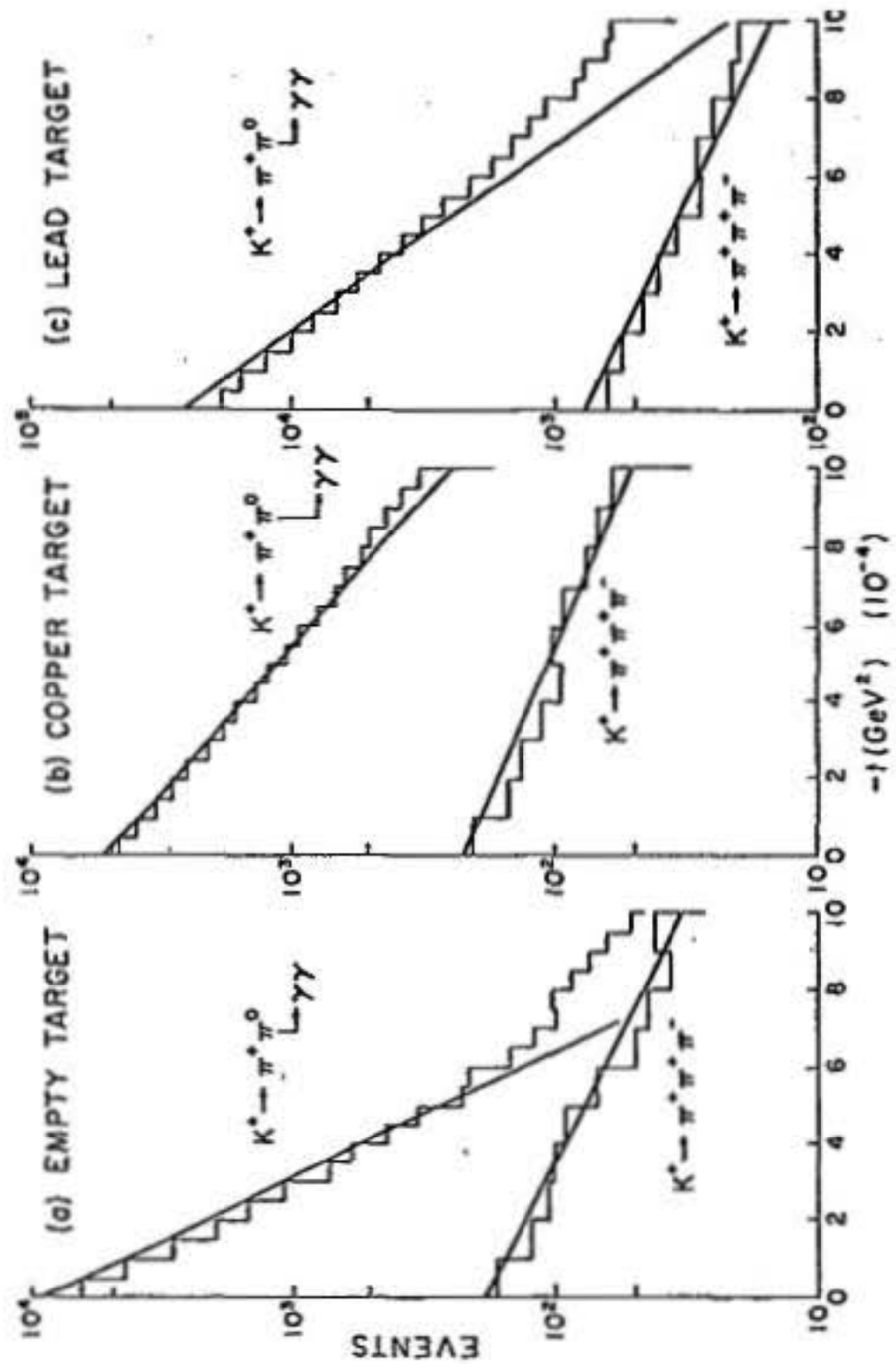

Figure 31

principle, the total variance in P_T, $\sigma^2_{P_T}$, should contain all contributions to the inherent spectrometer resolution, which includes effects of multiple Coulomb scattering of charged tracks in the spectrometer and in the target. However, the Monte Carlo simulation of the spectrometer did not include multiple Coulomb scattering other than in the target, since it was cumbersome to introduce these relatively small effects over an extended region. This explains some of the discrepancy between the Monte Carlo and the data in Figure 31: there was 1.52×10^{-2} radiation lengths of material in J1, J2, and various beam counters upstream of the target and 4.33×10^{-2} radiation lengths of material between the target and the magnet; the sum of these two contributions corresponds to a significant fraction of the number of radiation lengths in the targets.

Another effect that was found in fitting $K^+ \to \pi^+\pi^0$ t-disbributions was that the extracted values for σ_{P_T} depended on the cut-off used for the decay z-vertex. The same effect appeared in the Monte Carlo (see Figures 32a and 32b). In order to gain some insight into the P_T resolution for $K^{*+}(890)$ events (decaying to the topologically similar final state $K^+\pi^0 \to K^+\gamma\gamma$), the P_T resolution for $K^+ \to \pi^+\pi^0 \to \pi^+\gamma\gamma$ events was examined further.

A fit was performed on the values of σ_{P_T} for $K^+ \to \pi^+\pi^0$ decays, as a function of z-vertex, for all targets for both real and Monte Carlo data. The fit assumed a linear dependence of σ_{P_T} on decay

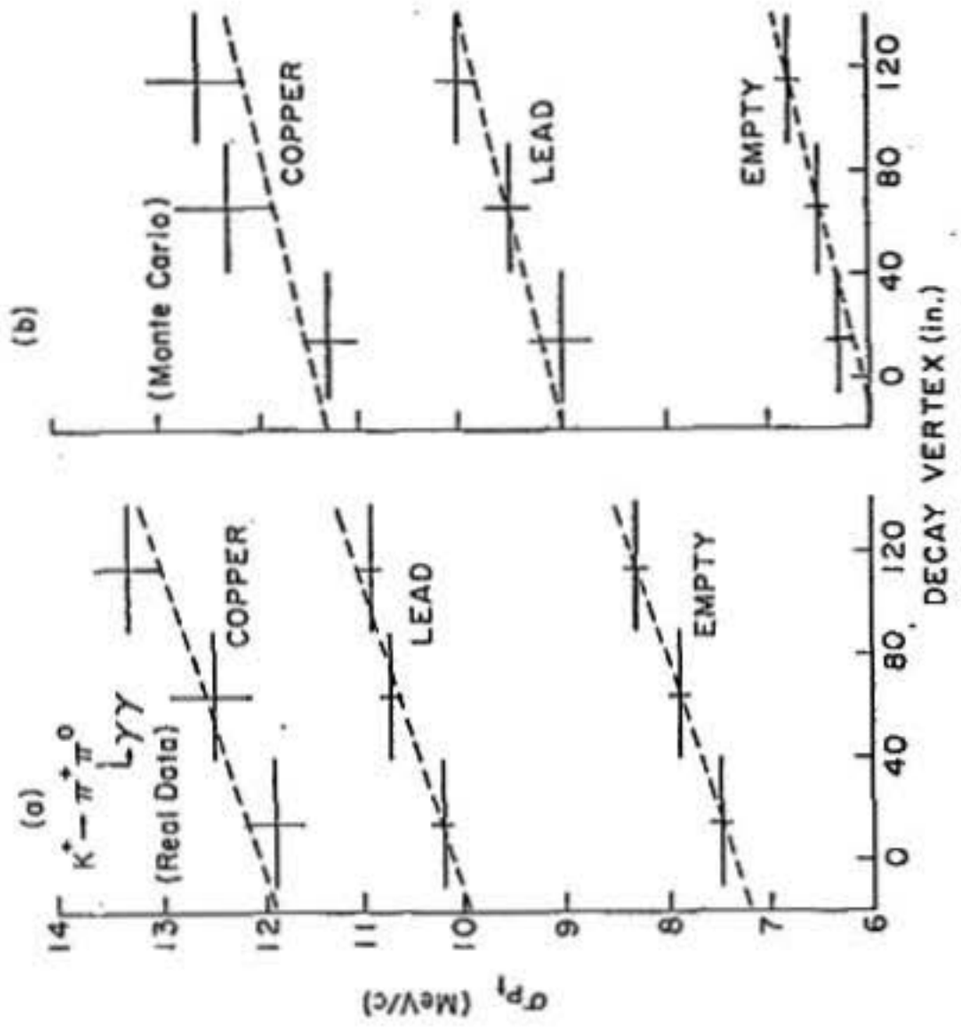

Figure 32

z-vertex, and took the form $\sigma_i = \sqrt{\sigma_o^2 + \sigma_{c_i}^2} + az$ where i labels the target type, σ_o is the contribution to σ_{P_T} inherent to the spectrometer, σ_{c_i} is the contribution from multiple scattering in the ith target, z is the decay z-vertex and a, assumed to be independent of target material, was a parameter. The fitted results for the data, and for the Monte Carlo are shown by the dotted lines in Figures 32a, and 32b, respectively. The final values of σ_{c_i} obtained for data and for the Monte Carlo events agreed to within statistical error, and were close to the values expected from the contributions to multiple Coulomb scattering. The values determined for a also agreed to within statistical error, however, the fitted values for σ_o did not agree.

Thus, it was apparent that σ_{P_T} and its dependence on z-vertex, as extracted from the Monte Carlo, was consistent with that extracted from the data, up to an overall offset. At the target, this could be expressed as

$$\sigma^2_{P_T}(\text{real data}) = \sigma^2_{P_T}(\text{Monte Carlo}) + \Delta^2$$

where $\Delta = 4.2$ MeV/c could be attributed to the contribution to σ_{P_T} due to multiple Coulomb scattering in the spectrometer, that was not explicitly put into the Monte Carlo. This contribution was taken into account when calculating σ_{P_T} for the $K^{*+}(890)$.

B. Normalization

To extract the partial width $\Gamma(K^{*+}(890) \to K^+\gamma)$ from the measured $K^{*+}(890)$ t' distributions, the latter had to be first converted to absolute cross sections. Corrections not addressed in the Monte Carlo model, and essentially independent of kinematics included:

Corrections to the gated beam flux incident on each target and

Additional spectrometer related corrections.

Each of these additional corrections will be described below; an important correction, applied to the observed yield of $K^{*+}(890)$ events, based on the observed yield of beam K^+ decays into topologically similar final states, extrapolated to the target region, will also be explored. Further corrections to the $K^{*+}(890)$ data resulting from spectrometer acceptances, triggering efficiencies, reconstruction efficiencies, the effects of cuts applied to the data, decay branching ratios, and empty target subtractions will be discussed in Section C. Possible sources of background to the $K^{*+}(890)$ signal will also be discussed there.

I. Corrections to the gated kaon beam flux included:

(i) A correction for beam kaons that subsequently decayed upstream of the target to a single charged particle (and neutrals) which still satisfied the beam definition. This correction was obtained from the Monte Carlo by generating K^+ decays to $\mu^+\nu$, $\pi^+\pi^o$, $\pi^+\pi^o\pi^o$, $\mu^+\pi^o\nu$, and $e^+\pi^o\nu$; starting half-way through the K1 Cherenkov counter (to make certain that the particle could be tagged), the kaon was allowed to decay according to an exponential decay

distribution in mean laboratory flight length; the decay was weighted by the corresponding branching ratio, and then checked to see that the event still satisfied the beam scintillator counter requirements. This correction is called "Cherenkov contamination #1".

(ii) A correction for the pion contamination of the K12 kaon Cherenkov signal. This correction was calculated from data for the two final state topologies $K^+\gamma\gamma$ and $\pi^+\pi^+\pi^-$ for the $K^{*+}(890)$, and $\pi^+\gamma\gamma$ and $\pi^+\pi^+\pi^-$ for K^+ decays. The K^+ decay rates over the appropriate z-vertex ranges were measured for kaons tagged using both the K12 and K13 Cherenkov signals. The latter was an absolutely pure kaon signal. The ratio of the measured decay rates found in the K13 mode to that in the K12 mode provided the correction for pion contamination ("Cherenkov contamination #2").

(iii) A correction for the restriction imposed on the data that there be one and only one beam track. This correction was calculated for each target using the correction observed for random beam triggers.

(iv) A correction for the absorption of the incident K^+ upstream of the target. The material upstream of the target, not including the J1 or J2 chambers, or material in between, amounted to 6.1×10^{-4} proton absorption lengths. The material in the incident beam spectrometer was ignored because an interaction in it would either cause the BH veto to fire, or more than one beam track would be reconstructed.

II. Target-related corrections included:

(i) A correction for the absorption of the incident K^+ beam in the target. This correction was given by $e^{\ell/2L_{abs}(K^+)}$ for $K^{*+}(890)$ events and $e^{\ell/L_{abs}(K^+)}$ for K^+ decays. Here ℓ is the thickness of the target, and $L_{abs}(K^+)$ is the K^+ absorption length in the target material at 200 GeV/c.[51,62]

(ii) A target veto correction, which included the effects of vetoes from δ-rays and random firings of veto counters. This correction was calculated from the observed rates in the V1-4 counters for the random beam-trigger events.

(iii) A correction for the absorption of the final state particles in the target. This included conversions of photons from π^o decay to e^+e^- pairs. For the K^o_s final state, it was assumed that its absorption cross section was equal to that for K^+'s. For the conversion of π^o photons, the correction factor was obtained by integrating the square of the attenuation factor $e^{-7/9\, x/L_o}$ over the target thickness, where x is the distance the two photons travel through the target, and L_o is the radiation length of the target material.[50] This gave a correction factor for a π^o (conversion of either photon) for a target of thickness ℓ, of $(14/9)(\ell/L_o)/(1 - e^{-(14/9)(\ell/L_o)})$.

III. The spectrometer-related corrections included:

(i) A correction for the loss of good events due to poor quality MWPC data. This effect was described in Section A of this chapter and was quantified for each target by observing the

corresponding rate of loss for random-beam trigger events.

(ii) A correction for the efficiency of the S-counter, whose signal was required by both the ρ and V-triggers, but not by the random-beam trigger. This correction was calculated utilizing data obtained with random-beam trigger events.

(iii) A correction for the loss of events in the ρ and V-triggers resulting from discrimination of the S-counter pulse height. This correction was, again, calculated using random-beam trigger events to establish an unbiased spectrum for the S-counter pulse height distribution, and then comparing this to the pulse height spectra for ρ and V-trigger events. Clean events for the latter trigger modes were obtained from beam $K^+ \to \pi^+\pi^0$ and $K^+ \to \pi^+\pi^+\pi^-$ decays. For this study, the only random-beam events used were those for which there was only one beam track, and no target or downstream vetoes. Figure 33 shows the pulse height spectrum for these random-beam triggers, and that for V-triggers (clean $K^+ \to \pi^+\pi^+\pi^-$ events), normalized to the number of random-beam events between the arrows. The cross-hatched regions show the loss of V-trigger events in the Landau tail region of the distribution due to the $\overline{S1}$ requirement, and a smaller loss for small pulse height events due to the S0 requirement.

(iv) A correction for absorption of the final-state particles in the S-counter, calculated as in the target-related correction (iii); there were 4.6×10^{-3} radiation lengths, and 2.8×10^{-3} proton absorption lengths, of material in the S-counter.

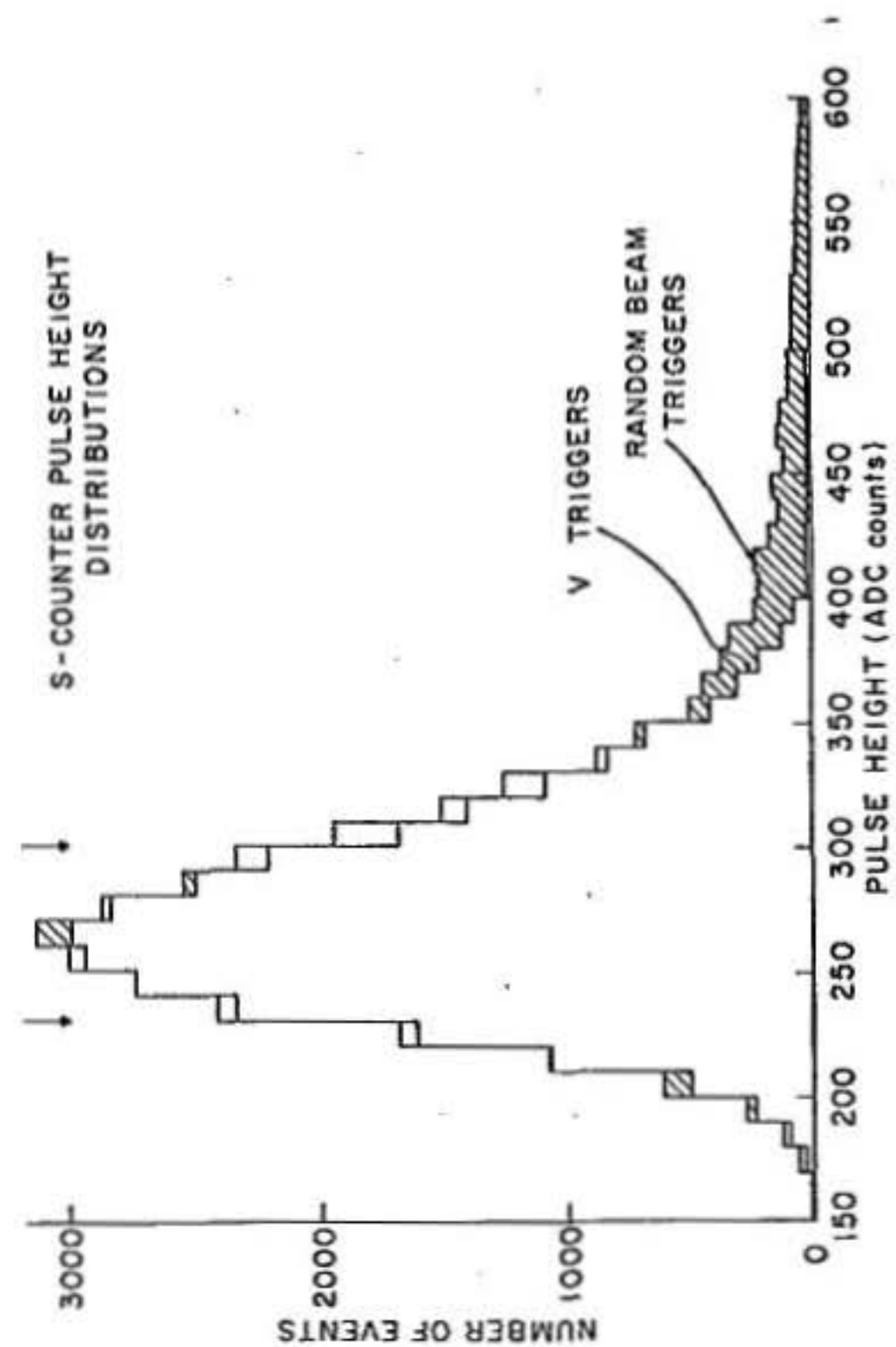

Figure 33

(v) A correction for the vetoing of good events by the AO and H counters due to δ-rays, random firings, and/or a misalignment of the H counter during part of the running period. This correction was determined by examining the rate of firing of these counters for random-beam events.

(vi) A correction for the vetoing of good events by the A1, A2, and AM veto counters as a result of random firings, or δ-rays generated in the upstream MWPC's or DWC's. This correction was calculated in a manner similar to correction (v), and then multiplied by the number of charged particles in the final state.

(vii) A correction for the absorption of final-state particles in the spectrometer. This included conversion of photons from π^0 decay to $e^+ e^-$ pairs. The contributions from spectrometer elements (such as the BV, BA, and VE counters), whose effects varied with final-state topology, were determined using the Monte Carlo program. (The amount of material in the spectrometer ranged from 0.073 to 0.075 radiation lengths, and from 0.022 to 0.026 proton absorption lengths, depending on the type of event.)

(viii) A correction for the decay of final-state particle within the spectrometer. Corrections for each final state were established with the help of the Monte Carlo program. Final state pions and kaons were allowed to decay along their flight paths and events in which these particles decayed within the confines of the spectrometer were assumed to have been lost.

The numerical values for the correction factors associated with all the above effects are tabulated in Tables VI.A through VI.D for $K^+ \to \pi^+\pi^0 \to \pi^+\gamma\gamma$, $K^+ \to \pi^+\pi^+\pi^-$, $K^{*+}(890) \to K^+\pi^0 \to K^+\gamma\gamma$, and $K^{*+}(890) \to K^0_s\pi^+ \to \pi^+\pi^+\pi^-$ events.

The final concern of this section is a discussion of the normalization of the $K^{*+}(890)$ yield to that observed from beam K^+ decays. If the observed yield of beam K^+ decays differed from Monte Carlo expectations, we would expect that the $K^{*+}(890)$ yield in topologically similar decay channels would be similarly reduced. The most likely causes for such discrepancies could be attributed to either imperfect modeling of the experimental apparatus in the Monte Carlo, or to some unknown effect afflicting the apparatus. Presumably, the beam K^+ decay and $K^{*+}(890)$ production yields would be similarly affected and any such limitations would tend to cancel out in a relative normalization of yields to K^+ decays.

Figure 34a shows the raw beam $K^+ \to \pi^+\pi^0$ decay rate (i.e. the number of observed events selected through cuts given in Section A, divided by the gated kaon beam flux); the results are for the decay z-vertex range of 25 to 225 inches, plotted as a function of temporal running period. Figure 34b shows these same rates corrected for S-counter efficiency and random vetos on a run-by-run basis. The relative constancy of the corrected rates over the entire run is indicative of the stability of the equipment, and supports the claim that normalization of the observed $K^{*+}(890)$ yield on each

TABLE VI.A

Beam Flux, Target Related, and Spectrometer Related Corrections for the Decay

$K^+ \to \pi^+\gamma\gamma$

		Target		
		Empty	Copper	Lead
Beam flux corrections				
1. Cherenkov contamination #1		1.004 ± 0.000	1.004 ± 0.000	1.004 ± 0.000
2. Cherenkov contamination #2		1.018 ± 0.012	1.020 ± 0.008	1.020 ± 0.005
3. Correction for one beam track		1.048 ± 0.003	1.056 ± 0.002	1.050 ± 0.001
4. Correction for absorption of incident K^+ upstream of target		1.000 ± 0.000	1.000 ± 0.000	1.000 ± 0.000
Target related corrections				
1. Absorption of incident K^+ in target		—	1.033 ± 0.000	1.005 ± 0.000
2. Correction for target vetoes		1.016 ± 0.001	1.098 ± 0.003	1.046 ± 0.001
3. Correction for absorption of final state in target		—	—	—
Spectrometer related corrections				
1. Correction for loss of good data		1.018 ± 0.002	1.022 ± 0.001	1.023 ± 0.001
2. Correction for S-counter efficiency		1.007 ± 0.001	1.000 ± 0.000	1.006 ± 0.000
3. Correction for S-counter pulse height discrimination		1.013 ± 0.001	1.000 ± 0.000	1.004 ± 0.000
4. Correction for absorption of final state in S-counter	(K^+)	1.002 ± 0.000	1.002 ± 0.000	1.002 ± 0.000
5. Correction factor for AO + H vetoes		1.126 ± 0.005	1.107 ± 0.003	1.145 ± 0.003
6. Correction factor for A1, A2, AM vetoes		1.010 ± 0.001	1.013 ± 0.001	1.013 ± 0.001
7. Correction for absorption of final state in spectrometer	(π^+)	1.020 ± 0.001	1.020 ± 0.001	1.020 ± 0.001
	(γ)	1.060 ± 0.002	1.060 ± 0.002	1.060 ± 0.002
	(γ)	1.060 ± 0.002	1.060 ± 0.002	1.060 ± 0.002
8. Correction for decay of final state in spectrometer	(π^+)	1.004 ± 0.000	1.004 ± 0.000	1.004 ± 0.000

TABLE VI.B

Beam Flux, Target Related, and Spectrometer Related Corrections for the Decay

$K^+ \to \pi^+\pi^+\pi^-$

		Target		
		Empty	Copper	Lead
Beam flux corrections				
1. Cherenkov contamination #1		1.004 ± 0.000	1.004 ± 0.000	1.004 ± 0.000
2. Cherenkov contamination #2		1.012 ± 0.043	0.968 ± 0.034	1.015 ± 0.020
3. Correction for one beam track		1.048 ± 0.003	1.056 ± 0.002	1.050 ± 0.001
4. Correction for absorption of incident K^+ upstream of target		1.000 ± 0.000	1.000 ± 0.000	1.000 ± 0.000
Target related corrections				
1. Absorption of incident K^+ in target		—	1.033 ± 0.000	1.005 ± 0.000
2. Correction for target vetoes		1.016 ± 0.001	1.098 ± 0.003	1.046 ± 0.001
3. Correction for absorption of final state in target		—	—	—
Spectrometer related corrections				
1. Correction for loss of good data		1.018 ± 0.002	1.022 ± 0.001	1.023 ± 0.001
2. Correction for S-counter efficiency		1.007 ± 0.001	1.000 ± 0.000	1.006 ± 0.000
3. Correction for S-counter pulse height discrimination		1.089 ± 0.010	1.111 ± 0.012	1.076 ± 0.008
4. Correction for absorption of final state in S-counter	(K^+)	1.002 ± 0.000	1.002 ± 0.000	1.002 ± 0.000
5. Correction factor for AO + H vetoes		1.125 ± 0.005	1.107 ± 0.003	1.145 ± 0.003
6. Correction factor for A1, A2, AM vetoes		1.031 ± 0.002	1.039 ± 0.002	1.038 ± 0.001
7. Correction for absorption of final state in spectrometer	(π^+)	1.018 ± 0.001	1.018 ± 0.001	1.018 ± 0.001
	(π^+)	1.018 ± 0.001	1.018 ± 0.001	1.018 ± 0.001
	(π^-)	1.018 ± 0.001	1.018 ± 0.001	1.018 ± 0.001
8. Correction for decay of final state in spectrometer	(3π)	1.007 ± 0.001	1.007 ± 0.001	1.007 ± 0.001

TABLE VI.C

Beam Flux, Target Related, and Spectrometer Related Corrections for the $K^{*+}(890) \rightarrow K^+\gamma\gamma$ Data

		Target		
		Empty	Copper	Lead
Beam flux corrections				
1. Cherenkov contamination #1		1.004 ± 0.000	1.004 ± 0.000	1.004 ± 0.000
2. Cherenkov contamination #2		1.018 ± 0.012	1.020 ± 0.008	1.020 ± 0.005
3. Correction for one beam track		1.048 ± 0.003	1.056 ± 0.002	1.050 ± 0.001
4. Correction for absorption of incident K^+ upstream of target		1.000 ± 0.000	1.000 ± 0.000	1.000 ± 0.000
Target related corrections				
1. Absorption of incident K^+ in target		——	1.016 ± 0.000	1.003 ± 0.000
2. Correction for target vetoes		1.016 ± 0.001	1.098 ± 0.003	1.046 ± 0.001
3. Correction for absorption of final state in target	(K^+)	——	1.014 ± 0.000	1.002 ± 0.000
	(2γ)	——	1.382 ± 0.003	1.178 ± 0.003
Spectrometer related corrections				
1. Correction for loss of good data		1.018 ± 0.002	1.022 ± 0.001	1.023 ± 0.001
2. Correction for S-counter efficiency		1.007 ± 0.001	1.000 ± 0.000	1.006 ± 0.000
3. Correction for S-counter pulse height discrimination		1.013 ± 0.001	1.000 ± 0.000	1.004 ± 0.000
4. Correction for absorption of final state in S-counter	(K^+)	1.002 ± 0.000	1.002 ± 0.000	1.002 ± 0.000
	(γ)	1.004 ± 0.000	1.004 ± 0.000	1.004 ± 0.000
	(γ)	1.004 ± 0.000	1.004 ± 0.000	1.004 ± 0.000
5. Correction factor for AO + H vetoes		1.126 ± 0.005	1.107 ± 0.003	1.145 ± 0.003
6. Correction factor for A1, A2, AM vetoes		1.010 ± 0.001	1.013 ± 0.001	1.013 ± 0.001
7. Correction for absorption of final state in spectrometer	(K^+)	1.017 ± 0.001	1.017 ± 0.001	1.017 ± 0.001
	(γ)	1.059 ± 0.002	1.059 ± 0.002	1.059 ± 0.002
	(γ)	1.059 ± 0.002	1.059 ± 0.002	1.059 ± 0.002
8. Correction for decay of final state in spectrometer	(K^+)	1.010 ± 0.001	1.010 ± 0.001	1.010 ± 0.001

Table VI.D

Beam Flux, Target Related, and Spectrometer Related Corrections for the $K^{*+}(890) \rightarrow \pi^+\pi^+\pi^-$ Data

		Target		
		Empty	Copper	Lead
Beam flux corrections				
1. Cherenkov contamination #1		1.004 ± 0.000	1.004 ± 0.000	1.004 ± 0.000
2. Cherenkov contamination #2		1.012 ± 0.043	0.968 ± 0.034	1.015 ± 0.020
3. Correction for one beam track		1.048 ± 0.003	1.056 ± 0.002	1.050 ± 0.001
4. Correction for absorption of incident K^+ upstream of target		1.000 ± 0.000	1.000 ± 0.000	1.000 ± 0.000
Target related corrections				
1. Absorption of incident K^+ in target		——	1.016 ± 0.000	1.003 ± 0.000
2. Correction for target vetoes		1.016 ± 0.001	1.098 ± 0.003	1.046 ± 0.001
3. Correction for absorption of final state in target	(K_S^0)	——	1.014 ± 0.000	1.002 ± 0.000
	(π^+)	——	1.017 ± 0.000	1.003 ± 0.000
Spectrometer related corrections				
1. Correction for loss of good data		1.018 ± 0.002	1.022 ± 0.001	1.023 ± 0.001
2. Correction for S-counter efficiency		1.007 ± 0.001	1.000 ± 0.000	1.006 ± 0.000
3. Correction for S-counter pulse height discrimination		1.089 ± 0.010	1.111 ± 0.012	1.076 ± 0.008
4. Correction for absorption of final state in S-counter	(K_S^0)	1.002 ± 0.000	1.002 ± 0.000	1.002 ± 0.000
	(π^+)	1.002 ± 0.000	1.002 ± 0.000	1.002 ± 0.000
5. Correction factor for AO + H vetoes		1.126 ± 0.005	1.107 ± 0.003	1.145 ± 0.003
6. Correction factor for A1, A2, AM vetoes		1.031 ± 0.002	1.039 ± 0.002	1.038 ± 0.001
7. Correction for absorption of final state in spectrometer	(π^+)	1.016 ± 0.001	1.016 ± 0.001	1.016 ± 0.001
	(π^+)	1.017 ± 0.001	1.017 ± 0.001	1.017 ± 0.001
	(π^-)	1.017 ± 0.001	1.017 ± 0.001	1.017 ± 0.001
8. Correction for decay of final state in spectrometer	(3π)	1.007 ± 0.001	1.007 ± 0.001	1.007 ± 0.001

target over the whole running period to the corresponding yield for topologically similar beam K^+ decays is not compromised by contamination from data of suspect quality.

The calculation of these normalization factors entailed forming the ratio of the expected K^+ decay yield, determined from the Monte Carlo, to the fully corrected observed yield. The expected yield was calculated from the well established life-time and branching ratios of the K^+.[51]

A comparison between data and Monte Carlo K^+ decays indicated that this ratio was a function of the position of the decay vertex. This discrepancy is in addition to the large differences already noted between the Monte Carlo and the data distributions for the decay z-vertex near the target (see Figure 27). (Here we are referring to the somewhat more rapid fall-off in the Monte Carlo relative to data at larger z-vertex values.) Because for the $K^{*+}(890)$ the normalization to the K^+ decays was required at the position of the target, the normalization correction factor for K^+ decays in the decay tank was extrapolated to the target. These corrections were obtained for each of the K^+ decay modes (i.e. $\pi^+\pi^0$ and $\pi^+\pi^+\pi^-$) and for each of the targets (i.e. empty, copper, and lead) for correcting the topologically similar sets of $K^{*+}(890)$ data.

The method used for obtaining these factors is illustrated in Figures 35a, and 35b for the decays $K^+ \to \pi^+\pi^0$, and $K^+ \to \pi^+\pi^+\pi^-$,

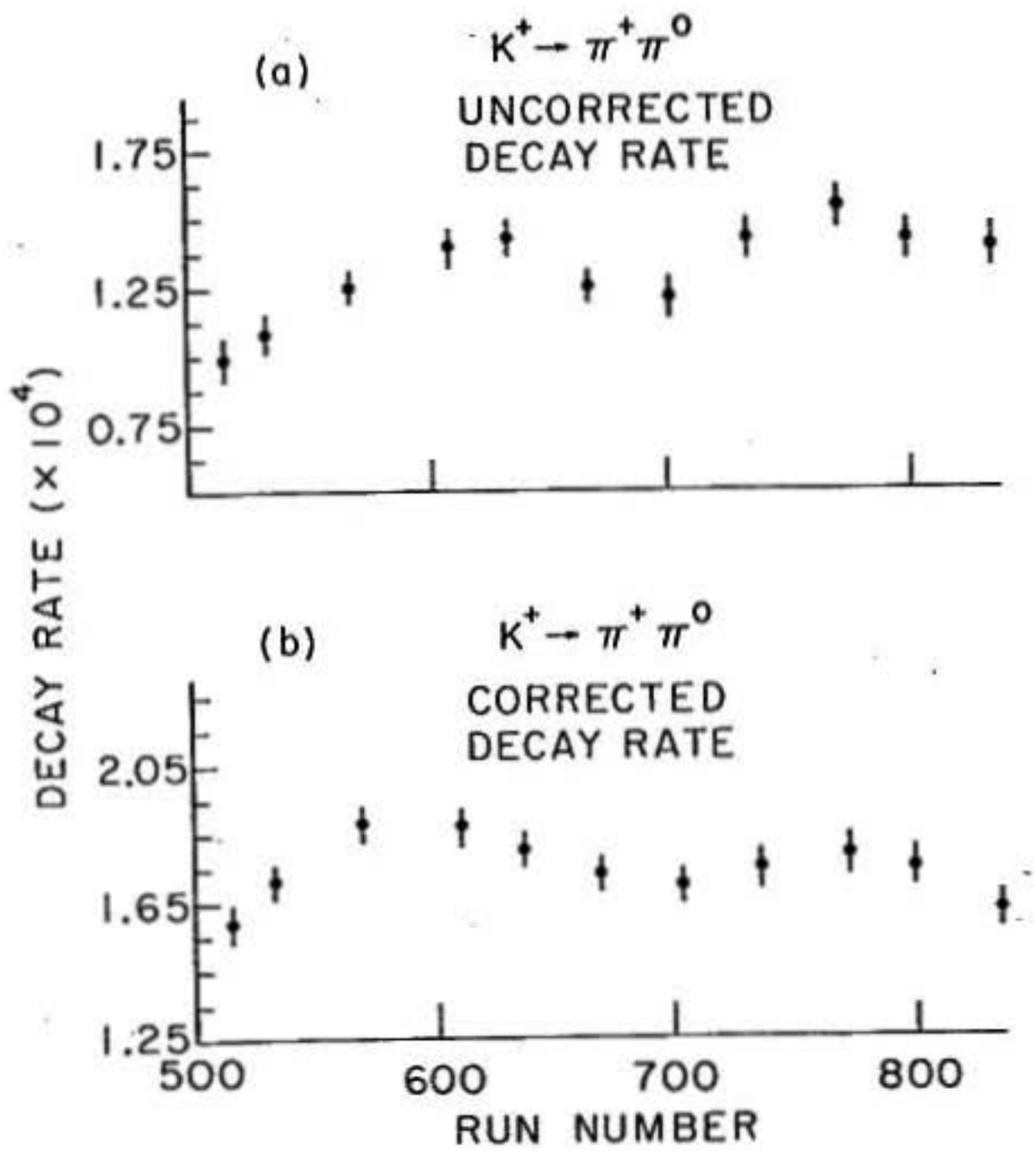

Figure 34

respectively. The ratio of expected to observed K^+ decay rates was calculated over 50-inch ranges of decay z-vertex between 40 and 190 inches, and 90 to 190 inches, for the $K^+ \to \pi^+\pi^0$, and $K^+ \to \pi^+\pi^+\pi^-$ data, respectively. Because of poor statistics, and the bias in the ratio outside of the chosen range, the $K^+ \to \pi^+\pi^+\pi^-$ ratios were obtained for only two points. The resulting normalization factors were then fit with a linear dependence on decay z-vertex for each target. The results are indicated by the dotted lines in Figures 35a and 35b. An extrapolation of these fitted forms to the target position then gave the corrections to be applied to the $K^{*+}(890)$ yield for normalization to K^+ decays. These corrections are given in Tables VII.A and VII.B, along with all the previously derived corrections.

C. Determination of Absolute Cross Sections

The overall acceptance for $K^{*+}(890)$ events was calculated using Monte Carlo generated events which were subjected to the same reconstruction and analysis procedures as the experimental data. From this point on, overall acceptances will be defined as the convolution of geometric acceptances, triggering efficiencies, reconstruction efficiencies, and will include the effects of all cuts applied to the data. These restrictions included the following non-kinematical cuts already described for K^+ decays:

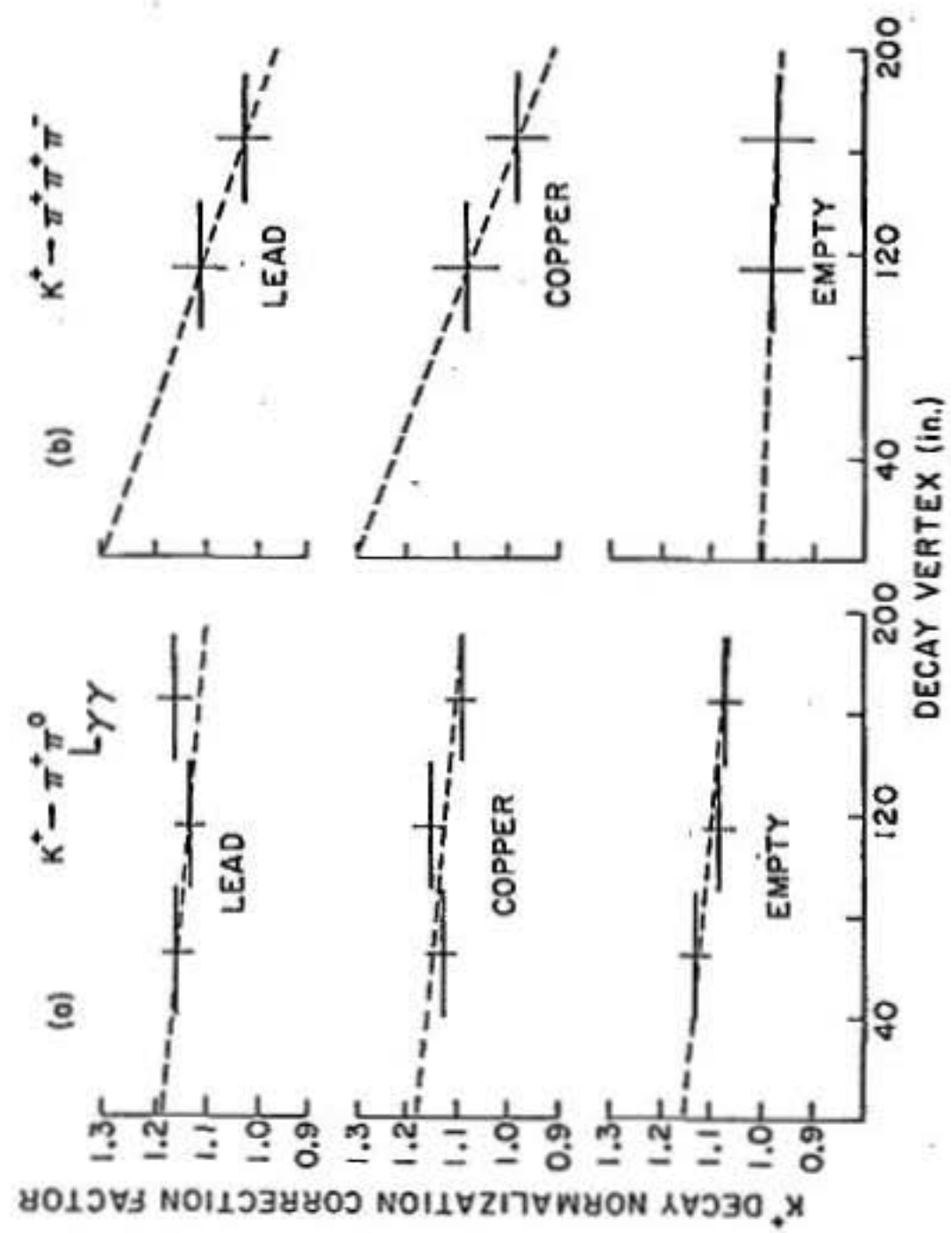

Figure 35

(i) A cut to ensure the quality of the MWPC information

(ii) The requirement of a single reconstructed incident beam particle and

(iii) The requirement that the beam particle be tagged as a kaon by the K12 Cherenkov counter.

Further cuts imposed on candidate $K^{*+}(890)$ events in the $K^+\gamma\gamma$ or $\pi^+\pi^+\pi^-$ final state required:

(iv) One charged particle and two photons (or three charged particles for the $\pi^+\pi^+\pi^-$ mode) with total charge identical to that of the incident K^+.

The following kinematical cuts were also applied to the $K^+\gamma\gamma$ data:

(i) The total reconstructed energy of the event had to be in the range 194 GeV to 214 GeV.

(ii) The reconstructed -t' was required to be less than 0.004 GeV^2 (to enhance coherent events produced predominantly by Primakoff excitation).

(iii) The reconstructed two-photon mass was limited to the range 0.110 GeV to 0.160 GeV.

(iv) The energy deposited in the LAC by the charged particle could be no more than 90% of its total energy.

(v) To be labeled a $K^{*+}(890)$, the total reconstructed invariant mass of the event, assuming the charged particle to be a

kaon, had to be in the range from 0.790 GeV to 0.990 GeV.

(vi) The candidate $K^{*+}(890)$ decay z-vertex (calculated as was the K^+ decay z-vertex) was restricted to a region around the position of the target from -32 inches to 28 inches (the target was located at z = -2 inches). This choice was dictated by a comparison of real $K^{*+}(890)$ data to Monte Carlo, which indicated a resolution of ~11 inches for the decay vertex.

(vii) Finally, to eliminate the large background from $K^+ \to \pi^+\pi^0$ decays (and to a lesser extend from $K^+ \to e^+\pi^0\nu$ or $K^+ \to \mu^+\pi^0\nu$ decays), where the decay was reconstructed near the target, and the charged particle was incorrectly assigned the kaon mass, a restriction was imposed that the total invariant mass of candidate events, assuming the charged particle to be a pion, be less than 0.580 GeV. This cut played a major role in eliminating beam K^+ decay background in the $K^+\gamma\gamma$ decay mode of the $K^{*+}(890)$ signal while reducing the $K^{*+}(890)$ yield by only ~25%. A cut of this sort was necessitated by the fact that the spectrometer did not distinguish between charged pions or kaons in the final state. This restriction eliminated primarily low-mass $K^+\pi^0$ events, causing the overall acceptance to go to zero for $K^+\pi^0$ massed below ~0.770 GeV (see Figures 45a and 45c).

The additional restrictions imposed to isolate coherently produced $K^{*+}(890)$ events detected in the $\pi^+\pi^+\pi^-$ final state included the above requirements (i), (ii), and (iv) (for these decays, the primary vertex resolution was determined to be ~8 inches) as well as the following cuts:

(i) The reconstructed neutral "V" decay z-vertex was restricted to the range from z = 40 inches to 240 inches. Monte Carlo simulation of this decay indicated a resolution of ~6 inches for the reconstructed z-vertex of the "V" decay. The z-vertex cut was chosen to avoid biases introduced by the S-counter requirement in the V-trigger (see Section A).

There were two possible choices for the assignment of charged particles to the "V" and to the prompt decay vertex of the $K^{*+}(890)$; the choice was made on the basis of the smallest value for the distance of approach between the two charged-particle trajectories for the hypothesized "V", and on the distance of closest approach of the incident K^+ beam track and the trajectory of the hypothesized, positively charged, prompt decay product.

(ii) The reconstructed invariant mass of the neutral "V" particle, assuming both decay products to be pions, had to be between 0.480 GeV and 0.520 GeV to select the K^0_s. The reconstructed invariant mass spectrum for the other choice of particles for the "V" showed absolutely no structure, indicating that the excellent tracking resolution of the charged particle spectrometer invariably provided the right choice.

(iii) For $K^{*+}(890)$ candidates, the total reconstructed invariant mass of the event, assuming all charged particles to be pions, was restricted to the range 0.790 GeV to 0.990 GeV.

The $\pi^+\pi^+\pi^-$ decay of the $K^{*+}(890)$ was not contaminated by K^+ decays. The LAC was not used in studying this decay.

We now present detailed comparisons between the $K\pi$ data and Monte Carlo expectations. All distributions were selected via the previously described cuts. (An empty-target subtraction has been applied to all of the data.)

Figures 36a and 36b show the $K^{*+}(890)$ z-vertex distribution for the sum of events produced on the copper and lead targets. The smooth curves superimposed are the Monte Carlo predictions, normalized to the number of events between the arrows (which also indicate the range of the cut applied to this quantity to select a clean sample of $K^{*+}(890)$ events. The agreement is quite good.

Figures 37a and 37b show a comparison between data and Monte Carlo for the total reconstructed energy distribution of the candidate $K^{*+}(890)$ events, summed for Cu and Pb targets. The Monte Carlo predictions are superimposed on the data and are normalized to the numbers of real data events between the arrows.

Figures 38a and 38b give the reconstructed two-photon and neutral "V" invariant masses, as found in the $K^+\gamma\gamma$ and $\pi^+\pi^+\pi^-$ final-state products of $K^{*+}(890)$ decay. The Monte Carlo predictions are given by the smooth curves, and are normalized to the numbers

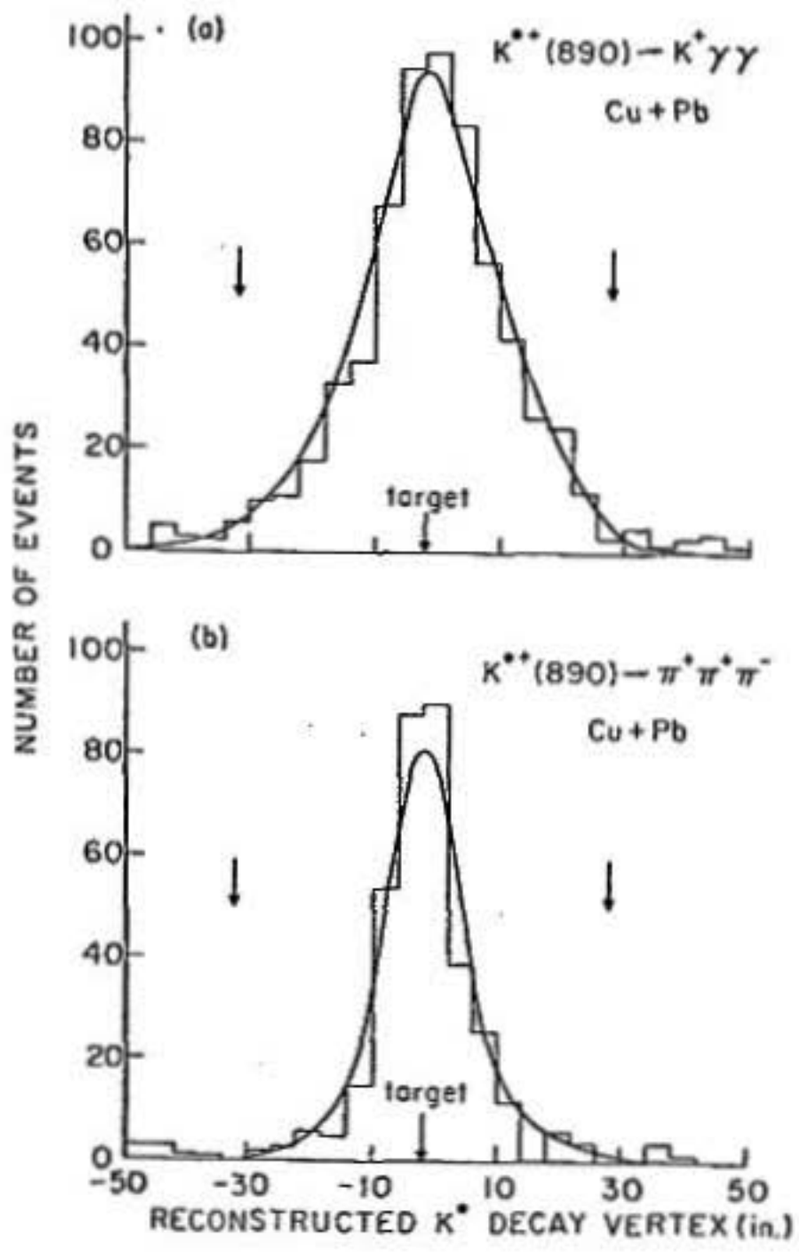

Figure 36

of events between the arrows. A slight discrepancy exists (~1 MeV) in the mean of the reconstructed two-photon mass. This is attributable to the fact that the final fine-tuning of the LAC energy calibration was accomplished using π^0's from beam K^+ decays. The energy spectrum of the π^0's from these events is quite different from that for π^0's originating from $K^{*+}(890)$ decay. For the K^+ events, the π^0 spectrum is highly skewed towards its upper kinematic limit (~ 183 GeV); whereas, the π^0 energy spectrum for π^0's from $K^{*+}(890)$ decay is relatively narrow with a peak at ~ 80 GeV. The final energy calibration of the LAC was biased by events which deposited large amounts of energy, which was not typical of $K^{*+}(890)$ decay π^0's. The effects of this discrepancy are quite minimal because of the loose cuts applied to this distribution. The data and Monte Carlo distributions for the reconstructed neutral "V" mass are in good agreement.

Figure 39a shows the distribution of two-photon energy asymmetry for π^0's found in the $K^+\gamma\gamma$ final state from $K^{*+}(890)$ decay for events produced on coper and lead targets. The superimposed curve is the Monte Carlo expectation normalized to the number of events. The agreement is reasonable, and the reasons for the fall-off as asymmetry increases have already been discussed for the case of beam $K^+ \to \pi^+\gamma\gamma$ decays.

The distribution of reconstructed decay z-vertices, for those neutral "V" particles satisfying the cuts to isolate $K^{*+}(890) \to K^0_S\pi^+ \to \pi^+\pi^+\pi^-$ events, is shown in Figure 39b for events produced

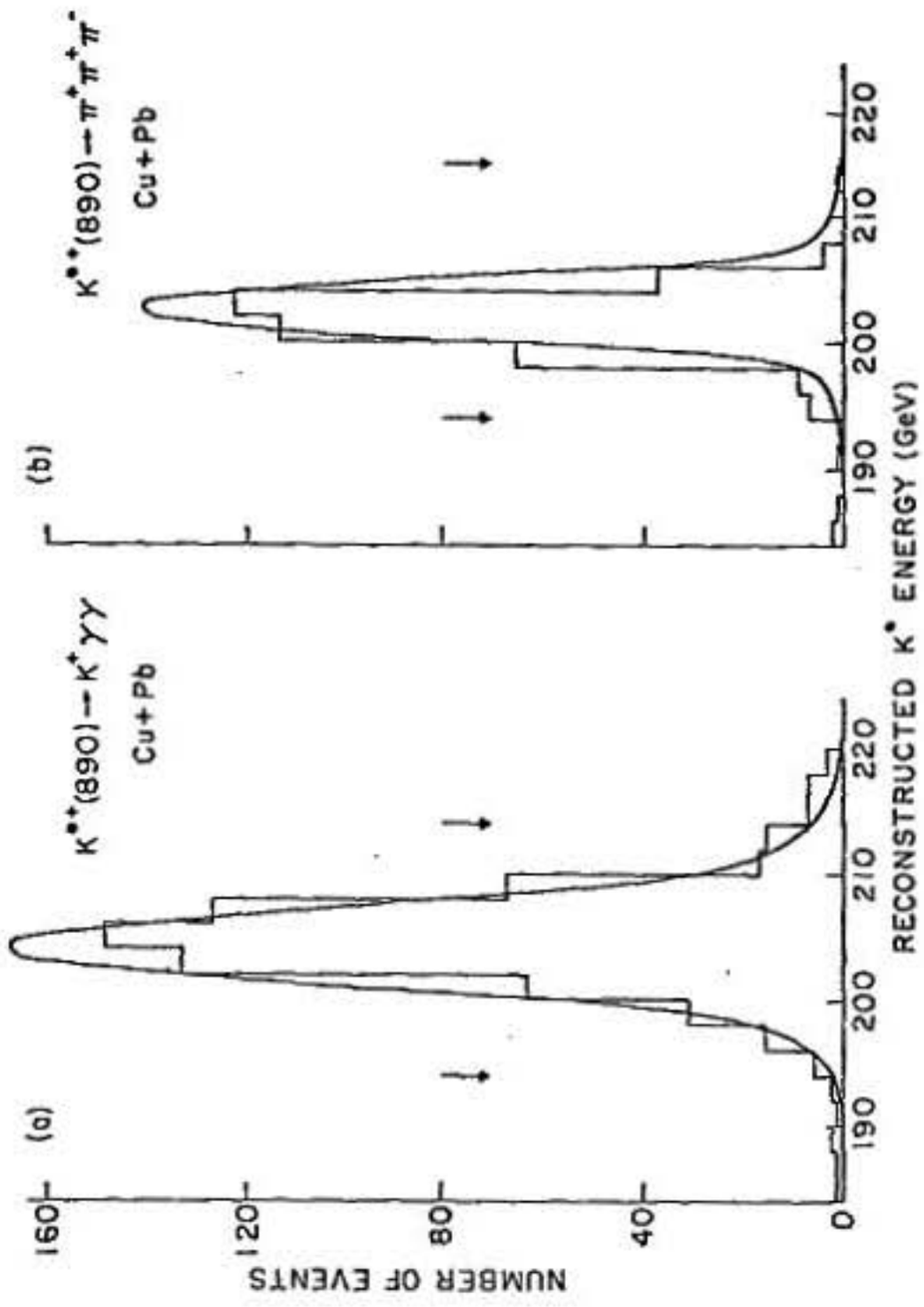

Figure 37

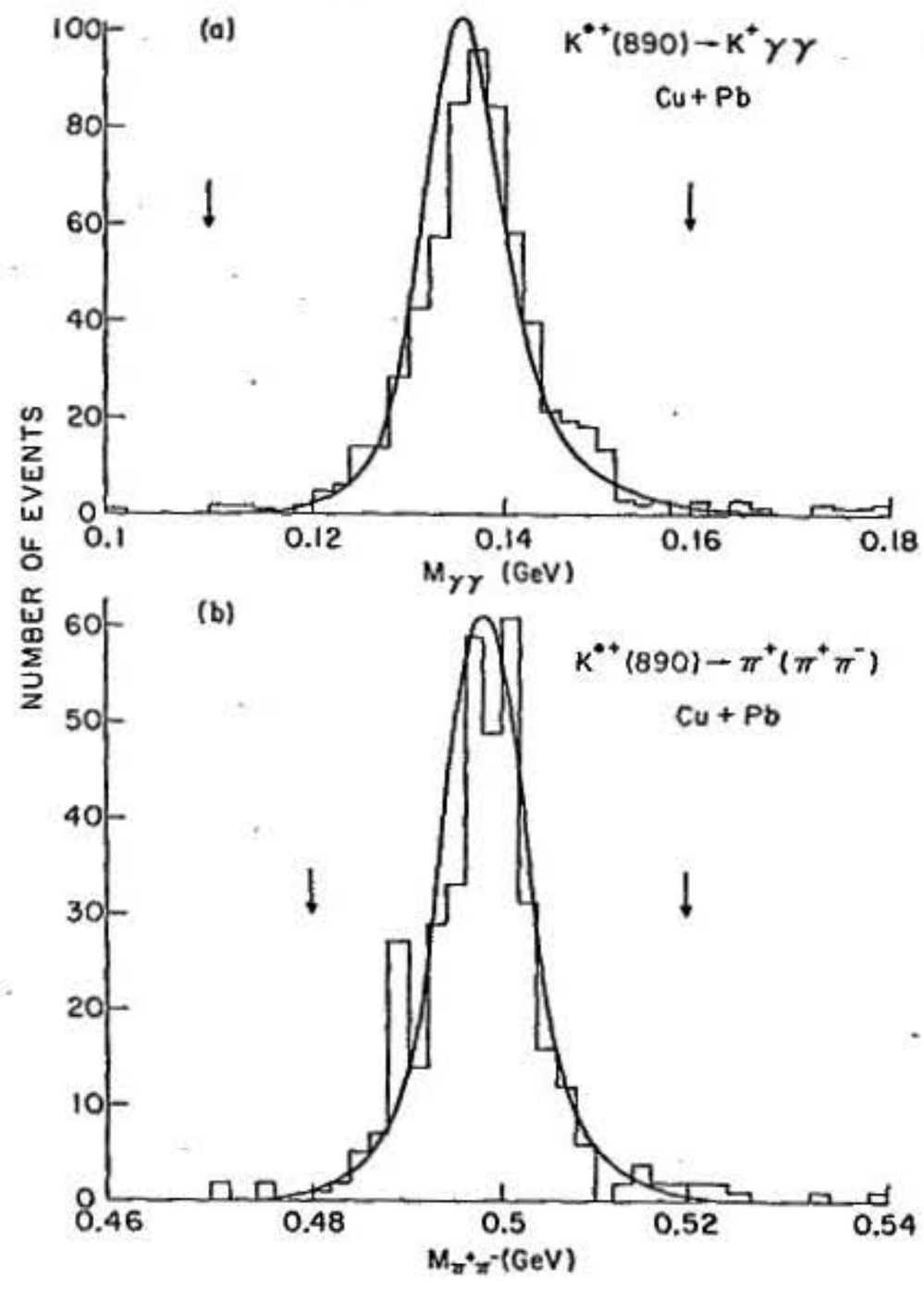

Figure 38

on copper and lead targets. The smooth curve is the Monte Carlo prediction normalized to the number of events between the arrows. The reason for the discrepancy near the target region has been discussed previously.

The distributions in the cosine of the polar decay angle in the Gottfried-Jackson frame for the K^+, and the π^+ resulting from $K^{*+}(890) \to K^+\pi^0$, and $K_s^0\pi^+$ decays for events accumulated using the copper and lead targets, are shown in Figures 40a, and 40b, respectively. The superimposed curves are the Monte Carlo expectations for the decay of a coherently excited spin-1 $K^{*+}(890)$ modified by overall acceptance, and normalized to the total number of events in each histogram. Again, the Monte Carlo predictions agree well with the data.

These comparisons indicate a reasonable consistancy between Monte Carlo predictions and data. Deviations are minimal, and negligibly affect the computation of overall acceptance for the $K^{*+}(890)$ decay modes.

The corrections for overall acceptance, for each target and the two decay modes of the $K^{*+}(890)$, were evaluated using the Monte Carlo program using as input a t' distribution corresponding to Coulomb production, with the strength of the Coulomb production mechanism given by the partial width for $K^{*+}(890) \to K^+\gamma$ decay of 50 keV, a strong contribution of strength $C_S = 2.0$ mb/GeV^4, and a

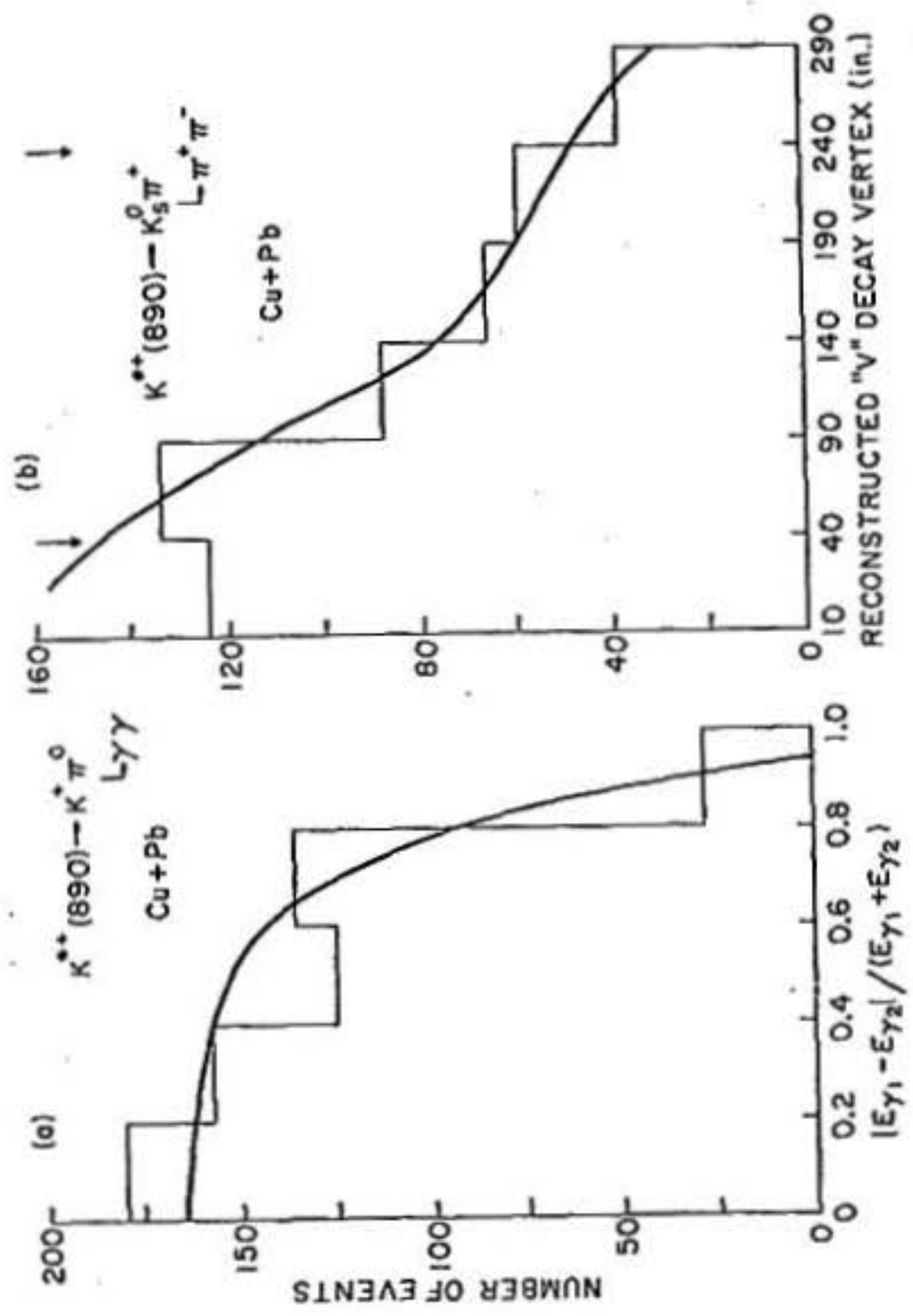

Figure 39

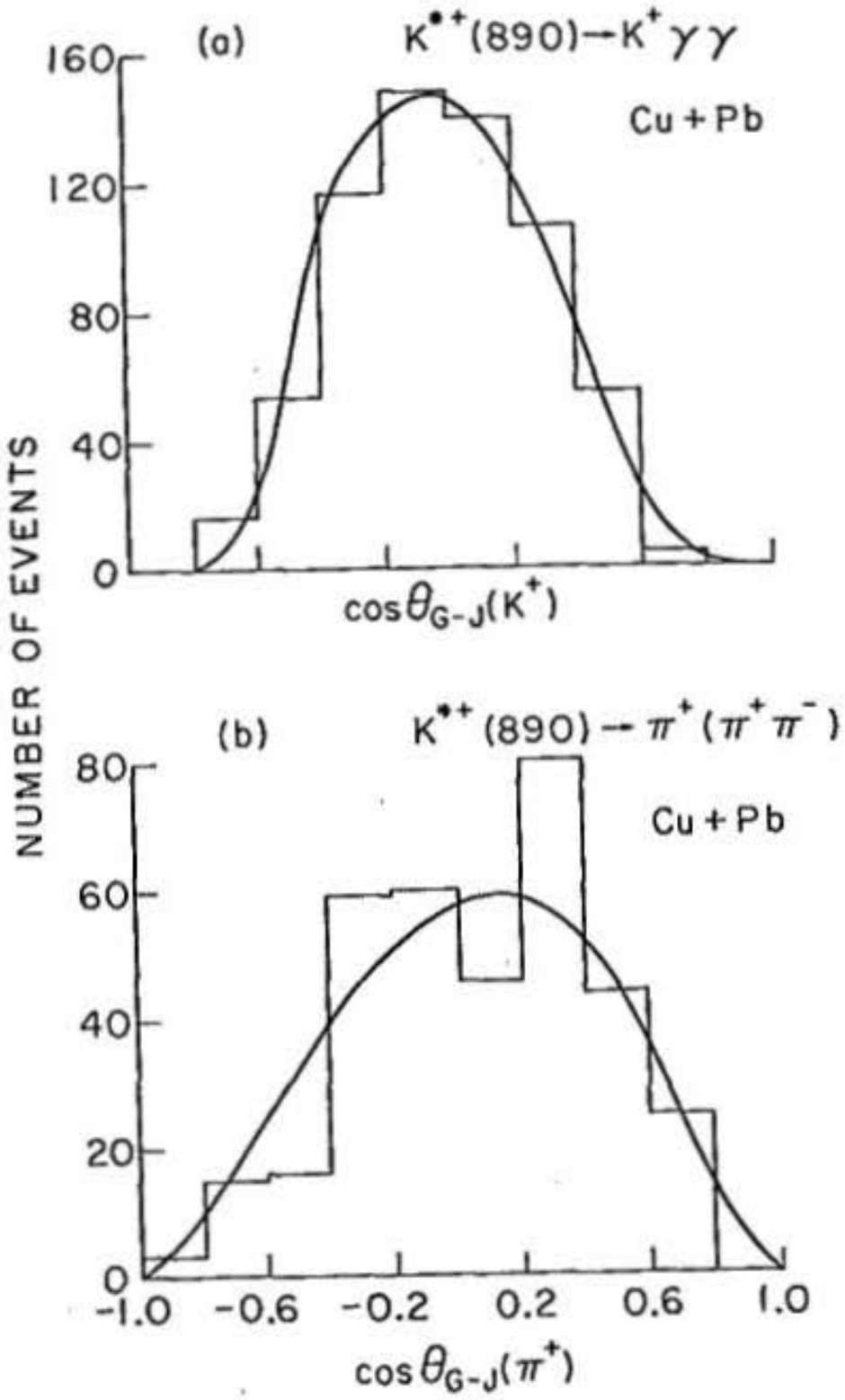

Figure 40

relative phase between the two production amplitudes of $\theta = \pi/2$ radians. The $K^{*+}(890)$ events were generated with a mass distribution given by a relativistic Breit-Wigner function (over the range from the kinematic minimum to 1.6 GeV) distorted by the effects of the two coherent production processes. These distributions used as input to the Monte Carlo program results from a preliminary analysis of the $K^{*+}(890)$ data. More details are given in Section E of Chapter VI. The $K^{*+}(890)$ events generated by the Monte Carlo were allowed to decay according to a $\sin^2\theta\sin^2\theta$ distribution in the Gottfried-Jackson frame. Overall accpetance corrections were calculated for the $K^{*+}(890)$ t' distributions (the correction was found to be independent of t') and $K\pi$ mass distributions, by passing these events through the reconstruction and analysis package used on the real data, and observing the ratio of the number of events emerging from analysis to the number generated for each data bin of the experimental distribution. It was particularly important to use the correct mass distribution for the $K^{*+}(890)$ in the $K^+\gamma\gamma$ final state because of the rapidly changing acceptance across the $K^{*+}(890)$ resonant peak, due to the severe removal of $K^+ \to \pi^+\pi^o$ decays (see Figures 45a and 45c).

The correction factors for overall acceptance for the empty, copper, and lead targets, for $K^{*+}(890) \to K^+\gamma\gamma$ and $\pi^+\pi^+\pi^-$ decays, to be applied to the t' distributions are given in Tables VII.A and VII.B. The number used for the empty target is an average of the results for copper and lead.

Other factors that had to be applied to the event distributions in t' and mass to arrive at absolute cross sections included corrections for branching ratios of the $K^{*+}(890)$ into different final states. Again, these corrections are tabulated in Tables VII.A and VII.B.

Included are corrections for:

Decay	Branching Ratio
(i) $K^{*+}(890) \to K^+\pi^0$	1/3
(ii) $K^{*+}(890) \to K^0\pi^+$	2/3
(iii) $\pi^0 \to \gamma\gamma$	0.9885 ± 0.0005 (Ref. 51)
(iv) $K^0 \to K^0_s$	1/2
(v) $K^0_s \to \pi^+\pi^-$	0.6861 ± 0.0024 (Ref. 51)

where the branching ratios of (i) and (ii) follow from isospin conservation in the strong decay of the $K^{*+}(890)$, and are calculated from Clebsch-Gordan coefficients of an expansion of the $K\pi$ final states in terms of total isospin eigenstates, (iii) and (v) are experimentally determined, and (iv) is calculated (ignoring CP violation) from the expansion of the hypercharge eigenstate $|K^0\rangle$ of the strong decay in terms of the eigenstates $|K^0_s\rangle$ and $|K^0_L\rangle$ of the weak decay Hamiltonian. We observe only the quickly

decaying component $|K^0_s\rangle$.

The total correction factors to be applied to the t' distributions are given for all targets, for the $K^+\gamma\gamma$ and $\pi^+\pi^+\pi^-$ states of the $K^{*+}(890)$, in Tables VII.A and VII.B.

The absolute partial cross sections to be assigned to the ith data bin, of an event distribution containing n_i events, is then given by

$$\sigma_i = (A/N_o\rho\ell)(CF)_i(n_i/\text{flux})$$

where A is the gram molecular weight of the target material, $N_o = 6.023 \times 10^{23}$ is Avogadro's number, ρ is the target density, ℓ is its thickness ($\rho\ell$ is the thickness in units of gm/cm^2), $(CF)_i$ is the total correction factor applied to the ith bin, and "flux" is the appropriate total gated kaon flux. As already pointed out, the $(CF)_i$ given in Tables VII.A and VII.B were independent of t'.

To account for contamination of the $K^{*+}(890)$ signal from events not produced in the target, data were taken with an empty target. To correct the target induced partial cross sections, we made the bin-by-bin target-empty subtractions given by

Table VII.A

Totals of Corrections Applied to the $K^{*+}(890)$ ($\to K^+\gamma\gamma$) t' Distribution

Correction		Empty	Copper	Lead
1.	beam flux corrections	1.071±0.013	1.081±0.009	1.075±0.005
2.	target related corrections	1.016±0.001	1.563±0.005	1.238±0.004
3.	spectrometer related corrections	1.370±0.008	1.331±0.006	1.392±0.005
4.	correction for decay ($K^{*+}\to K^+\pi^0$)	3.000	3.000	3.000
	branching ratio ($\pi^0 \to \gamma\gamma$)	1.012±0.001	1.012±0.001	1.012±0.001
5.	factor from normalization to K^+ decays	1.161±0.054	1.176±0.050	1.193±0.047
6.	correction for acceptance	3.865±0.034	3.895±0.035	3.836±0.034
Total correction factor		20.30 ±0.99	31.24 ±1.38	25.73 ±1.05

Table VII.B

Totals of Corrections Applied to the $K^{*+}(890)$ ($\to \pi^+\pi^+\pi^-$) t' Distribution

Correction			Empty	Copper	Lead
1.	beam flux corrections		1.065±0.045	1.026±0.036	1.070±0.021
2.	target related corrections		1.016±0.001	1.150±0.003	1.054±0.001
3.	spectrometer related corrections		1.374±0.014	1.385±0.016	1.397±0.011
4.	correction for decay branching ratio	($K^{*+}\to K^0\pi^+$)	1.500	1.500	1.500
		($K^0 \to K^0_S$)	2.000	2.000	2.000
		($K^0_S\to\pi^+\pi^-$)	1.458±0.005	1.458±0.005	1.458±0.005
5.	factor from normalization to K^+ decays		1.004±0.048	1.306±0.037	1.300±0.034
6.	correction for acceptance		5.338±0.055	5.339±0.054	5.338±0.055
Total correction factor			34.82 ±2.28	49.82 ±2.40	47.82 ±1.69

$$\sigma_i = (A/N_o\rho\ell)\left[\frac{CF_{iA}\, n_{iA}}{flux_A} - \frac{CF_{iMT}\, n_{iMT}}{flux_{MT}}\right].$$

Here, the subscripts A and MT refer to the target type (A = copper or lead, MT = empty target), and the number of empty target induced events in the ith bin is properly corrected by the correction factor CF_{iMT}, and suitably weighted by the amount of incident kaon beam taken on this target. For the $K^{*+}(890)$ distributions, the procedure used for making target-empty subtractions to histograms is indicated by the form of the term in square brackets above, but normalized by the factor $CF_{iA}/flux_A$.

Figures 41a,b and 41c,d show the reconstructed invariant masses for the final states $K^+\gamma\gamma$ and $\pi^+\pi^+\pi^-$, for candidate K^{*+} events, using the previously described cuts, subsequent to target empty subtractions. After conversion to absolute cross sections, using the μb equivalents per event $(A/N_o\rho\ell)(CF_{iA}/flux_A)$, these distributions are fit to extract $K^{*+}(890)$ line-shape parameters: mass m_o and width $\Gamma(m_o)$. The arrows in these figures indicate the range of masses used in the t' differential cross sections.

Figures 42a, b, c, and d show the reconstructed t' distributions for $K^{*+}(890)$ events. After conversion to absolute cross

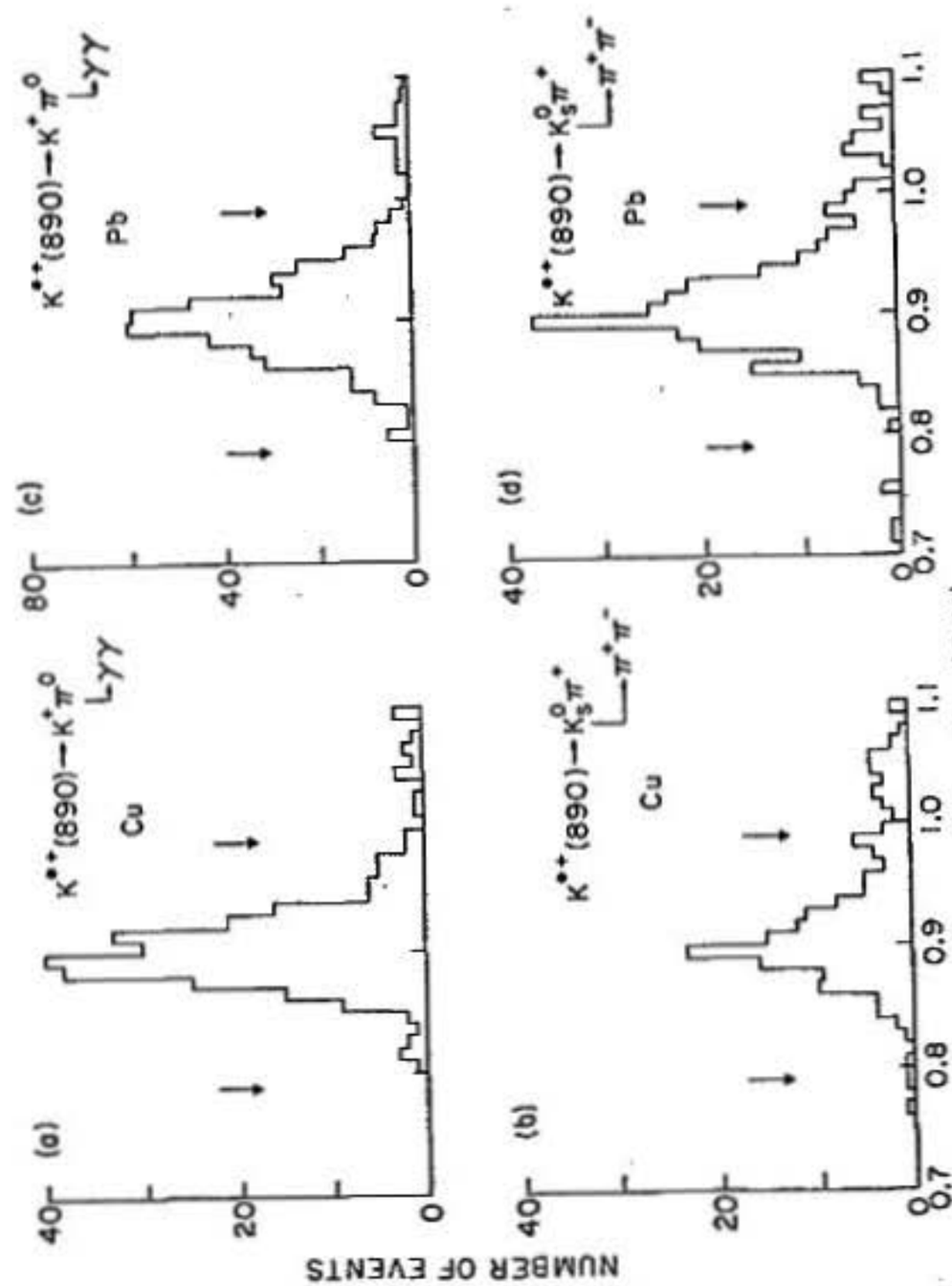

Figure 41

sections, these data are fitted to the theoretical form of $d\sigma/dt'$ used to extract the radiative decay width of the $K^{*+}(890)$, $\Gamma(K^{*+}(890) \to K^+\gamma)$, the strength of the elementary strong contribution to coherent production of $K^{*+}(890)$'s, C_s, and the relative phase θ between the Coulomb and strong production amplitudes.

The μb equivalents per event for the t' distributions, $(A/N_o\rho\ell)(CF_A/flux_A)$, for the target parameters listed in Table V, the gated kaon flux on each target given in Section B of Chapter III, and the total correction factors listed in Tables VII.A and VII.B are:

Target	Detected final state	μ-barn equivalent (μb/event)	
Cu	$K^+\gamma\gamma$	1.218 ± 0.054	(333)
	$\pi^+\pi^+\pi^-$	1.942 ± 0.094	(177)
Pb	$K^+\gamma\gamma$	4.473 ± 0.183	(486)
	$\pi^+\pi^+\pi^-$	8.313 ± 0.294	(256)

The numbers in parentheses give the total number of $K^{*+}(890)$ events in the t' distributions with $-t' < 0.010$ GeV^2, surviving all cuts

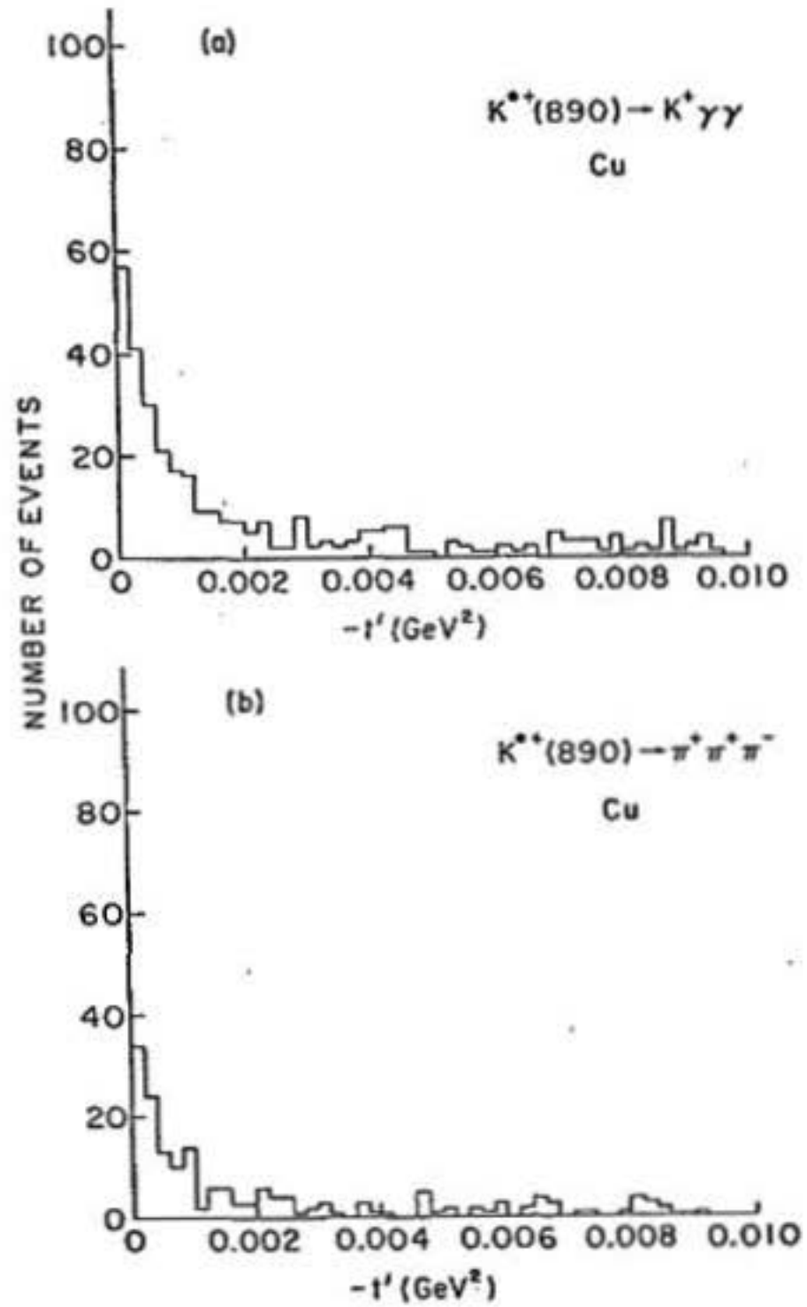

Figure 42

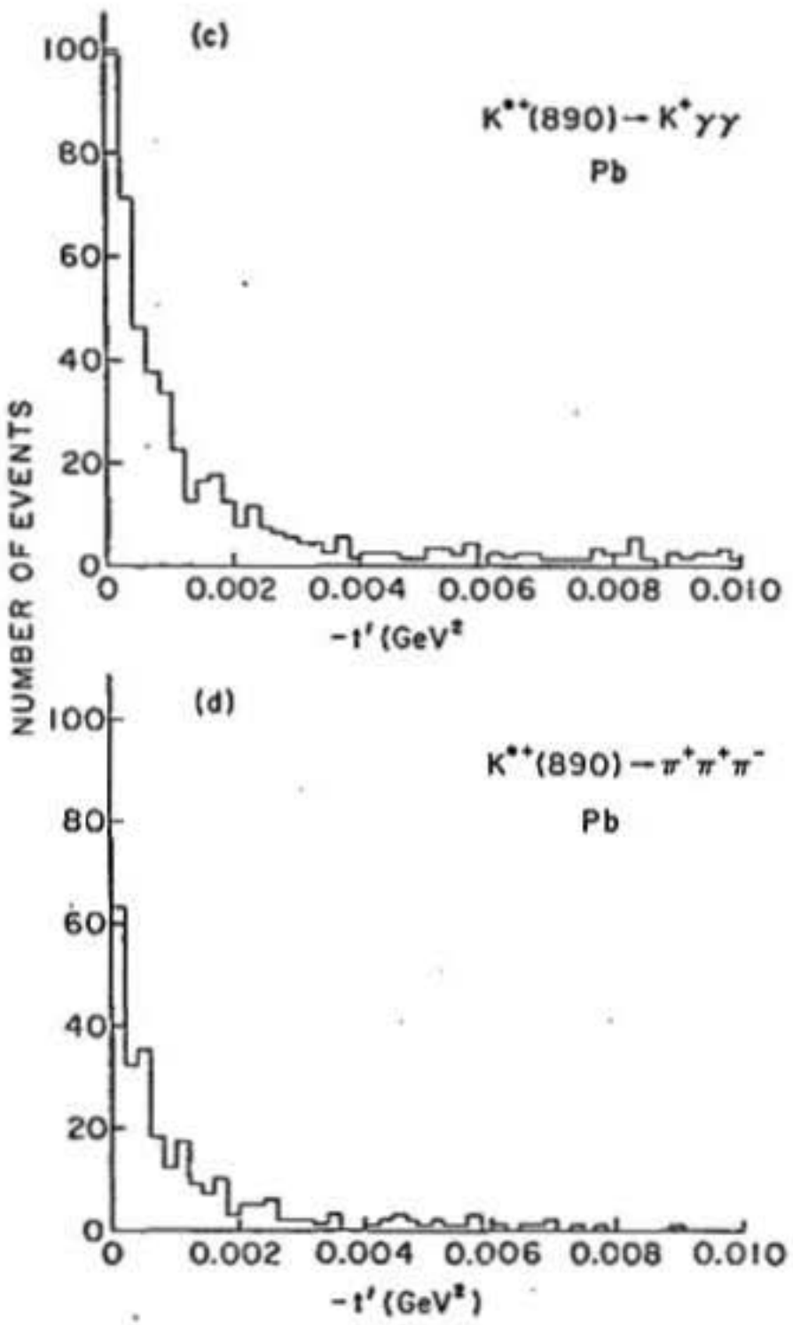

Figure 42

(after an empty target subtraction). The relative sensitivity of the measurements is given by the inverse of these μb equivalents.

Lastly, we turn to a discussion of the possible backgrounds in the $K^{*+}(890)$ signal leaking through the restrictions imposed to select the signal. For the $K^+\gamma\gamma$ final state, possible backgrounds included beam kaon decays of the sort $K^+ \to \pi^+\pi^0$, $K^+ \to e^+\pi^0\nu$, and $K^+ \to \mu^+\pi^0\nu$, as well as contamination from diffractively produced $Q^+ \to \pi^+\pi^0\pi^0$ events, and coherently excited events induced by the pion fraction of the beam.

The possibility of the presence of the latter source of contamination can be ignored because the contamination from pions in the K12 Cherenkov tagging signal was less than 1%, as indicated in Figure 4. As already mentioned, the strict $K^+ \to \pi^+\pi^0$ cut imposed on the $K^{*+}(890)$ data eliminated this source of contamination, and also suppressed beam K_{e3} and $K_{\mu 3}$ decay contaminations. Monte Carlo simulations of these decays indicated that the latter two decays were eliminated as a source of contamination by the excellent energy resolution of the apparatus. Although the neutrinos from these decays escaped detection, the majority of these decays were eliminated by the restrictions on t' and on the total reconstructed energy applied to the data. The cut requiring that the charged particle in the final state deposit no more than 90% of its energy in the LAC further reduced the possibility of a K_{e3} background. Monte Carlo simulations of these decays showed that those events still

passing all cuts would reconstruct to have masses well above the range chosen to select $K^{*+}(890)$ events. Background from diffractively produced $Q^+ \to K^+\pi^0\pi^0$ events, where a low energy π^0 may have gone undetected, was also shown to be negligible by a Monte Carlo simulation of this decay, again due to the excellent t' and energy resolution of the apparatus, and the low energy threshold for photon reconstruction.

This same rationale applied to the elimination of diffractively produced $Q^+ \to K_s^0\pi^+\pi^0$ events as a source of background in the $\pi^+\pi^+\pi^-$ decay channel of the $K^{*+}(890)$, as was verified by Monte Carlo results. Pion induced contamination in this mode was also ignored for reasons given above.

Therefore, as a result of Monte Carlo simulations, the various requirements imposed to select the $K^{*+}(890)$ signal were deemed to provide negligible sources of background, and the final samples of $K\pi$ events were judged to be essentially pure $K^{*+}(890)$.

CHAPTER VI

FITTING OF $K^{*+}(890)$ DATA

A. Introduction

This chapter deals with the fitting of the experimentally derived distributions for the coherently produced $K^{*+}(890)$. Included are fits to the polar-angle decay distributions in the Gottfried-Jackson frame, a fit to the extract the mean life-time of the K_s^0 from the $K^{*+}(890) \to K_s^0\pi^+$ data sample, and fits to the differential cross sections $d\sigma/dm$ and $d\sigma/dt'$ for the four data sets, consisting of events obtained on copper and lead targets for the $K^+\gamma\gamma$ and $\pi^+\pi^+\pi^-$ final states. A brief discussion of the optical model calculation of the form factors $f_c(t)$ and $f_s(t)$, and the final theoretical forms of $d\sigma/dm$ and $d\sigma/dt'$ to be fit, are also presented.

B. Check on Decay Angular Distributions

Plots of the polar decay angle distributions in the Gottfried-Jackson frame for the K^+ resulting from $K^{*+}(890) \to K^+\pi^0$, and for the π^+ from the $K_s^0\pi^+$ decay, after correction for overall acceptance, and a target empty subtraction, are shown in Figures 43a and 43b. These distributions are plotted as a function of $\cos\theta_{GJ}$, where θ

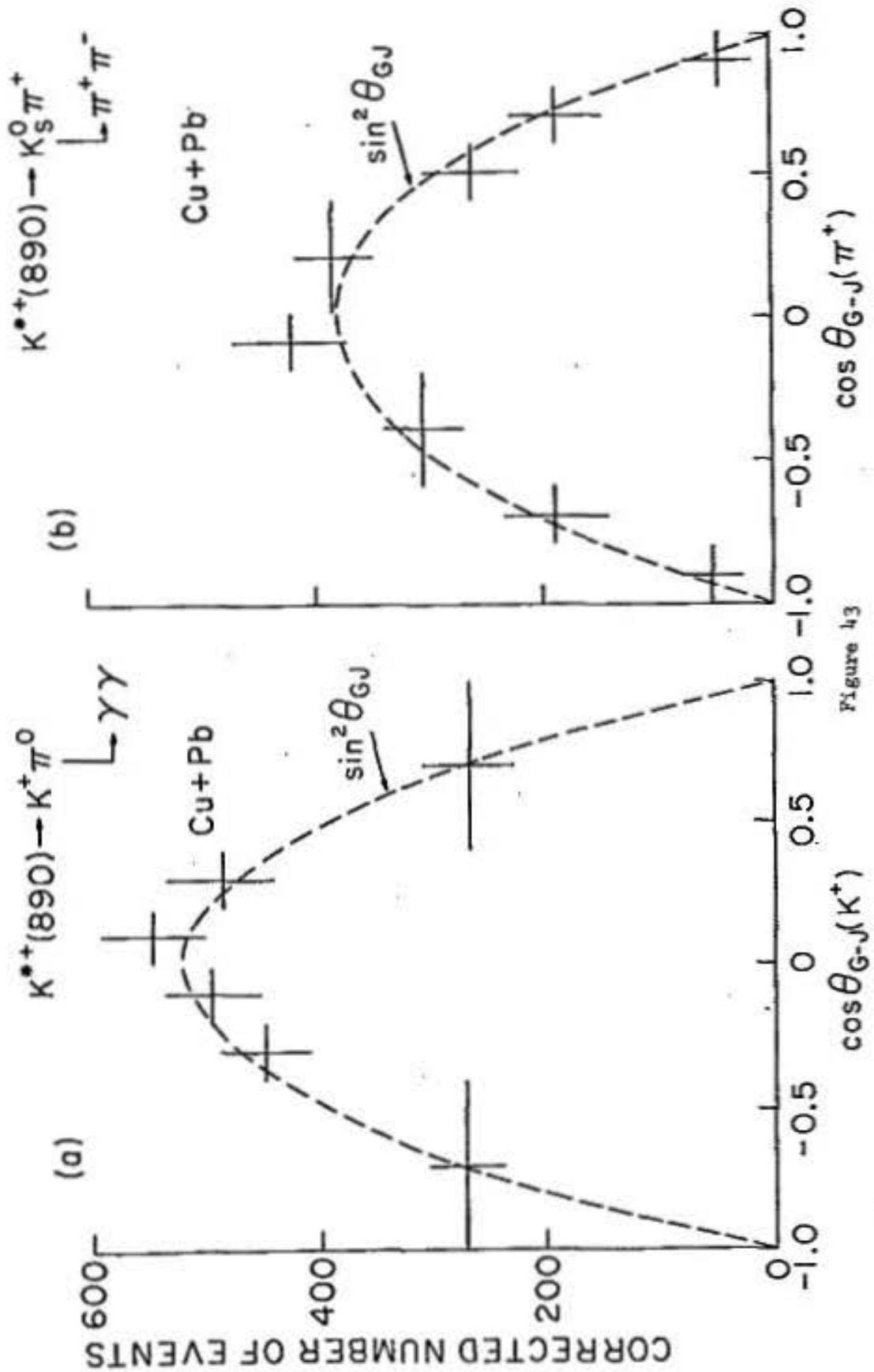

Figure 43

is the polar angle. These data include events with $-t' < 0.004$ GeV^2, and invariant $K\pi$ mass between 0.790 GeV and 0.990 GeV.

The corrections for overall acceptances were calculated on a bin-by-bin basis by generating $K^{*+}(890)$ events with the Monte Carlo, and letting them decay with a $\sin^2\theta\sin^2\phi$ decay angular distribution. The bin-by-bin $\cos\theta$ acceptances were simply the ratio of the number of events surviving reconstruction and analysis to the number generated in each bin. The corrections applied to the data were the reciprocals of these acceptances.

Superimposed on Figures 43a and 43b are the $\sin^2\theta$ distributions expected for $K^{*+}(890)$ decays, normalized to the total number of corrected events in each plot. The χ^2 per degree of freedom for the fits are 1.3/5 and 2.8/7, respectively, implying that the data are indeed distributed according to $\sin^2\theta$ with a high confidence level. These results indicate convincingly that the sample consists of coherently excited $K^{*+}(890)$ events. (The $\sin^2\theta\sin^2\phi$ form is expected for Coulomb excitation as well as for ω-exchange.)

The azimuthal distributions in ϕ are not presented because at small values of t', these distributions are severely affected by the resolution of the spectrometer. As a result, there exists an ambiguity (approaching π as $t' \to 0$) in defining the orientation of the production plane for such events, and consequently the distributions contain little information.

C. Check on K_s^o Life-time

Data on the decay mean free path of K_s^o's from $K^{*+}(890) \rightarrow K_s^o\pi^+$ decays was used to extract a measurement of the K_s^o mean life-time. A cut of $-t' < 0.004\ GeV^2$ was imposed on the data, and the reconstructed $K_s^o\pi^+$ mass was required to fall in the range from 0.790 GeV to 0.990 GeV. Figure 44 shows the distribution of the K_s^o life-times in its rest frame, after application of overall bin-by-bin acceptance corrections and a bin-by-bin empty target subtraction. Each event life-time in its rest frame was calculated from the Lorentz dilated life-time $\tau' = \gamma\tau$ observed in the laboratory. Since the K_s^o's travelled at nearly the speed of light, τ' was calculated from the distance travelled by the K_s^o, defined as the distance between the point of closest approach of the π^+ trajectory from the $K^{*+}(890)$ decay and the incident beam track, to the reconstructed $\pi^+\pi^-$ vertex of the K_s^o, divided by the speed of light. The Lorentz dilation factor γ was given by $(p^2 + m^2)^{1/2}/m$ for the K_s^o, as determined from the decay pions.

The dotted line superimposed in Figure 44 is the result of a fit of the form $Ae^{-\tau/\tau_o}$. The fitted result for the K_s^o mean life-time τ_o was $0.89 \pm 0.09 \times 10^{-10}$ seconds in good agreement with the world average.[51]

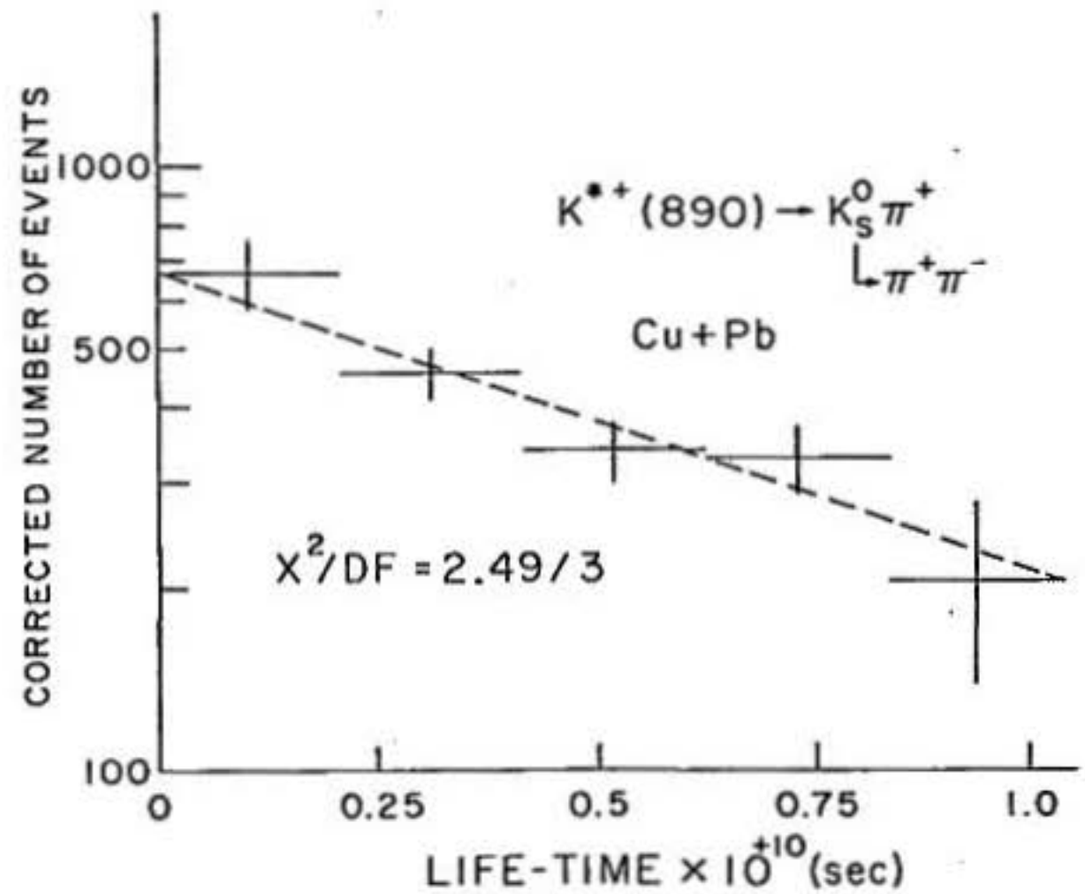

Figure 44

D. Fitting Formalism for the Differential Cross Section

The form factors $f_c(t)$, and $f_s(t)$ in Equations (11), and (15), respectively, were calculated numerically using an optical model for the nucleus. Specific details may be found elsewhere[33]; however, some points of general interest are:

(i) The nuclear charge and matter distributions were taken to be identical.

(ii) In evaluating $f_c(t)$, the nuclear charge distribution was described by a sphere of uniform charge density. This approximation sufficed for Coulombic production since most of the production occurs at large impact parameters. The radius of the nucleus was taken to be $r = (c^2 + (7/3)(\pi/a)^2)^{1/2}$, where $c = 1.12\ A^{1/3}$ fermi (A is the nucleon number) and $a = 0.545$ fermi. This radius is equivalent to that in the Woods-Saxon distribution, which is used in the calculation of $f_s(t)$.

(iii) Since the strong production amplitude is sensitive to the nuclear shape (production is concentrated at the surface of the nucleus), a Woods-Saxon parameterization for the matter density was used. That is, $\rho(r) = \rho_o/(1 + \exp(\frac{r-c}{a}))$.

(iv) Effects of nuclear absorption of the incoming K^+ and outgoing K^{*+} were accounted for.

(v) The cross sections of K^*'s and K's on nucleons were

taken to be equal, and given by $\sigma' = \sigma(1-i\alpha)$, where σ is given by the total cross section of K^+'s on nucleons[63], and α is the ratio of real to imaginary parts of the forward K^+-proton scattering amplitude[64] at 200 GeV/c.

Returning now to Equations (17) and (18), and using Equation (16), and the definitions of the production amplitudes $F_c(t,m)$ and $F_s(t,m)$, and the T-matrix element given by Equations (14), (15), and (13), we can write

$$\frac{d\sigma}{dm} = \frac{2m\ m_o^2\ \Gamma_{K\pi}(m)}{(m^2-m_o^2)^2 + m_o^2\Gamma_{K\pi}^2(m)} \cdot \int_o^{t'_{max}} dt'\ K(t',m) \tag{20}$$

where

$$K(t',m) = 24\ Z^2\alpha\ \frac{m^2}{(m^2-m_K^2)^3}\ \Gamma_{K\gamma}(m)\left(\frac{t'}{t^2}\right)|f_c|^2$$

$$+ C_s A^2 t' |f_s|^2$$

$$+ (24\ Z^2\alpha\Gamma_{K\gamma}(m) C_s A^2)^{1/2}\ \frac{m}{(m^2-m_K^2)^{3/2}}\left(\frac{t'}{t}\right)\ 2\mathrm{Re}(f_c f_s^*) \tag{21}$$

and

$$\frac{d\sigma}{dt'} = \int dm^2\, K(t',m)\, \frac{m_o^2 \Gamma_{K\pi}(m)}{(m^2 - m_o^2)^2 + m_o^2 \Gamma_{K\pi}^2(m)} \qquad (22)$$

These are the basic theoretical forms that will be used to fit the experimental cross sections. These expressions were fit using the χ^2 minimization program MINUIT.[65]

E. Fits to $d\sigma/dm$

The differential cross sections $d\sigma/dm$ for $K^{*+}(890)$ production on copper and lead targets are presented in Figures 45a, b, c, and d. The overall acceptance as a function of mass, for each of these data sets, is shown above the distributions. Each of these distributions has been fully corrected. The data are for events with $-t' < 0.004\ \mathrm{GeV}^2$.

At this point, an aside on the determination of overall acceptance corrections for both the $K^{*+}(890)$ mass and t' distributions is in order. Preliminary investigations with the Monte Carlo program indicated that the acceptance in t' was independent of t' over the range of interest to us. However, the mass acceptance was not uniform, and bin-by-bin corrections were required. The calculation of these bin-by-bin corrections for the mass distributions involved an iterative process. First, a simple, undistorted, relativistic p-wave Breit-Wigner of constant width was used

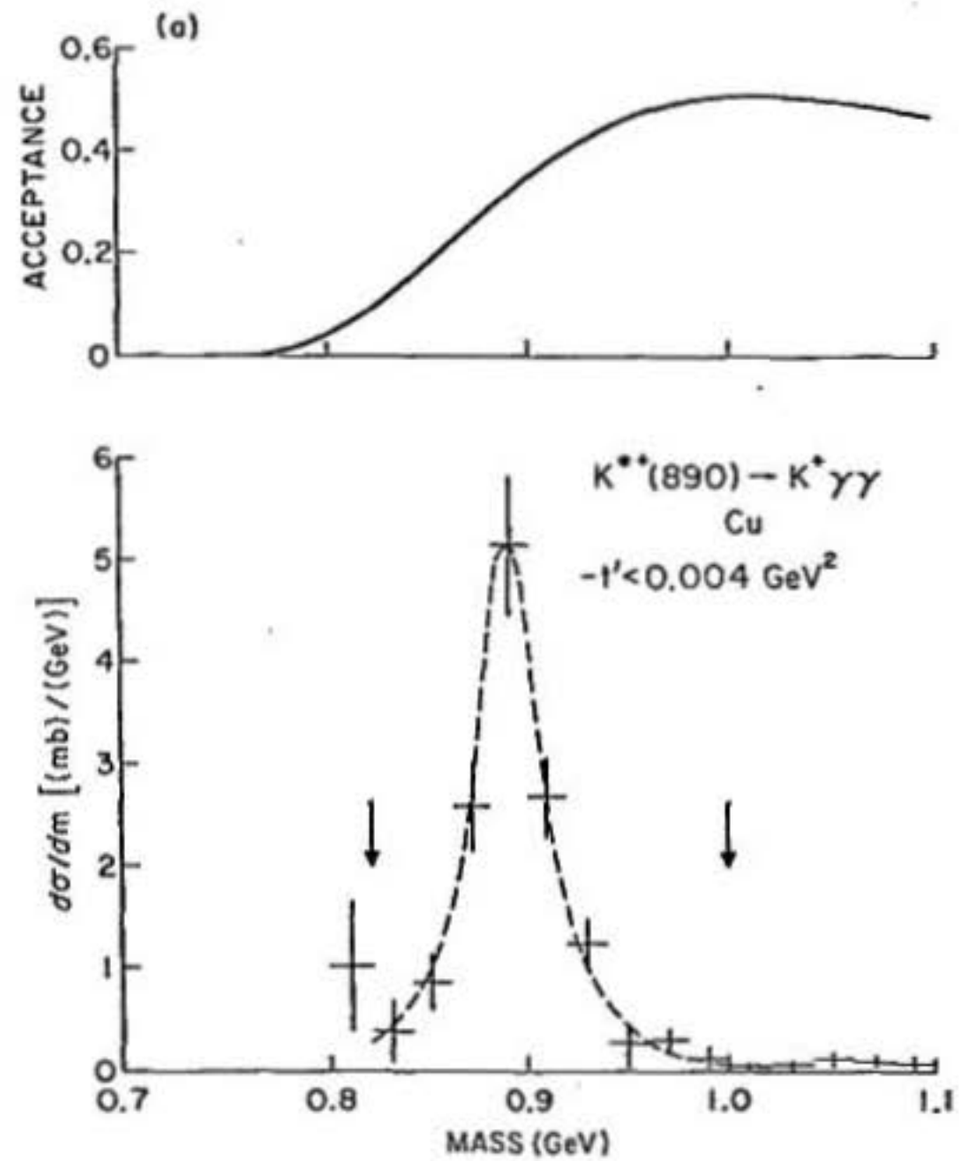

Figure 45

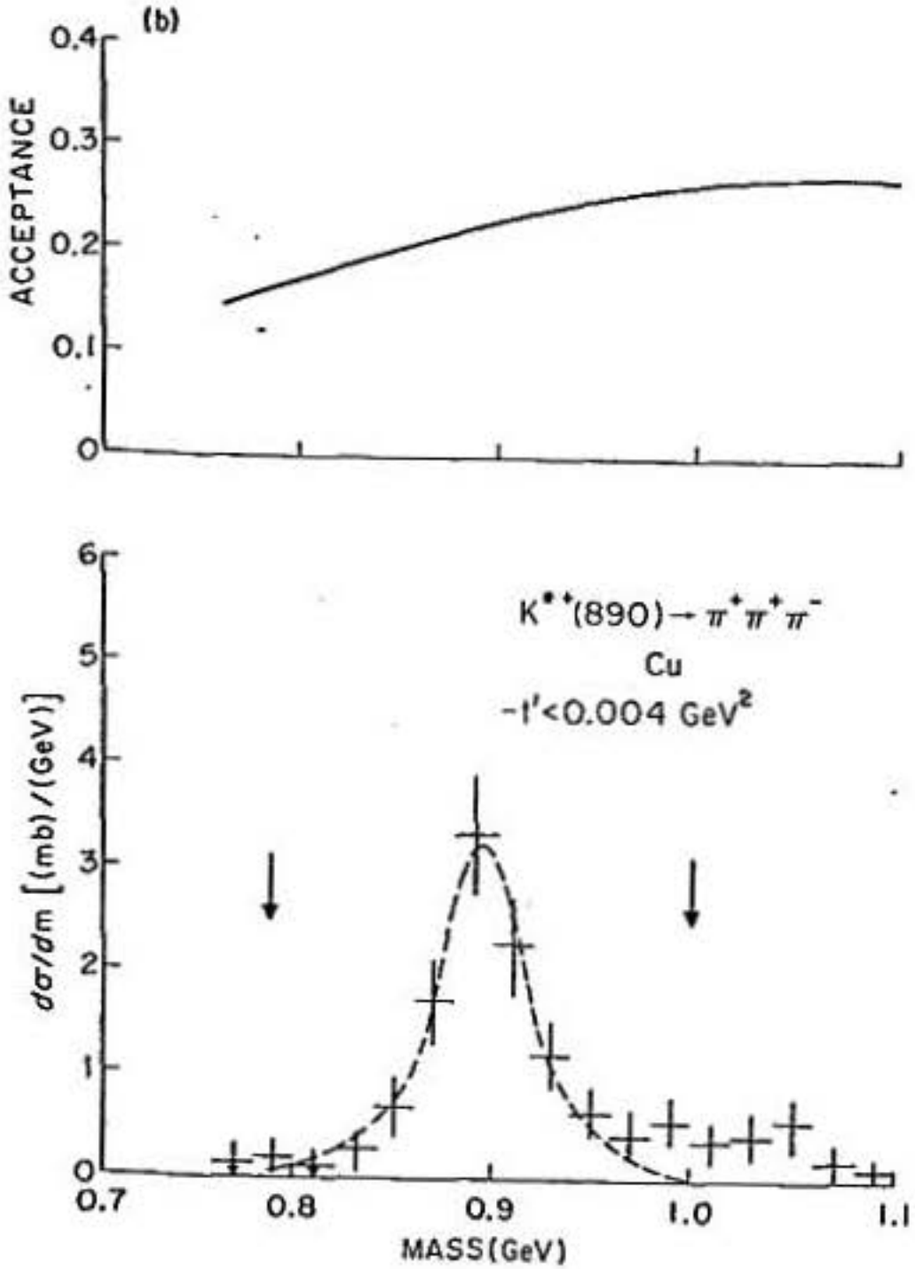

Figure 45

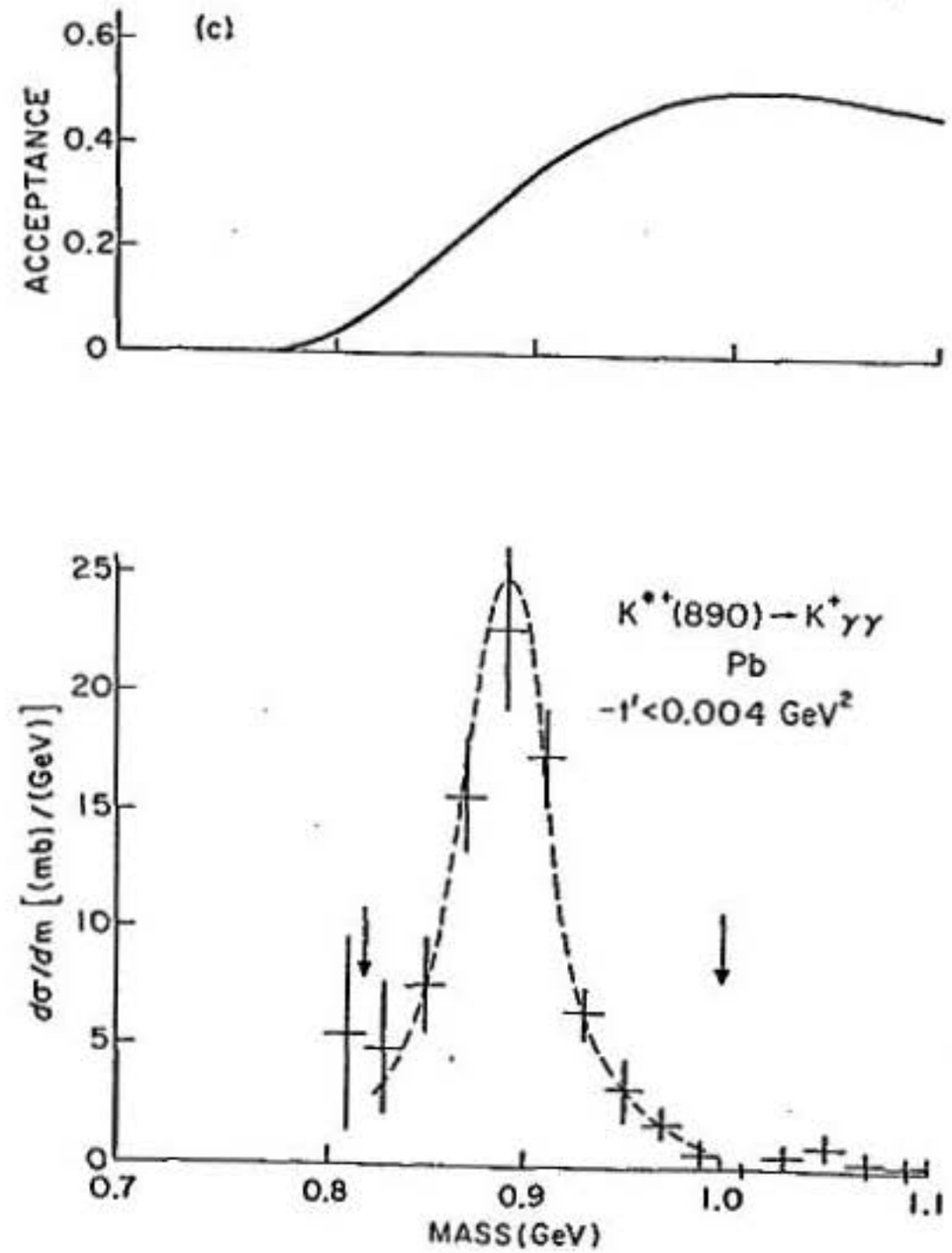

Figure 45

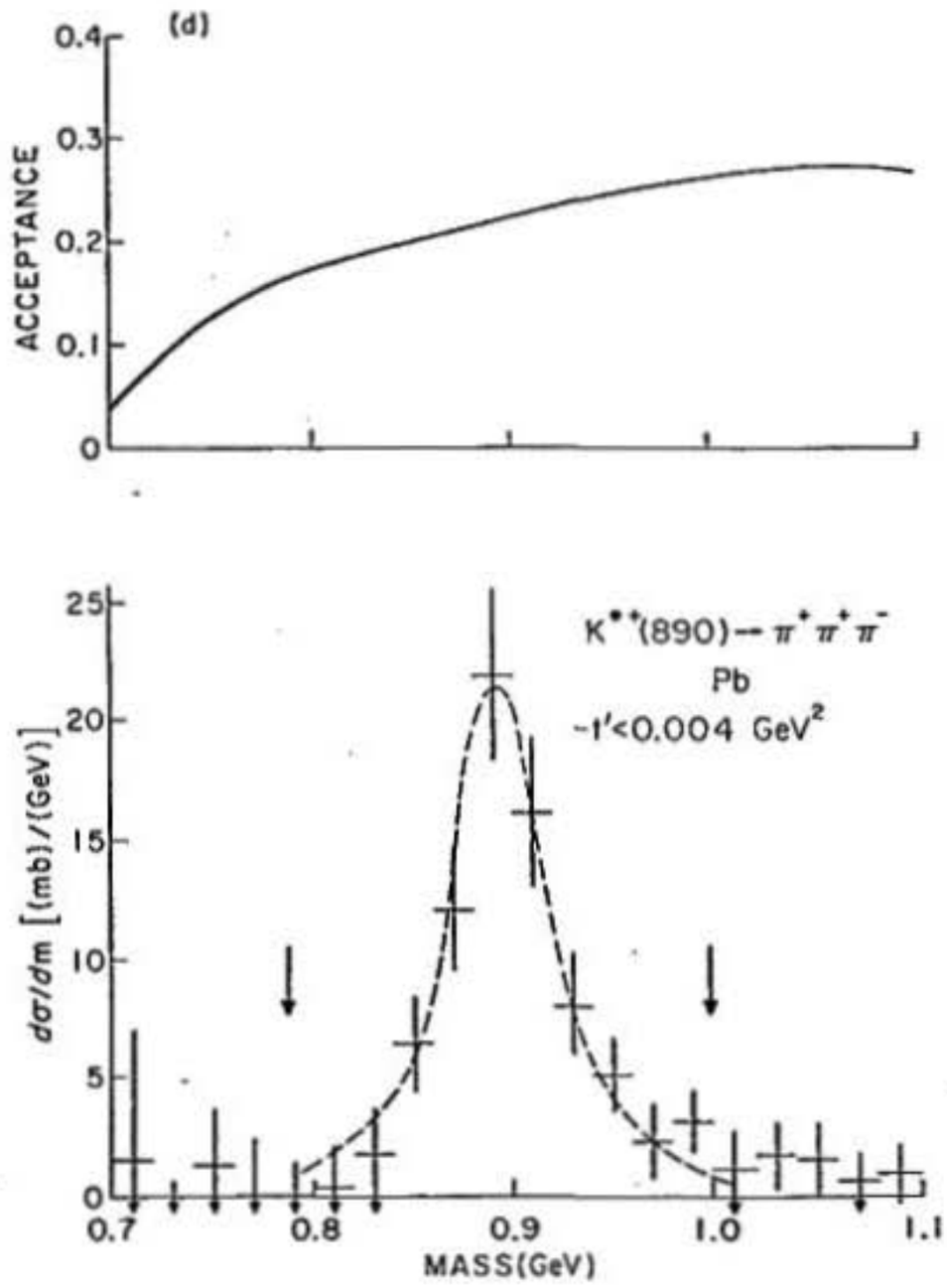

Figure 45

to specify the distribution of $K^{*+}(890)$ masses in the Monte Carlo. The first-pass acceptance corrections to be applied to t' distributions were calculated and used to get preliminary distributions in $d\sigma/dt'$. These cross sections were then fit (see Section E) to extract preliminary values for $\Gamma(K^{*+}(890) \to K^+\gamma)$, C_s and θ (these initial results were almost identical to the final results). These results were then used to calculate a distorted $K^{*+}(890)$ line shape as given by Equation (20). The energy dependences of the partial widths were parameterized as $\Gamma_{K\pi} = \Gamma_o (q/q_o)^3 \, 2q_o^2/(q^2 + q_o^2)$ and $\Gamma_{K\gamma} = \Gamma_{\gamma o} (k/k_o)^2 \, 2k_o^2/(k^2 + k_o^2)$. Here q and k refer to the momenta of the decay particles, and the zero subscript indicates evaluation at the $K^{*+}(890)$ resonant mass, in the rest frame of the $K^{*+}(890)$. In these expressions, the first factors in parenthesis represent the effects of the centrifugal barrier to decay, while the other factors are empirical. This new line shape was then introduced into the Monte Carlo program to generate $K^{*+}(890)$ events. Bin-by-bin corrections to the mass distributions for overall acceptance were then determined again, and applied to the data. Using the parameterizations for the partial widths $\Gamma_{K\pi}(m)$ and $\Gamma_{K\gamma}(m)$ that best fit the data (they were found to be identical to those originally chosen), the overall acceptance correction to be applied to the t' distributions was then calculated in its final form.

The theoretical line shape given by Equation (20) represents the modified relativistic resonant shape expected for the decay of $K^{*+}(890)$ to two pseudoscalar mesons; the shape is distorted by the Coulombic and hadronic production processes. The distorting effect is introduced through the integral over t'. The integrand K(t',m) was evaluated numerically at various mass and t' bins using the optical model previously described for the calculation of f_c and f_s and, again, the preliminary values for $\Gamma_{\gamma o}$, C_s, and θ were used. Because the cut-off $-t' < 0.004\ \mathrm{GeV}^2$ was applied to real data, smeared by experimental resolution, K(t',m) was first smeared by the resolution function $R(\vec{P}_T,\tilde{\vec{P}}_T)$ (see Equation (19) in Section A, Chapter V)

$$\tilde{K}(t',m) = \int d\vec{P}_T\ R(\vec{P}_T,\tilde{\vec{P}}_T)K(t',m)$$

then numerically integrated from $t' = 0$ to $-t' = 0.004\ \mathrm{GeV}^2$. The resulting expression for $d\sigma/dm$ was then averaged over the experimental mass bins and fit to the data to extract the resonant mass m_o and width Γ_o. The overall normalization was allowed to vary freely.

Several parameterizations of the partial widths were investigated. Besides the two already mentioned, which gave the best fits, the following forms were also tried:

$$\Gamma_{K\gamma} = \begin{cases} \Gamma_{\gamma o}\ (k/k_o)^3\ 2k_o^2/(k^2 + k_o^2) \\ \Gamma_{\gamma o}\ (k/k_o)^2\ m/m_o \\ \Gamma_{\gamma o}\ (k/k_o)^3\ m/m_o \end{cases}$$

All of these gave results for m_o and Γ_o within 0.002 GeV of the best fits.

The best-fit line shapes for the $K^{*+}(890)$ are shown by the dotted lines superimposed on the data in Figures 45a-d. The arrows on the figures show the range over which the data were fit to the theoretical line shape. The fits assumed that there were no backgrounds.

The fitted resonant parameters for the four data sets are presented in Table VIII. The errors quoted are purely statistical. The weighted average for the resonant mass is in good agreement with the accepted value;[51] however, the weighted average for the width is somewhat below the accepted value.[51,66]

F. Fits to $d\sigma/dt'$

Using Equations (21) and (22), we can write

$$\frac{d\sigma}{dt'} = 24\ Z^2\alpha \int dm^2 \Gamma_{K\gamma}(m)\ \frac{t'}{t^2}\ |f_c|^2\ \frac{m_o^2\ \Gamma_{K\pi}(m)}{(m^2-m_o^2)^2+m_o^2\Gamma_{K\pi}^2(m)}\ \frac{m^2}{(m^2-m_K^2)^3}$$
$$+C_sA^2 \int dm^2\ t'|f_s|^2\ \frac{m_o^2\Gamma_{K\pi}(m)}{(m^2-m_o^2)^2 + m_o^2\Gamma_{K\pi}^2(m)}$$
$$+ (24Z^2\alpha C_sA^2)^{1/2}\int dm^2\Gamma_{K\gamma}^{1/2}(m)\ \frac{t'}{t}\ 2\mathrm{Re}(f_cf_s^*)\ \frac{m_o^2\Gamma_{K\pi}(m)}{(m^2-m_o^2)^2 + m_o^2\Gamma_{K\pi}^2(m)}$$

Table VIII

Results of Fits to the $K^{*+}(890)$ Mass Differential Cross Sections

Target	Observed final state	mass range of fit (GeV)	m_o (GeV)	Γ_o (GeV)	χ^2/DF
Cu	$K^+\gamma\gamma$	0.820 - 1.000	0.893 ± 0.002	0.036 ± 0.005	4.36/6
	$\pi^+\pi^+\pi^-$	0.780 - 1.000	0.895 ± 0.003	0.047 ± 0.007	4.85/8
Pb	$K^+\gamma\gamma$	0.820 - 1.000	0.894 ± 0.003	0.047 ± 0.006	2.84/6
	$\pi^+\pi^+\pi^-$	0.780 - 1.000	0.893 ± 0.003	0.052 ± 0.009	4.67/8
<u>weighted averages:</u>			m_o = 0.894 ± 0.001 GeV		
			Γ_o = 0.043 ± 0.003 GeV		

The integrals on m^2 run from the kinematic minimum for the $K\pi$ final state up to some maximum value. For this maximum, we choose $m^2_{MAX} = (1.6\ \text{GeV})^2$, and duplicated this upper limit in the Monte Carlo when generating $K^{*+}(890)$ masses in the process of calculating the overall acceptance correction for t' distributions. The convergence properties of the above integrals are, therefore, not important.

Due to the strongly peaked nature of the relativistic Breit-Wigner term in these integrals, and to the fact that factors such as t', f_c, and f_s depend only weakly on mass, the latter terms were taken outside of the integral, and evaluated at the accepted value of m_o for the $K^{*+}(890)$.[51] Substituting the parametrizations of the partial widths $\Gamma_{K\gamma}(m)$ and $\Gamma_{K\pi}(m)$ found to provide the best fit to the $K^{*+}(890)$ mass spectrum, we can write:

$$\frac{d\sigma}{dt'} = 24\ z^2\alpha\Gamma_{\gamma o}\frac{t'}{t^2}|f_c|^2 \cdot C_1$$

$$+ C_s A^2 t' |f_s|^2 \cdot C_2$$

$$+ (2\sqrt{2}\, z^2\alpha\Gamma_{\gamma o} C_s A^2)^{1/2}\frac{t'}{t}\, 2\mathrm{Re}(f_c f_s^*) \cdot C_3 \qquad (23)$$

where C_1, C_2, and C_3 are constants given by

$$C_1 = \int dm^2 \frac{m_o^2[\Gamma_o(q/q_o)^3 2q_o^2/(q^2+q_o^2)][(k/k_o)^2 2k_o/(k^2+k_o^2)]}{(m^2-m_o^2)^2+m_o^2[\Gamma_o(q/q_o)^3 2q_o^2/(q^2+q_o^2)]^2} \cdot \frac{m^2}{(m^2-m_K^2)^3}$$

$$C_2 = \int dm^2 \frac{m_o^2\Gamma_o(q/q_o)^3\ 2q_o^2/(q^2+q_o^2)}{(m^2-m_o^2)^2 + m_o^2[\Gamma_o(q/q_o)^3\ 2q_o^2/(q^2+q_o^2)]^2}$$

$$C_3 = \int dm^2 \frac{m_o^2[\Gamma_o(q/q_o)^3 2q_o^2/(q^2+q_o^2)][(k/k_o)^2 2k_o/(k^2+k_o^2)]^{1/2}}{(m^2-m_o^2)^2+m_o^2[\Gamma_o(q/q_o)^3 2q_o^2/(q^2+q_o^2)]^2} \cdot \frac{m}{(m^2-m_K^2)^{3/2}}$$

These integrals were evaluated numerically using the accepted world averages for the resonant parameters m_o and Γ_o for the $K^{*+}(890)$ line shape.[51]

Before fitting the experimental $d\sigma/dt'$ distributions to Equation (23), the theoretical expression must be smeared to account for the finite transverse momentum resolution of the experimental apparatus. The experimental cross sections are convolutions of the true form $\partial\sigma/dt'$, and the resolution function $R(\vec{P}_T,\vec{\tilde{P}}_T)$ given by Equation (19). We have

$$\left.\frac{d\sigma}{dt'}\right]_{smeared} = \int d\vec{\tilde{P}}_T\ R(\vec{P}_T,\vec{\tilde{P}}_T)\ \left.\frac{d\sigma}{dt'}\right]_{true}$$

The meaning of $R(\vec{P}_T,\vec{\tilde{P}}_T)$, and the assumptions surrounding its choice, are given in Section A of the previous chapter.

In order to smear the theoretical expression, we need to know the variance in P_T for each target and for each final state. These parameters were determined using Monte Carlo $K^{*+}(890)$ events generated at $t' = 0$. The values for $\sigma^2_{P_T}$ at $t' = 0$ were then extracted from the reconstructed t' distributions. These values were assumed to be independent of t'. Recalling the fact that the Monte Carlo underestimated the P_T resolution, each value of $\sigma^2_{P_T}$ for the $K^{*+}(890)$ was increased as prescribed in Chapter V, Section A. The final results for σ_{P_T}, with the copper target in place, were 13.9 MeV/c and 13.8 MeV/c for the detected final states $K^+\gamma\gamma$ and $\pi^+\pi^+\pi^-$, respectively. For the lead target, the values of σ_{P_T} were 12.2 MeV/c and 12.4 MeV/c, respectively.

The final theoretical differential cross sections consisted of averages of the smeared forms, integrated over the experimental bins. The χ^2 sum of the squares of the deviations of the experimental data points from these theoretical bin averages, weighted by the inverse squares of the experimental errors, was formed and minimized to extract the values of the radiative partial width of the $K^{*+}(890)$, $\Gamma(K^{*+}(890) \to K^+\gamma)$, the strength of the elementary strong contribution to coherent production of the $K^{*+}(890)$, C_s, and the relative phase θ between the two production amplitudes.

The fully corrected experimental differential cross sections in t', for $K^{*+}(890)$ data obtained from copper and lead targets, are shown in Figures 46a and 46b. As already mentioned, these distributions reflect an effective integration over the full

$K^{*+}(890)$ line shape, from the kinematic minimum to 1.6 GeV.

The superimposed dotted lines in these figures result from the three-parameter fits described above, over the range from $t' = 0$ to $-t' = 0.010\ GeV^2$. The resultant extracted values for $\Gamma(K^{*+}(890) \to K^+\gamma)$, C_s, and θ are tabulated in Table IX. The quoted errors are purely statistical.

In order to study the sensitivity of the fits, two-parameter fits were tried with C_s or θ fixed at the values of 0.0 to 4.0 mb/GeV^4, and 0 to 2π radians, respectively. The phase angle θ varied by more than $\pi/2$ radians when C_s was changed by more than $2 mb/GeV^4$ from its nominal three-parameter fitted value; however, $\Gamma(K^{*+}(890) \to K^+\gamma)$ remained throughout within its error limits. As θ increased from 0 to 2π radians, C_s varied by as much as 5 mb/GeV^4, revealing a strong correlation between the fitted results for C_s and θ. Again, the extracted values of $\Gamma(K^{*+}(890) \to K^+\gamma)$ remained within the error limits, except in the region of $\theta \gtrsim \pi$ radians, where the deviations were nevertheless less than twice the statistical errors. A one-parameter fit, performed with C_s and θ constrained at zero (i.e. assuming pure Coulombic production), gave a weighted average over the four data sets of 61 ± 2 keV. This error is statistical only.

Three-parameter fits, with $-t' < 0.002\ GeV^2$, gave results consistent with the fits to $-t' < 0.01\ GeV^2$. Needless to say, C_s and θ were poorly determined in this case, since the fit was restricted primarily to the Coulombic peak.

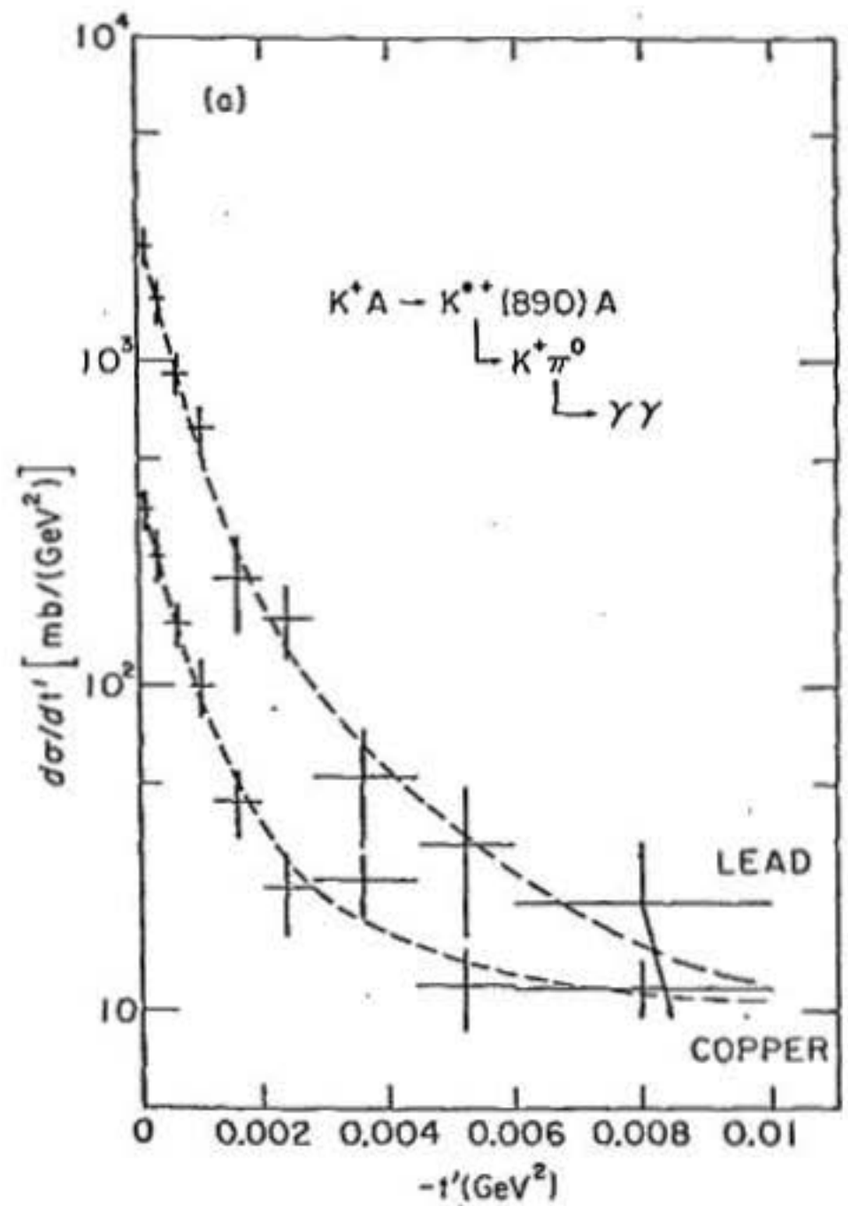

Figure 46

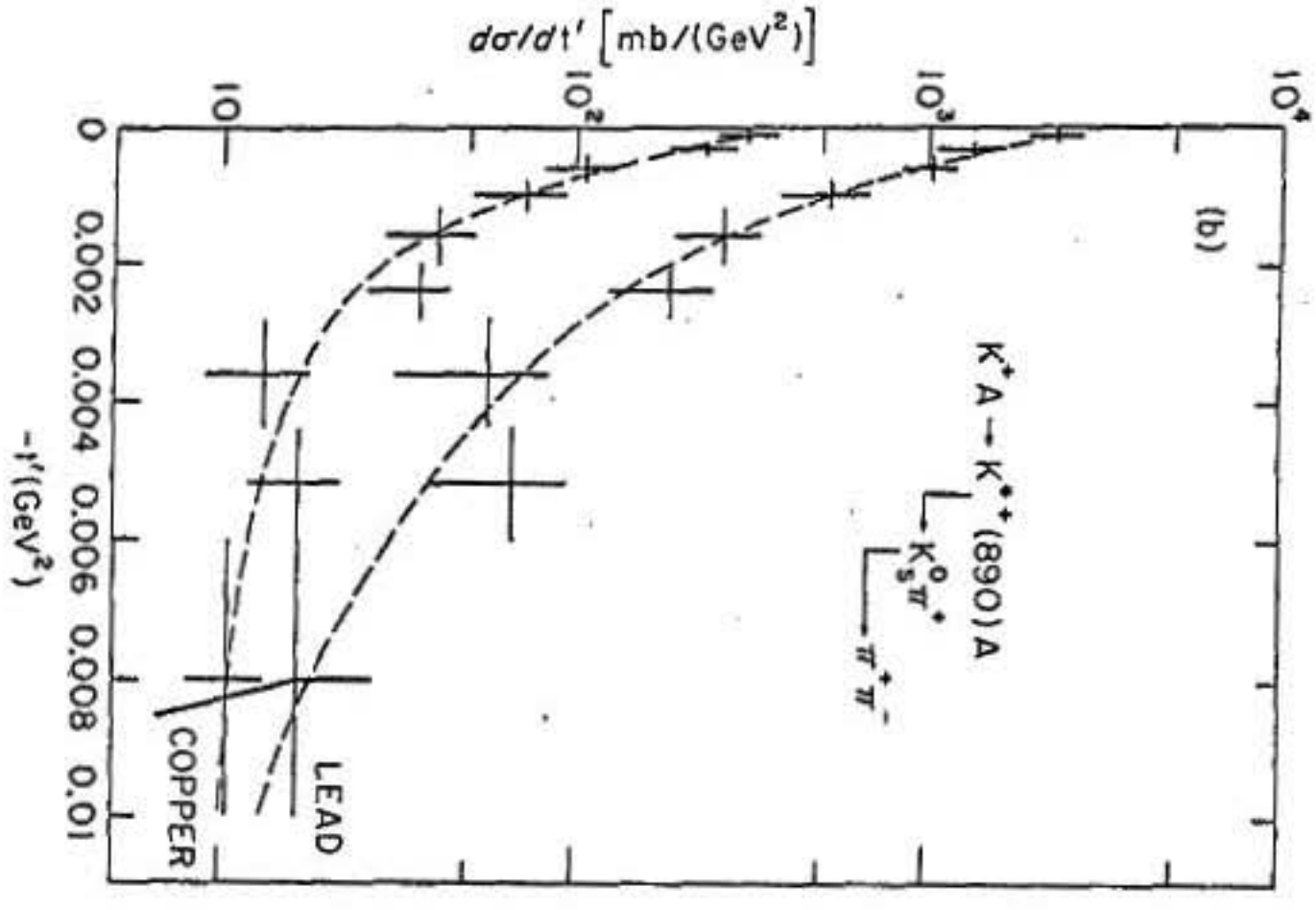

Figure 46

TABLE IX

Results of Fits to the $K^{*+}(890)$ $-t'$ Differential Cross Sections

target	observed final state	$-t'$ range of fit (GeV^2)	$\Gamma(K^{*+}(890)\to K^+\gamma)$ (keV)	C_s (mb/GeV^4)	θ (degrees)	χ^2/DF
Cu	$K^+\gamma\gamma$	< 0.010	62 ± 6	2.9 ± 1.0	85 ± 26	3.5/6
	$\pi^+\pi^+\pi^-$	< 0.010	51 ± 7	2.8 ± 1.1	85 ± 32	3.8/6
Pb	$K^+\gamma\gamma$	< 0.010	48 ± 4	4.2 ± 2.0	84 ± 28	3.5/6
	$\pi^+\pi^+\pi^-$	< 0.010	47 ± 6	4.9 ± 2.2	82 ± 30	2.9/6
Global Fit		< 0.010	51 ± 3	2.4 ± 0.8	64 ± 26	21.2/33

To gain an understanding of the effects of a possible systematic error in the values used for σ_{P_T} in the resolution smearings of the theoretical cross sections, three-parameter fits on all data sets up to $-t' = 0.010\ GeV^2$ were performed, allowing σ_{P_T} to vary by $\pm 10\%$. The extracted values of $\Gamma(K^{*+}(890) \rightarrow K^+\gamma)$ were seen to vary by roughly $\pm$ 8%.

Finally, a global fit over all four data sets, with the nominal values for σ_{P_T}, and a fitted range up to $-t' = 0.010\ GeV^2$, constraining C_s and θ to be independent of target material, was performed. The results of this fit are also given in Table IX, with only statistical errors shown.

CHAPTER VII

CONCLUSIONS

A. Introduction

It is apparent from Table IX that the fits to the experimental differential cross section provide consistent results for $\Gamma(K^{*+}(890) \rightarrow K^+\gamma)$. This consistency fosters a sense of confidence in these measurements, and encourages the belief that all possible systematic errors in determining absolute cross sections have been properly addressed.

The fitted values of $\Gamma(K^{*+}(890) \rightarrow K^+\gamma)$ are relatively insensitive to target material, indicating that target related corrections, and biases affecting cross sections, have also been handled correctly. The agreement of the extracted results for data from both decay modes of the $K^{*+}(890)$, each demanding completely different hardware trigger requirements, and presenting different difficulties in reconstruction and subsequent analysis, supports the belief that the treatment of correction factors and normalizations has been proper.

Therefore, the claim appears justified that the task which this thesis addressed has been accomplished; namely, that a definitive measurement of the radiative decay width of the $K^{*+}(890)$ has been obtained.

B. Final Results

Besides the statistical errors on $\Gamma(K^{*+}(890) \to K^+\gamma)$ quoted in Table IX, errors associated with systematic cross section normalization uncertainties, and uncertainties in the experimental P_T resolution must be considered and appropriately convoluted with the statistical errors. The former are directly related to errors in $\Gamma(K^{*+}(890) \to K^+\gamma)$ through the cross section formula (Equation (23)), whereas the latter translate into compounded errors in $\Gamma(K^{*+}(890) \to K^+\gamma)$ by means of the fitting procedure.

The systematic normalization errors for both $K^{*+}(890)$ decay modes arise primarily from unknown factors contributing to the discrepancy between the experimentally observed and the theoretically expected decay yields for beam kaons decaying to channels topologically similar to the $K^{*+}(890)$ final states. These systematic errors are estimated to be 5% and 10% of the total normalization for the $K^+\gamma\gamma$ and $\pi^+\pi^+\pi^-$ final states, respectively.

As noted earlier, a change in the experimental P_T resolution by $\pm$ 10% manifests itself as a variation of the resultant fitted solution for $\Gamma(K^{*+}(890) \to K^+\gamma)$ by roughly $\pm$ 8%. Since it is believed that σ_{P_T} is known to an accuracy of 5%, the error contribution to $\Gamma(K^{*+}(890) \to K^+\gamma)$ from uncertainty in σ_{P_T} is estimated to be 4% for all the data.

Taking an average of each of the fitted values of $\Gamma(K^{*+}(890) \to K^+\gamma)$, weighted by the inverse squares of the statistical errors, gives the result $\Gamma(K^{*+}(890) \to K^+\gamma) = 51 \pm 3 \pm 4$ keV, where the errors represent overall statistical and systematic uncertainties, respectively.

Adding these errors in quadrature gives a final result of

$$\Gamma(K^{*+}(890) \to K^+\gamma) = 51 \pm 5 \text{ keV}$$

Using the excepted world average for the total decay width of the $K^{*+}(890)$,[51] this measurement implies a radiative branching ratio of 0.10 ± 0.01%.

This measurement is in complete agreement with the original upper limit for this rate, reported by Bemporad et al, of $\Gamma(K^{*+}(890) \to K^+\gamma) < 80$ keV.[67] The agreement is also excellent with the earlier, but statistically poorer, measurement by our group for the charge conjugate reaction, $\Gamma(K^{*-}(890) \to K^-\gamma) = 62 \pm 14$ keV.[68] Finally, this measurement is in best accord with the non-relativistic quark model predictions, presented in Chapter I (assuming exact SU(3) symmetry).

A weighted average of the extracted values for C_s gives $C_s = 3.2 \pm 0.7$ mb/GeV^4, where the error is purely statistical in nature. This result does not agree well with an extrapolation from lower energy results of Bemporad et al, assuming an inverse dependence on beam momentum.

A weighted average of the relative phase θ between the two production amplitudes gives $\theta = 84 \pm 14$ degrees, where the error is purely statistical.

C. Discussion of Results

The final value quoted above for the transition rate $K^{*+}(890) \to K^+\gamma$ can be compared with an early measurement at Brookhaven energies for

the width for the decay $\overline{K^{o*}} \to \overline{K^{o}}\gamma$. Exact SU(3) symmetry predicts the ratio $\Gamma(\overline{K^{o*}} \to \overline{K^{o}}\gamma)/\Gamma(K^{*+} \to K^{+}\gamma) = 4.0$. Using this previous measurement of $\Gamma(\overline{K^{o*}} \to \overline{K^{o}}\gamma) = 75 \pm 35$ keV, and the result presented here, we calculate this ratio to be 1.5 ± 0.7. As discussed in Chapter I, in the regime of broken SU(3), using quark magnetic moments as inferred from measurements of baryon magnetic moments, this ratio is 1.64, which agrees well with this experimental value, but using this same method for calculating the rate $\Gamma(\overline{K^{o*}} \to \overline{K^{o}}\gamma)$ gives values much higher than the experimental result. This difficulty is compounded by the fact that the measurement of $\Gamma(K^{*+}(890) \to K^{+}\gamma)$ reported here agrees best with the quark model predictions assuming no phenomenological symmetry breaking.

A historical suspicion exitst concerning the reliability of the analysis used in the first generation radiative decay experiments. In particular, the first measurements for the rates $\rho^- \to \pi^-\gamma$ and $K^{*+}(890) \to K^{+}\gamma$ showed an A dependence for measured values of C_s. This effect was not seen in the original $\overline{K^{o*}} \to \overline{K^{o}}\gamma$ data. This sort of effect can be explained by an isovector exchange (A_2) contribution to strong coherent production.[69]

Data from the previous experiment on the $\rho^- \to \pi^-\gamma$ transition could not be re-analyzed to include an A_2 exchange contribution. Consequently, the old extracted width of $\Gamma(\rho^- \to \pi^-\gamma) = 35 \pm 10$ keV[70] is no longer regarded as definitive. Also, data from the first running period of E272 on the $\rho^- \to \pi^-\gamma$ decay, where, due to the high energy of the experiment, an A_2 exchange contribution could be ignored, indicate $\Gamma(\rho^- \to \pi^-\gamma) = 71 \pm 7$ keV; this agrees with the

result of $30 < \Gamma < 80$ keV of the old experiment obtained under weaker assumptions (such as the possible presence of isovector contributions to strong coherent production).

The neglect of such isovector contributions in the analysis of cross sections obtained at lower energies also affects the extraction of measurements of C_s. Because this was omitted in the first study of $K^{*+}(890) \to K^{+}\gamma$, it seems safe to conclude that a direct comparison of our measurement of C_s with an extrapolated value from that experiment is invalid.

Finally, our result for $\Gamma(K^{*+}(890) \to K^{+}\gamma)$, examined in light of theoretical predictions for $\Gamma(\overline{K^{o*}} \to \overline{K^{o}}\gamma)$, indicate that a re-measurement of the latter, in an experiment where the separation of the Coulomb and strong production processes would be less model dependent, might be of great value in resolving the conundrum this decay presents regarding the radiative decays of the $J^P = 1$ meson nonet.[71]

REFERENCES

1. M. Gell-Mann, Physics Letters 8, 214 (1964).
2. M. Kobayashi and T. Maskawa, Progress of Theoretical Physics 49, 652 (1973).
3. O. W. Greenberg, Physical Review Letters 13, 598 (1964).
4. H. Fritzsch, M. Gell-Mann, and H. Leutwyler, Physics Letters 47B, 365 (1973).
5. S. Okubo, Physics Letters 4, 14 (1963).
6. C. Becchi and G. Morpurgo, Physical Review 140, 687 (1965).
7. G. Morpurgo in Theory and Phenomenology in Particle Physics, (1968), edited by A. Zichichi (Academic Press, New York, 1969), p. 136.
8. P. J. O'Donnell, Physical Review Letters 36, 177 (1976).
9. R. Van Royen and V. F. Weisskopf, Nuovo Cimento A50, 617 (1967).
10. G. Grunberg and F. M. Renard, Nuovo Cimento 33A, 617 (1976).
11. M. Gourdin in Meson Resonances and Related Electromagnetic Phenomena, (1971), edited by R. H. Dalitz and A. Zichichi (Editrice Compositori, Bologna, Italy, 1972), p. 219.
12. P. J. O'Donnell, Review of Modern Physics 53, 673 (1981).
13. J. J. J. Kokkedee, The Quark Model (W. A. Benjamin, Inc., New York, 1969).
14. G. Morpurgo, Physics 2, 95 (1965).
15. R. P. Feynman, Quantum Electrodynamics, (W. A. Benjamin, Inc., Reading, Mass., 1976), p. 5.

16. J. D. Jackson in Proceedings of Summer Institute on Particle Physics, edited by Martha C. Zipf, SLAC-198 (1976), p. 147.
17. W. R. Holzon, Physical Review Letters 41, 1213 (1978).
18. M. M. Nagels, Nuclear Physics B147, 189 (1979).
19. O. W. Greenberg, Physics Letters 70B, 465 (1977).
20. L. I. Schiff, Quantum Mechanics (McGraw-Hill Inc., New York, Third Edition, 1968).
21. R. B. Teese and R. Settles, Physics Letters 87B, 111 (1979).
22. S. Oneda, T. Tanuma, T. Toiya, and M. D. Slaughter, University of Maryland Physics Publication No. 80-198 (1980).
23. J. Franklin, Physical Review 172, 1807 (1968).
24. E. R. Cohen and B. N. Taylor, Journal of Physical Chemistry Reference Data 2, 633 (1973).
25. G. L. Greene et al., Physical Review D20, 2139 (1979).
26. L. Schachinger et al., Physical Review Letters 41, 1348 (1978).
27. D. A. Geffen and W. Wilson, Physical Review Letters 44, 370 (1980).
28. T. N. Pham, Ecole Polytechnique, preprint CPT A386.0380 (1980).
29. P. J. O'Donnell, Canadian Journal of Physics 55, 1301 (1977).
30. D. Berg et al., Physical Review Letters 44, 706 (1980).
31. W. C. Carithers et al., Physical Review Letters 35, 349 (1975).
32. T. Ohshima, Physical Review D22, 707 (1980), and references cited within.
33. T. Jensen et al., (1982) (submitted to Physical Review D).
34. K. S. Kolbig and B. Margolis, Nuclear Physics B6, 85 (1968).

35. L. Stodolsky, Physical Review 144, 1145 (1966).

36. R. J. Glauber in Lectures in Theoretical Physics, edited by W. E. Brittin, (Interscience Publishers, Inc., New York, 1959) Vol. 1, p. 315; High-energy Physics and Nuclear Structure (North Holland, Amsterdam, 1967) p. 311.

37. A. Y. Abul Magd et al., Physics Letters 50B, 182 (1969).

38. G. Faldt, Nuclear Physics B43, 591 (1972).

39. H. Primakoff, Physical Review 81, 899 (1951).

40. G. Morpurgo, Nuovo Cimento 31, 569 (1964).

41. S. M. Berman and S. D. Drell, Physical Review 133, 791 (1964).

42. Ya. I. Azimov et al., Soviet Journal of Nuclear Physics 22, 394 (1975).

43. Y. Nagashima and J. Rosen, University of Rochester Report UR-875-295 (1969).

44. N. Jurisic and L. Stodolsky, Physical Review D3, 724 (1971).

45. A. Halprin, C. M. Andersen, and H. Primakoff, Physical Review 152, 1295 (1966).

46. J. D. Jackson, Nuovo Cimento 34, 1644 (1964).

47. C. Michael, Nuclear Physics B57, 292 (1973).

48. M. L. Perl, High Energy Hadron Physics (J. Wiley and Sons, Inc., New York, 1974).

49. A. Jonckheere et al., Nuclear Instruments and Methods 180, 25 (1981).

50. Y. S. Tsai, Reviews of Modern Physics 46, 815 (1974).

51. "Review of Particle Properties," Reviews of Modern Physics 52, No. 2 (1980).

52. G. Charpak et al., Nuclear Instruments and Methods 99, 279 (1972).

53. C. R. Kerns, Fermilab Report TM-819 2510.000, (October 1978).

54. Y. Chatelus et al., Nuclear Instruments and Methods 171, 127 (1980).

55. T. Jensen, Ph.D. Thesis, University of Rochester Report UR-747 (1980).

56. C. Nelson et al., (1982) (submitted to Nuclear Instruments and Methods).

57. T. F. Droege, F. Lobkowicz, and Y. Fukushima, Fermilab Report TM-746 2500.000, (October 1977).

58. S. Cihangir, Ph.D. Thesis, University of Rochester (1981).

59. A. Breskin et al., Nuclear Instruments and Methods 124, 189 (1975).

60. A. N. Walenta, Nuclear Instruments and Methods 111, 467 (1973).

61. J. D. Jackson, Classical Electrodynamics, (J. Wiley and Sons, Inc., New York, Second Edition, 1975), p. 647.

62. A. S. Carroll et al., Physics Letters 80B, 319 (1979).

63. A. S. Carroll et al., Physics Letters 61B, 303 (1976).

64. L. A. Fajardo et al., Physical Review D24, 24 (1981).

65. F. James and M. Roos, CERN Computer program MINUIT, D506, D516 (1976).

66. E. J. Sacharidis et al., Max-Planck-Institut Fur Physik und Astrophysik preprint (1980), and references cited within.

67. C. Bemporad et al., Nuclear Physics B15, 1 (1973).

68. D. Berg et al., Physics Letters 98B, 119 (1981).

69. A. N. Kamal and G. L. Kane, Physical Review Letters 43, 551 (1979).

70. B. Gobbi et al., Physical Review Letters 33, 1450 (1974).

71. A novel approach to such a measurement is given by L. S. Littenberg, Brookhaven National Laboratory preprint BNL-26954 (1979).